Analysis of transition metal complexes formed through contact of skin with circulating coins and metabolipidomic changes induced by dermal nickel penetration determined in an *ex vivo* porcine ear skin model

Cumulative Dissertation

by

Azar Rezaei

Submitted to the
Faculty of Biology and Chemistry (FB 08)
and prepared at the
Institute of Inorganic and Analytical Chemistry

for the Degree of
Doctor rerum naturalium (Dr. rer. nat.)

Justus Liebig University Giessen, Germany
Giessen, 2024

Advisor and first referee:

Prof. Dr. Bernhard Spengler
Justus Liebig University Giessen
Institute of Inorganic and Analytical Chemistry
Heinrich-Buff-Ring 17
D-35392 Gießen

Second referee:

Prof. Dr. Siegfried Schindler
Justus Liebig University Giessen
Institute of Inorganic and Analytical Chemistry
Heinrich-Buff-Ring 17
D-35392 Gießen

Day of oral exam:

TABLE OF CONTENTS

PUBLICATIONS

1) **Analysis of transition metal complexes formed through contact of skin with Euro coins**

   Rezaei, A.; Heiles, S.; Spengler, B.; Schindler, S. Mass Spectrometric Analysis of Transition Metal Complexes Formed through Contact of Artificial Sweat with Circulating Euro Coins. *Zeitschrift für Anorg. und Allg. Chemie* **2024**, *650* (4), e202300213

2) **Metabolipidomic changes induced by dermal nickel penetration determined in an ex vivo porcine ear skin model**

   Rezaei, A.; Ganashalingam, Y.; Schindler, S.; Spengler, B.; Keck, C. M.; Schulz, S. Metabolipidomic Changes Induced by Dermal Nickel Penetration Determined in an Ex Vivo Porcine Ear Skin Model. *Rapid Commun. Mass Spectrom*. **2024**, 38 (20), e9891

LIST OF ABBREVIATIONS

ACD	allergic contact dermatitis
AD	atopic dermatitis
AGC	automatic gain control
AP	atmospheric pressure
APCs	antigen-presenting cells
ASS	artificial sweat solution
CE	capillary electrophoresis
CER	ceramide
CHOL	cholesterol
CHCA	α-Cyano-4-hydroxycinnamic acid
CID	collision-induced dissociation
DAG	diacylglycerides
DCs	dendritic cells
DDA	data-dependent acquisition
DDTC	diethyldithiocarbamate
DESI	desorption electrospray ionization
DHB	2,5-dihydroxybenzoic acid
DIA	data-independent acquisition
DMG	dimethylglyoxime
DTH	delayed-type hypersensitivity
ECD	electron capture dissociation
EFAs	essential fatty acids
EPMA	electron probe microanalysis
ESI	electrospray ionization
FFAs	free fatty acids
FT-ICR	fourier-transform ion cyclotron resonance
GC-MS	gas chromatography/mass spectrometry
GNPS	global natural products social molecular networking
HCD	higher-energy collisional dissociation

HESI	heated electrospray ion source
HMDB	human metabolome database
HPLC	high-performance liquid chromatography
IARC	international Agency for Research on Cancer
ICP	inductively coupled plasma
KEGG	kyoto encyclopedia of genes and genomes
LA-ICP-MS	laser ablation inductively coupled plasma mass spectrometry
LCFAs	long-chain fatty acids ()
LC-MS/MS	liquid chromatography coupled with tandem mass spectrometry
LDI-MS	laser desorption/ionization mass spectrometry
LLE	liquid-liquid extraction
LPC	lysophosphatidylcholine
MAG	monoacylglycerides
MALDI	matrix-assisted laser desorption/ionization
MRI	magnetic resonance imaging
MS	mass spectrometry
MSI	mass spectrometry imaging
MTBE	methyl-tert-butyl ether
m/z	mass-to-charge-number ratio
NCE	normalized collision energy
NIST	the national institute of standards and technology
NMR	nuclear magnetic resonance
OCFA	odd chain fatty acids
ox-LDL	oxidized low-density lipoprotein cholesterol
PBS	phosphate-buffered saline
PC	glycerophosphatidylcholine
PE	glycerophosphatidylethanolamine
PET	positron emission tomography
PIXE	proton beam microprobe
QIT	quadrupole ion trap
REACH	registration, evaluation, authorization, and restriction of chemicals

RXLI	recessive X-linked ichthyosis
SB	stratum basale
SC	stratum corneum
SEM	scanning electron microscope
SG	stratum granulosum
SIMS	secondary ion mass spectrometry
SM	sphingomyelin
SS	stratum spinosum
SXRF	synchrotron X-ray fluorescence
TEM	transmission electron microscopy
TIC	total ion current
TLR4	toll-like receptor 4
TOF	time of flight
TSLP	thymic stromal lymphopoietin
ULCFA	ultra-long chain fatty acids
VLCFA	very long-chain fatty acids
XANES	X-ray absorption near-edge spectroscopy
µXAS	micro X-ray absorption spectroscopy

DECLARATION

I have completed this dissertation independently, without any unauthorized assistance, and received only acknowledged help. I have properly cited all direct quotes, content from other sources, and information from verbal communications. I agree to have my thesis checked using anti-plagiarism software. I have adhered to the principles of good scientific conduct outlined in the charter of the Justus Liebig University Giessen „Satzung der Justus-Liebig-Universität Gießen zur Sicherung guter wissenschaftlicher Praxis“ in carrying out the investigations described in the dissertation.

place, date, signature

ABSTRACT

ABSTRACT

Nickel allergic contact dermatitis (Ni-ACD) is the most common delayed-type hypersensitivity reaction affecting the skin worldwide, yet the underlying mechanisms remain elusive. This study presents a novel approach combining tandem mass spectrometry (MS/MS) and matrix-assisted laser desorption/ionization mass spectrometry imaging (MALDI MSI) to shed light on these interactions:

The MS/MS analysis of metal complexes on 1-euro coins, a prevalent nickel, copper, and zinc source, unveiled their distribution with micrometer precision. A notable result from atmospheric pressure laser desorption/ionization mass spectrometry imaging (AP-LDI MS) imaging of a cleaned 1-Euro coin is the detection of signals at *m/z* 207.8941 ($[C_4HO_3NNi+K]^+$) and *m/z* 116.9527 ($[CH_4NZn+Na]^+$). Furthermore, we delved into the impact of simulated sweat components such as lactic acid, urea, and sodium chloride on metal dissolution, leading to the discovery of a unique copper complex at *m/z* 140.9728 $[Cu(CH_4N_2O)+H_2O]^+$. Notably, the concentration of metal ions increased on the surface of coins treated with artificial sweat solutions compared to cleaned Euro coins, especially nickel metal ions. Following the developing method for investigating metal ions, the MALDI MSI analysis of *ex vivo* porcine ear skin exposed to increasing nickel concentrations revealed the spatial distribution of nickel-induced metabolic alterations. We further investigated nickel penetration using the dimethylglyoxime (DMG) staining method. This method showed that most nickel ions were confined to the stratum corneum for lower nickel concentrations (up to 84 $\mu g/cm^2$). Interestingly, areas with high nickel accumulation within the stratum corneum exhibited decreased levels of arginine and ceramides. Meanwhile, the deeper viable epidermis and dermis showed downregulation of specific lipids such as phosphatidylcholines and sphingomyelins.

These findings advance our understanding of metal allergens and highlight the potential impact of sweat composition on increasing metal ions, which leads to metal allergy development. Moreover, the research provides direct insights into the effect of common metal allergens on skin metabolites and lipids. This underscores the need for further research to delve into the mechanisms of metal penetration and their effects on skin composition, which could potentially revolutionize treatment options for metal sensitivity and enhance the quality of life for individuals with metal allergies.

ZUSAMMENFASSUNG

Nickelallergie (Ni-AKD) ist weltweit die häufigste allergische Kontaktdermatitis vom Spättyp, wobei die zugrundeliegenden Mechanismen jedoch weitgehend ungeklärt bleiben. Diese Studie präsentiert einen neuartigen Ansatz, der die Kombination von Tandem-Massenspektrometrie (MS/MS) und bildgebender Matrix-unterstützter Laser-Desorptions/Ionisations-Massenspektrometrie (MALDI-MSI) nutzt, um diese Wechselwirkungen zu beleuchten.

Die MS/MS-Analyse von Metallkomplexen auf 1-Euro-Münzen, einer relevanten Nickel-, Kupfer- und Zinkquelle, zeigte ihre Verteilungen mit mikrometergenauer Präzision. Ein bemerkenswertes Ergebnis der bildgebenden Atmosphärendruck-Laser-Desorptions-/Ionisations-Massenspektrometrie (AP-LDI-MS) einer gereinigten 1-Euro-Münze ist der Nachweis von Signalen bei *m/z* 207,8941 ($[C_4HO_3NNi+K]^+$) und *m/z* 116,9527 ($[CH_4NZn+Na]^+$). Darüber hinaus untersuchten wir den Einfluss künstlichem Schweiß mit den Komponenten Milchsäure, Harnstoff und Natriumchlorid auf die Metall-Auflösung, was zur Beobachtung eines spezifischen Kupferkomplexes bei m/z 140,9728 $[Cu(CH_4N_2O)+H_2O]^+$ führte.

Bemerkenswerterweise stieg die Konzentration von Metallionen auf der Oberfläche von mit künstlichem Schweiß behandelten Münzen im Vergleich zu gereinigten Euromünzen, insbesondere die von Nickel-Metallionen, signifikant an. Nach der Entwicklung der Methode zur Untersuchung von Metallionen zeigte die MALDI-MSI-Analyse von *ex vivo* porciner Ohrhaut, die erhöhten Nickelkonzentrationen ausgesetzt war, die räumliche Verteilung nickelinduzierter Stoffwechselveränderungen. Wir untersuchten außerdem die Nickelpenetration mit der Dimethylglyoxim (DMG)-Färbemethode. Diese Methode zeigte, dass die meisten Nickel-Ionen bei niedrigeren Nickelkonzentrationen (bis zu 84 $\mu g/cm^2$) auf das Stratum corneum beschränkt waren. Interessanterweise zeigten Bereiche mit hoher Nickelakkumulation im Stratum corneum einen verringerten Gehalt an Arginin und Ceramiden. Gleichzeitig zeigten die tieferen Schichten der lebenden Epidermis und Dermis eine Herunterregulation spezifischer Lipide wie Phosphatidylcholine und Sphingomyeline. Diese Ergebnisse erweitern unser Verständnis von Metallallergenen und beleuchten den potenziellen Einfluss der Schweißzusammensetzung auf die Erhöhung der Metallionenkonzentration, die potentiell zur Entwicklung einer Metallallergie führt.

ZUSAMMENFASSUNG

Darüber hinaus liefern die Ergebnisse direkte Einblicke in die Auswirkungen gängiger Metallallergene auf Hautmetabolite und -lipide. Dies unterstreicht die Notwendigkeit weiterer Forschung, um die Mechanismen der Metallpenetration und ihre Auswirkungen auf die Hautzusammensetzung zu untersuchen, was potenziell zu neuen Behandlungsmöglichkeiten für Metallsensibilität und zu einer Verbesserung der Lebensqualität für Menschen mit Metallallergien führen könnte.

.

CHAPTER I

CHAPTER I

1. INTRODUCTION

1.1 A Brief Introduction to Metals

Metals have been crucial to human progress since ancient times. They are essential for metal production, creating valuable products, and recycling.[1] Metals possess distinctive properties that make them necessary in numerous industries, such as alloy production. Additionally, they are vital components in technologies like touchscreens, circuit boards, and fiber optic cables. The demand for metals continues to rise with the growing global population and living standards. Metals are crucial for electricity transmission and are heavily used in manufacturing, consuming three gigatons of metal annually globally.[2]

Apart from technological applications, metals are vital in construction, transportation, electronics, and infrastructure development. The use of specific metals is often intertwined with the history of civilizations. For example, transitioning from the Bronze Age to the Iron Age brought transformative changes to many societies.[2]

Metals are also a fundamental part of our everyday lives. For instance, many higher-denomination euro coins are circulated in Germany. In 2011, an estimated €2.3 billion worth of euro coins were used for transactions in Germany, representing about 36% of the total issued by the Deutsche Bundesbank.[3] 1 and 2 EUR coins are both composed of two alloys: Cu 75%, Zn 20%, Ni 5%, and Cu 75%, Ni 25%.[4]

Furthermore, certain metals, such as copper (Cu), zinc (Zn), and manganese (Mn), are crucial for normal biological function and essential to enzyme activities within cells.[5] The precise control of metal ions, including sodium (Na), potassium (K), magnesium (Mg), calcium (Ca), vanadium (V), chromium (Cr), manganese (Mn), iron (Fe), cobalt (Co), nickel (Ni), copper (Cu), zinc (Zn), and molybdenum (Mo), are critical for maintaining vital biological functions.[6] In conclusion, metals have profoundly impacted human history, technology, and biology, demonstrating their enduring importance in the modern world. However, balancing metal ions within the body is crucial, as an excess or deficiency can be harmful.

Certain metals are essential for normal biological functions but can also adversely affect human health. Species, age, gender, genetics, and nutritional status can influence individual susceptibility to metal toxicity. Some heavy metals, while essential in small quantities, can have both beneficial and harmful effects, with the potential to disrupt bodily functions and even cause cancer. These metals are widespread in the environment, contaminating soil, water, and air and entering the food chain, potentially leading to cellular damage and cancer development.[7] Certain heavy metals, such as arsenic, cadmium, and chromium, have been identified as primary culprits in causing cancer by the International Agency for Research on Cancer (IARC).[8] While nickel is an essential trace element, hazards associated with its exposure are predominantly artificial, with occupational settings posing significant risks.[9] These risks extend beyond immediate concerns, with nickel's toxic effects impacting various biological systems, including the immune system, nervous system, reproductive system, and development.[9] Research suggests that nickel's cancer-causing activity is linked to its disruption of DNA and is also a common cause of contact allergies.[10] Nickel is the most common contact allergen in industrialized countries worldwide.[11] Sensitization to nickel is often identified on patch testing and is associated with ear piercing.[12] These findings emphasize the potential health risks associated with metal exposure. They prompt us to further investigate metal toxicity as a potential cause, especially nickel allergy, and require an understanding of the molecular mechanism of metal allergy.

1.2 Metal allergy

Metal hypersensitivity affects a significant portion of the population, with estimates suggesting prevalence rates of around 10-15% of individuals. A higher incidence is observed in women (around 10-20% versus 1-3% in men).[13,14] Numerous studies and clinical observations have shown that nickel is the most commonly encountered allergen among various contact allergens.[15]

Certain professions can increase the risk of developing nickel allergies due to frequent exposure to nickel-containing items. People who work in jobs that require regular contact with nickel-containing items are particularly at risk. Occupations such as cashiers, locksmiths, carpenters, metalworkers, hairdressers, jewelers, dental technicians, auto-mechanics, electroplaters, dyers, and homemakers often handle items like coins, keys, jewelry, tools, and other metal objects that may contain nickel.[16]

Limiting nickel exposure from items used in prolonged contact is essential to prevent nickel allergy and dermatitis.

Nickel exposure commonly leads to contact dermatitis, especially for people with sensitive skin. Due to high sensitization rates to nickel salts, European regulations were implemented. Denmark and Sweden were the first to introduce such regulations in 1990 and 1994.[17] These efforts resulted in the EU Nickel Directive (Directive 94/27/EC) and, later, the Registration, Evaluation, Authorization, and Restriction of Chemicals (REACH) legislation.[18]

The Nickel Directive specifically addresses nickel released from products that come into direct contact with the skin, such as jewelry. This directive sets migration limits for nickel release, with stricter limits (0.2 $\mu g/cm^2/week$) for post assemblies for pierced ears and other body parts (Directive 94/27/EC). The nickel release limit is 0.5 $\mu g/cm^2/week$ for other products with prolonged skin contact.[19,20]

To measure nickel release, the EN 1811 test method is used. This standardized test involves submerging the object in a synthetic sweat solution for a week and then quantifying the amount of nickel leached.[21]

Despite implementing regulations to limit nickel release, nickel allergy persists as a significant health concern within the EU.[17] Understanding the mechanisms underlying metal toxicity and its role in biological processes is crucial for developing effective prevention and treatment strategies

1.3 Molecular Mechanisms of Nickel Allergy

Allergic contact dermatitis (ACD) is a complex immune reaction triggered by exposure to tiny molecules in our surroundings. It results in an inflammatory skin condition caused by interactions with small organic chemicals and metal ions.[22] Metal allergies are T cell-mediated delayed-type hypersensitivity (type IV) that result from contact allergies to metal ions in our environment. Sensitization begins with exposure to Nickel on the skin, which causes the production of proinflammatory cytokines (TNF-α and IL-1β), Thymic Stromal Lymphopoietin (TSLP), and chemokines.[23]

Due to their small size, metal ions are considered incomplete antigens (or haptens). To become complete antigens, they need to bind to endogenous peptides. These haptens activate and move special epidermal and dermal dendritic cells (DCs) through the lymphatic system to the lymph nodes.

They then form a trimolecular complex associating with MHC II molecules, peptides, and T-cell receptors. This complex is responsible for inducing a specific T-cell response. The new complex between metal-MHC/peptide may produce neoantigens recognized by T cells due to the formation of novel epitopes.[24] In humans, nickel triggers the Toll-like receptor 4 (TLR4) pathway in dendritic cells (DCs). Once the dendritic cells reach the lymph nodes, they present haptenated peptides to T cells. The T cells then undergo an increase in numbers, become activated, and differentiate into hapten-specific T cells. During this sensitization phase, the inflammatory cytokines like TNFα, IL-1b, IL-6, IL-8, IL-12, or IFNα and -β produced in the draining lymph nodes contribute to efficient hapten-specific T-cell activation, proliferation, and differentiation.[18] Once the T cells are primed, they leave the lymph nodes and migrate back to the skin. During the elicitation phase, when a person is exposed to the same allergen again, they take it up and present it to specific T cells.[23] These T cells activate and release inflammatory chemicals such as cytokines and chemokines at the exposure site. This leads to an allergic reaction and skin rashes, characteristic of the specific allergen[25,26] shown in Figure 1. Previous research has illuminated the cellular and molecular mechanisms of ACD, providing valuable insights into the role of different effector cells and the triggering role of haptens in initiating this immune response.[27] In the context of ACD, lipids also participate in various signaling pathways and immune reactions. Lipids are critical in ACD, serving essential functions in skin structure and immune responses. Fatty acids contribute to the skin's integrity and function among these lipids. They are integral to forming triglycerides, which store energy and provide cell insulation.[28]

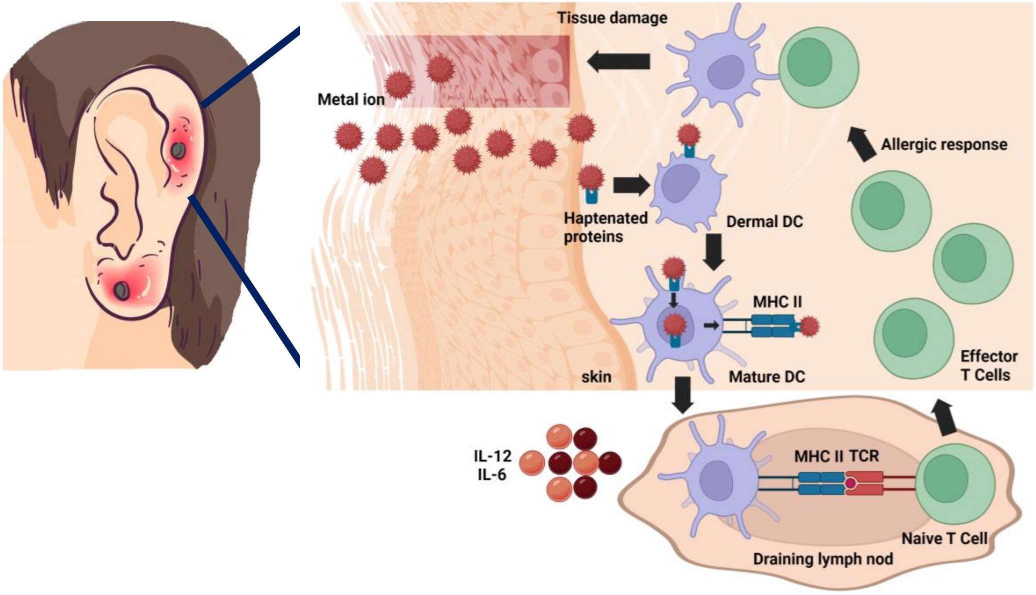

Figure 1. Mechanism of metal allergy. Created with BioRender.com

The skin is a primary defense mechanism against external threats, including pathogens, chemicals, irritants, and allergens, preventing ACD.[29] However, if these substances penetrate the deeper layers of the skin, they may trigger an immune response, highlighting the crucial role of the skin's barrier function.[30] Disruptions in the stratum corneum, the outermost layer of the epidermis, can lead to atopic dermatitis (AD) by compromising the skin barrier function. The outermost layer of the epidermis, the stratum corneum, forms the core of this defensive shield. The epidermis, which ranges from 50 to 100 µm thickness, consists of four sublayers: the outermost stratum corneum (SC), followed by the stratum granulosum (SG), the stratum spinosum (SS), and the innermost stratum basale (SB) shown in Figure 2.[31]

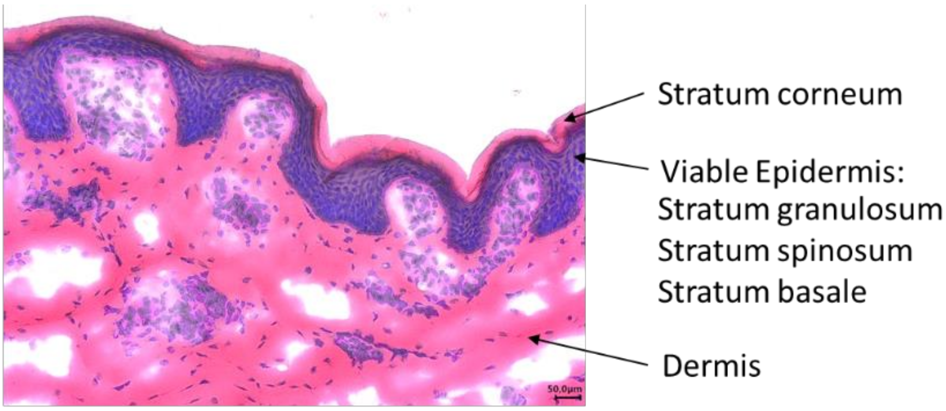

Figure 2. H&E staining of fresh frozen pig ear cross-section (10 µm thickness) magnification 1000x.

Skin barrier dysfunction significantly contributes to ACD by enhancing skin permeability, facilitating the rapid penetration of allergens, and triggering immune responses. AD, closely associated with ACD, exhibits skin barrier defects, including changes in lipid composition and reduced ceramide levels, resulting in compromised barrier function.[32] The lipid bilayer in the stratum corneum, comprising hydrophobic lipids such as ceramides, cholesterol, and free fatty acids, plays a crucial role in maintaining skin hydration and integrity. [32]Alterations in lipid composition, such as shorter chain lengths of fatty acids and ceramides observed in AD skin, further exacerbate skin permeability and contribute to barrier dysfunction.[32] Restoring the skin barrier function becomes pivotal in preventing or halting the progression of AD, given that the root cause is believed to lie within the skin barrier itself.[33] Understanding the interplay between ACD, allergens, and the skin's lipid barrier is crucial for developing effective prevention and treatment strategies. By understanding this complex interaction, we can work towards strengthening the skin's barrier function and reducing the allergic response. This knowledge can help develop specific treatments to prevent and manage ACD and other skin allergies. To achieve this, recent technological advancements in imaging techniques of metals in cells and tissues have enabled researchers to track the movement of metals through skin tissue as well as metabolipidomic changes induced by dermal metal penetration as described below in section 1.4.

1.4 Imaging Techniques of Metals in Cells and Tissues

Determining the exact location and amount of trace metals in biological tissues is crucial for understanding their effect on the body. Several analytical techniques can provide detailed analysis at a micro level, each with its strengths and weaknesses. This text will compare and contrast electron probe microanalysis (EPMA), proton beam microprobe (PIXE), electron-probe energy-dispersive spectroscopy (EDS), X-ray microprobe including synchrotron X-ray fluorescence (SXRF), micro X-ray absorption spectroscopy (µXAS) and X-ray absorption near-edge spectroscopy (XANES), magnetic resonance imaging (MRI), positron emission tomography (PET), autoradiography, and mass spectrometry imaging (MSI)—including secondary ion mass spectrometry (SIMS), matrix-assisted laser desorption ionization mass spectrometry imaging (MALDI-MSI), and laser ablation inductively coupled plasma mass spectrometry imaging (LA-ICP MSI) to understand their suitability for analyzing trace metals in biological samples.

EPMA is a valuable technique for studying the distribution and quantification of elements, including trace metals, within biological tissues. It employs a focused electron beam to induce emission of characteristic X-rays from the elements present in the sample. These element-specific X-rays are then dispersed by a crystal monochromator and detected, enabling researchers to identify the elements present and quantify their concentrations. However, EPMA has limitations in spatial resolution, typically around 100 nanometers.[34] One significant challenge is the potential for matrix effects resulting from the influence of the surrounding sample composition on the X-ray emission and absorption characteristics of the element of interest. Additionally, conductive samples or those coated with conductive material are required to prevent the buildup of electrostatic charges that can disrupt the analysis.[35]

PIXE uses a focused beam of protons and offers good sensitivity for trace metals. It can analyze non-conductive samples, which is advantageous for analysis of biological tissues. However, its spatial resolution is generally lower than EPMA, ranging from 1 to 10 µm.[36]

EDS provides elemental analysis capabilities commonly used with scanning electron microscopy (SEM) and transmission electron microscopy (TEM). However, electron beam scattering can diminish the advantage of SEM's nanometer-scale resolution in biological specimens, particularly those with typical thicknesses. Reducing the spatial resolution for EDS analysis to the low millimeter range makes it unsuitable for detailed subcellular or biomolecular investigations.[36]

X-ray microprobe (SXRF, µXAS, XANES) offers exceptional capabilities for analyzing trace metals in biological tissues. It focuses a beam of X-rays onto the sample, inducing either the emission of fluorescent X-rays or the absorption of X-rays, depending on the incident X-ray energy. This allows for excellent spatial resolution, down to a remarkable 0.3 micrometers, and the analysis of a broad range of elements.[37] Techniques like XANES and micro X-ray absorption spectroscopy (µXAS) provide valuable insights beyond elemental identification, revealing the target metal's oxidation state and local environment within the biological sample.[38] Like PIXE and EPMA, SXRF detects emitted X-rays to generate spatially resolved elemental distribution maps. Non-destructive techniques like EDS and µPIXE preserve sample integrity but may introduce artifacts due to the microprobe's interaction with the sample.

MRI is primarily known for anatomical and physiological imaging in vivo and holds the potential for trace metal analysis. It can detect specific isotopes like protons (^{1}H) and phosphorus (^{31}P), indirectly indicating trace metal concentrations due to their association with biological molecules.[39] However, MRI offers lower spatial resolution compared to other techniques discussed here. While developing effective MRI probes is promising, further research is needed to improve sensitivity and specificity for broader applicability in trace metal detection within biological samples.[39]

PET offers in vivo imaging capabilities, using radiolabeled metal chelators to study the distribution of specific metals. However, its spatial resolution is limited to millimeters.[39]

Autoradiography utilizes the interaction between radiation emitted by radiolabeled samples and photographic film. It provides high spatial resolution, down to 1 µm, for visualizing the distribution of trace metals in biological tissues. However, sensitivity limitations may impede the detection of low-abundance metals.[40]

On the other hand, mass spectrometry imaging (MSI)—including SIMS, MALDI-MSI, and LA-ICP MSI—has revolutionized the study of metal distribution within biological tissues.

The following section describes the strengths and applications of these three essential MSI techniques.

1.5 Mass Spectrometry Imaging

MSI is a label-free analytical technique crucial in analytical chemistry and biochemistry. It enables the visualization of various molecules on a sample surface, including biomarkers, metabolites, lipids, peptides, or proteins, without labeling in a single experiment.[41]

The MSI operation principle involves a straightforward three-step process for measuring ions' mass-to-charge-number ratio (m/z) through mass spectrometry:

1. The molecules are converted into gas-phase ions employing an ionization source.
2. The ions are separated based on their m/z values using magnetic or electric fields within the mass analyzer.
3. The ions are separated and detected as electrical signals at their specific m/z values, revealing their abundances.

One way to determine the identity of a signal at a specific m/z value is by conducting fragmentation on ions from each pixel using tandem MS (MS/MS). This process produces fragments that can help identify the unknown molecule's structure. Alternatively, the molecule can be identified by accurately matching its intact mass to databases of known molecules within a specific mass error range.[41]

MSI relies on various ionization techniques with specific requirements to ensure sample integrity. These techniques play a crucial role in visualizing the unlabeled molecular components present within biological or environmental samples at a microscopic level. The methods include SIMS,[42] which was introduced for elemental imaging in 1962, and LA-ICP MSI, introduced in 1985, [43]MALDI-MSI was introduced in 1994,[44] while Desorption Electrospray Ionization Mass Spectrometry Imaging (DESI-MSI) was introduced in 2004.[45] Mass spectrometry imaging includes several techniques, each with its strengths and limitations.

SIMS is a powerful technique that aids in studying the distribution of lipids, metabolites, drugs, metals, and other molecules in biological tissues and cells. SIMS utilizes a focused beam of primary ions (e.g., Cs+, O-) to sputter secondary ions from the sample surface. A mass spectrometer then analyzes the secondary ions to determine the elemental and isotopic composition of the sample. SIMS exhibits exceptional spatial resolution, surpassing 100 nanometres, enabling precise visualization of metal distribution within cellular structures.[46]

However, SIMS measurements have some limitations. This technique requires a vacuum environment, and the ion beam used for analysis breaks down biomolecules, making it challenging to detect them. Proper sample preparation is crucial for (Nano)SIMS. The analysis is performed under ultra-high vacuum (UHV) conditions, requiring the preservation of cellular and tissue structural and chemical integrity.[47]

ICP-MS is a susceptible analytical technique used to detect and quantify trace levels of metals and some non-metals in various sample types. LA-ICP-MS combines laser ablation for sample introduction with ICP-MS for elemental analysis. A pulsed laser beam ablates a microscopic volume of the sample, and the ablated material is swept into the ICP-MS for elemental detection. LA-ICP-MS offers excellent detection limits for trace metals and good spatial resolution (around 10 µm).[47] It can detect metals in low concentrations (parts per trillion to parts per quadrillion range).[47] This means that researchers can examine metals with high spatial resolution, down to the cellular level, while retaining the high sensitivity, wide dynamic range, and multi-element analysis capabilities of ICP-MS.[47]

Despite its advantages, this technique suffers from matrix effects, requiring careful calibration for accurate quantification.[48]

MALDI is a soft ionization method used in mass spectrometry to analyze biomolecules. To perform MALDI MSI analysis, it is crucial to follow a defined workflow strictly. This includes sectioning the tissue using a suitable method and placing the tissue section on a conductive slide. Depending on the specific analysis, the tissue may need to be washed. The tissue sample should be coated with a dissolved matrix using the specified method.[49] Possible matrices include 2,5-dihydroxybenzoic acid (DHB), α-cyano-4-hydroxycinnamic acid (α-CHCA), and sinapinic acid. Co-crystallization of the analyte with the matrix prevents direct laser interaction, reducing fragmentation. When the matrix absorbs energy from a laser (typically a UV laser at a wavelength between 330 and 360 nm), it facilitates the desorption and ionization of the analyte. Protons released from the matrix lead to the formation of pseudomolecular ions. The resulting ion plume is then analyzed by mass spectrometry (see Figure 3).[50] The MALDI technique offers exceptional sensitivity and lateral resolution down to one µm, making it valuable for examining the local biological systems.[41,51,52]

It has broader applicability compared to ICP-MS and can work with a wider variety of samples. It generally has higher sensitivity and good lateral resolution, enabling detailed imaging.

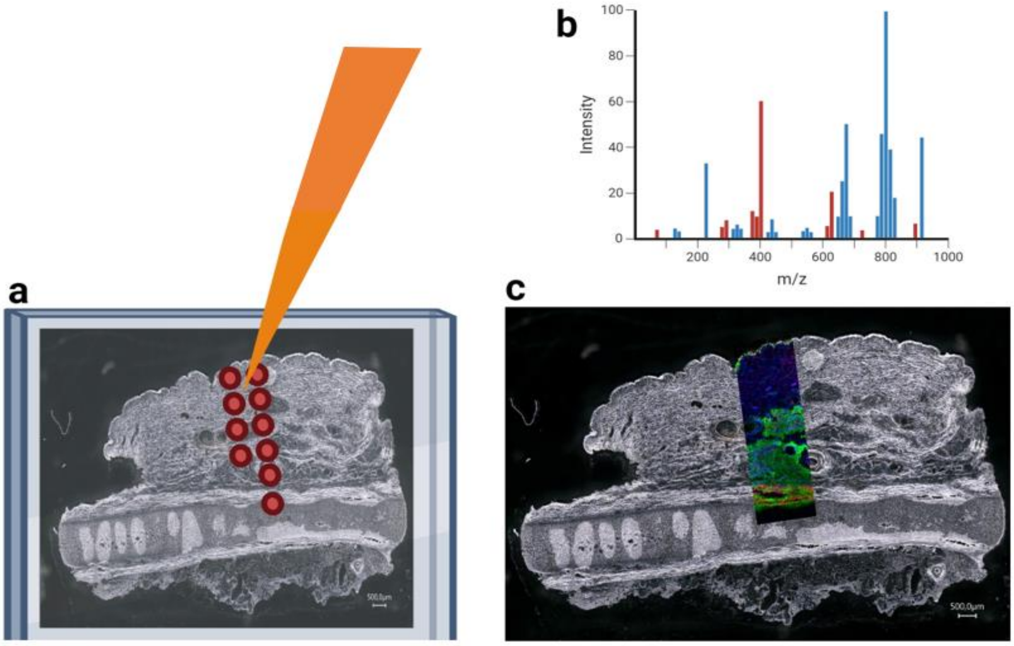

Figure 3. In MALDI-MSI, a tissue sample is positioned on a target and then scanned by a LASER (a). The generated ions are directed into the mass spectrometer, producing a mass spectrum (b). Each specific LASER spot can be correlated with a distinct mass spectrum, leading to the creation of a distribution image (c)

Recent advancements in MALDI, particularly AP-MALDI MSI sources, have enabled the analysis of complex biological samples while maintaining high resolution (around 1.4 micrometers) and working under conditions closer to the sample's natural state.[52]

However, a downside of MALDI is the need to apply a unique matrix, which can be time-consuming and affect the quality of results, especially at high resolution.

In addition to MALDI, LDI-MS is another sample analysis method. This technique involves using a laser pulse to ionize material directly from a surface, which is then detected through a mass analyzer. LDI-MS is particularly useful for analyzing samples on surfaces because it is quick and efficient. However, LDI ionization yields are typically lower than those of MALDI techniques, and significant fragmentation of analytes is regularly encountered.[41,51–53]

DESI is a technique that extracts chemical information directly from surfaces without requiring prior treatment. It has a spatial resolution of 50–100 µm. DESI is an ionization technique that allows surface analysis without adding a matrix or other treatment while the sample is kept under ambient conditions. Although DESI enables imaging capabilities, its spatial resolution is generally lower than that of other mass spectrometry imaging techniques like MALDI or SIMS. DESI-MS has been used to analyze various analytes in biological and environmental samples, such as alkaloids in plants, phospholipids in mammalian tissue, and lipids in bacteria and proteins.[54]

Researchers can choose the most suitable method by understanding the strengths and limitations of each. Due to its exceptional spatial resolution, SIMS offers precise mapping of ion distributions within biological samples. However, it is less effective for larger molecules and fragments complex molecules. On the other hand, DESI provides real-time analysis with ambient ionization but has lower sensitivity and needs improved spatial resolution compared to SIMS and MALDI. LA-ICP-MS for elemental analysis faces challenges such as sample-dependent ablation behavior and elemental fractionation, which may be magnified in environmental and life science applications. Considering the limitations of other techniques, MALDI-MSI is a compelling choice as it allows low-fragmentation analysis and correlation of chemical information with histological staining. Additionally, AP-MALDI MSI sources offer high resolution and the ability to work under conditions closer to the sample's natural experiences. However, sophisticated mass analyzers are needed when aiming at high mass resolution, fast analysis times, and exceptional mass accuracy.

The mass analyzer is the central component of any mass spectrometer, playing a critical role in separating ionized molecules based on their mass-to-charge-number ratio (m/z). This separation is the foundation for identifying and characterizing the molecules within a sample. Several analyzer designs exist, with quadrupoles, ion traps, time-of-flight (TOF) analyzers, and more advanced technologies like Fourier Transform Ion Cyclotron Resonance (FT-ICR) and Orbitrap mass analyzers being the most prevalent. Two key factors define an analyzer's performance: mass resolution and mass accuracy.[55] The mass resolution reflects the ability to distinguish between molecules with similar masses. Mass accuracy indicates how close the measured mass is to the actual mass. The specific mass analyzer and detector determine both, resolution and accuracy. Quadrupole, magnetic sector, and time-of-flight (TOF) mass spectrometers are well-suited to mapping elemental composition within a sample.[19] The choice of analyzer for high-resolution analysis depends on the specific needs. SIMS coupled with TOF excels at sensitively detecting atomic and small molecular ions with impressive spatial resolution down to 100 nm.[47]

In contrast, MALDI-MSI can leverage TOF or FT-ICR analyzers. Notably, MALDI-MSI analysis can even be performed under atmospheric pressure conditions. The choice between TOF and FT-ICR depends on the desired outcome. TOF instruments excel at detecting large molecules, even those reaching 100 kDa. FT-ICR, on the other hand, offers exceptional mass resolution for analyzing molecules up to a few kDa.[47] The Orbitrap mass analyzer emerged as a powerful alternative to previous technologies, particularly FT-ICR. Unlike the bulky and complex FT-ICR systems, the Orbitrap is based on a more straightforward design without the need for superconducting magnets. It also surpasses older TOF instruments regarding sensitivity and mass accuracy. The Q Exactive Orbitrap model exemplifies these advancements, offering exceptional selectivity, high resolution (up to 480,000 at m/z 200), and mass accuracy (<1 ppm) in a compact and affordable package, making it a more accessible option compared to FT-ICR.[56] Modern mass spectrometry instruments often push the boundaries by incorporating multiple analyzers within a single system, enabling even more complex analyses. These hybrid systems are referred to as "multiplexed mass spectrometers." Some notable examples include:

Quadrupole Ion Trap (QIT-TOF): This instrument allows you to perform tandem MS (MS/MS) experiments directly within it, facilitating the identification of unknown molecules.[57] Quadrupole Time-of-Flight (QTOF): This technique combines the separating power of a quadrupole analyzer with the high mass accuracy of TOF, providing excellent performance for complex samples.[58]

Fourier Transform Ion Cyclotron Resonance (FT-ICR): High-resolution imaging mass spectrometry is highly effective for analyzing low to medium molecular weight compounds.[59]

Ion Trap Orbitrap: Combines an ion trap's trapping capabilities with an Orbitrap analyzer's high mass accuracy, enabling sensitive detection and detailed characterization of complex mixtures.[60]

Quadrupole Orbitrap Analyzers Offer high mass accuracy and resolution and the ability to perform targeted and untargeted analyses.[61]

Now, after comparing different ionization methods and mass analyzers, here are some examples of mentioned applications:

Researchers leverage SIMS to investigate how metals interact with drugs, accumulate in tissues, and track metal-containing nanoparticles.[40,47] SIMS boasts exceptional spatial resolution, reaching 50 nanometers, enabling visualization of metal distribution within cellular structures with unmatched detail.[46] Applications include studying metal interactions with drugs and nanoparticle tracking. For instance, a recent study employed SIMS to analyze the localized corrosion of an aluminum alloy (AA2050-T8).[62]Advancements in Time-of-Flight (ToF-SIMS) imaging allow for the detection of trace metals like iron, magnesium, and gold alongside lipids and metabolites at high lateral resolution in cells and tissues.[19] This technology has revealed nickel accumulation in the human skin's outermost layer (stratum corneum) and upper epidermis.[63] Additionally, ToF-SIMS has detected metal allergens (nickel, cobalt, chromium) in deeper epidermal layers, suggesting promise for allergy research.[64] Furthermore, ToF-SIMS can map the distribution of iron, histidine, and heme fragments within pancreatic tissue sections, revealing alterations in metabolism.[65] Notably, NanoSIMS is a variant that can determine the distribution of metallodrugs and organic ligands with high spatial resolution.[66] SIMS measurements have limitations. The technique requires a vacuum environment, and the ion beam can fragment biomolecules, hindering detection. Proper sample preparation is crucial for (Nano)SIMS. Analysis occurs under ultra-high vacuum (UHV), preserving cellular and tissue integrity.[47]

MALDI-MSI can be combined with on-tissue chemical derivatization to effectively study the distribution of metal-based drugs and their metabolites within tissues. A recent study used diethyldithiocarbamate (DDTC) to image a platinum-based cancer drug and its metabolites in an in vitro tumor model, achieving simultaneous and specific imaging.[48]

Another study investigated the potential of atmospheric pressure LDI- Q Exactive MS for 3D surface profiling with elemental analysis, using a coin of distinct metal alloys as a sample.[53]

ICP-MS is a powerful tool for investigating metallodrug movement in biological systems.[67] However, it can be susceptible to matrix effects and may require calibration with appropriate standards. LA-ICP-MS, a variant technique, has been used to map transition metals (Fe, Cu, Zn, Mn, Ti) alongside alkali and alkaline-earth metals (Na, K, Mg, Ca) and even nonmetals (C, P, S) within native cryosections of mouse heart tissue.[68] Another study focused on rat kidneys using LA-ICP-TOFMS to quantify essential metals (Mg, Mn, Fe, Cu, Zn, Mo), providing insights into copper level regulation.[69]LA-ICP-MS also holds promise for bioimaging, with a study exploring the "polymer film strategy" and internal standardization showing promising results for eight out of eleven elements analyzed (Co, Ni, Cu, Zn, Se, Mo, Cd, Pt).[70]

With a comparison of the advantages and disadvantages of the mentioned ion sources and analyzers, we have selected the AP-SMALDI[5] AF ion source (TransMIT GmbH, Giessen, Germany) coupled to a Q Exactive HF Orbitrap mass spectrometer (Thermo Fisher Scientific (Bremen) GmbH, Bremen, Germany) with a mass resolution of 240,000 at *m/z* 200 for both, the mass spectrometric analysis of transition metal complexes formed through contact of artificial sweat with circulating Euro coins and the determination of metabolipidomic changes induced by dermal nickel penetration in an *ex vivo* porcine ear skin model. In the following, mass spectrometry imaging techniques for metal detection and metabolomics are described.

1.6 Metabolomics

Metabolomics, the study of small molecules within biological systems, has rapidly grown in recent years due to its wide-ranging applications across the life sciences. Although it should theoretically cover all metabolites below 2,000 Da, practical limitations in extraction, ionization, and detection restrict what can be observed in the metabolome.[71] This complex network comprises various compounds with different properties and concentrations, including amino acids, lipids, and organic acids.[72] Traditionally seen as energy stores, Lipids are increasingly recognized for their vital regulatory roles within cells, generating significant interest in the biomedical field.[71] Metabolomic techniques allow the analysis of hundreds of metabolites within a single sample, with targeted and untargeted approaches offering distinct advantages.[73] Targeted analysis focuses specifically on predefined metabolite groups, enabling precise quantification. Meanwhile, untargeted analysis offers a comprehensive view of all detectable metabolites within the sample.[74] Realizing the wealth of information within the metabolome requires specialized techniques for sample preparation, separation, mass spectrometry, and data processing and interpretation. These developments are crucial for unlocking the full potential of metabolomics in various scientific endeavors.

Sample preparation in metabolomics is a critical step that directly impacts the quality and interpretability of the data. The primary goal is to preserve the sample's original metabolic state, or "fingerprint," by minimizing metabolite degradation and ensuring a representative portion is analyzed.[75] This is achieved through a multi-step process.

First, immediate quenching upon sample collection is essential. Standard techniques include rapid freezing in liquid nitrogen, acidification, or quenching in cold methanol solutions.[76] These methods rapidly inactivate enzymes and halt metabolic activity, preventing further metabolite modification.[76]

Following quenching, in LC-MS-based metabolomics, tissues are often homogenized at low temperatures to facilitate efficient extraction.[76] Mechanical disruption using mortar and pestle, bead beating, or homogenizers breaks down tissues in a solvent.[77] Extraction itself is a crucial step in metabolomics. Liquid-Liquid Extraction (LLE) has traditionally been the workhorse for biofluids and tissues.[78] LLE utilizes immiscible solvents to partition metabolites based on their polarity. The selection of solvents plays a key role, with mixtures like chloroform/methanol or chloroform/methanol/water (Bligh and Dyer method) being popular choices due to their ability to extract both water-soluble and fat-soluble metabolites. Recent advancements explore alternative methods like uniphase extractions, offering advantages like simplicity and potentially higher yields.[76] One such example is the two-step extraction method developed by Leuthold et al.[79], which facilitates untargeted metabolomics and lipid profiling of human and porcine kidney tissue. This approach employs sequential extractions with methanol/water (1/1, v/v) followed by MTBE/methanol (3/1, v/v) after bead-based homogenization of a single tissue sample.[80]

Ultimately, the success of sample preparation relies on optimizing these steps for the specific sample type and desired metabolites. Careful consideration of quenching methods, homogenization techniques, and solvent selection ensures that the captured metabolome accurately reflects the in vivo state, paving the way for robust and informative metabolomic analyses.

Nuclear magnetic resonance (NMR) and mass spectrometry (MS) are the two main techniques used in metabolomics to analyze small molecules in complex samples.

NMR spectroscopy is advantageous due to its high-throughput fingerprinting, minimal sample preparation requirements, and non-destructive nature. However, its sensitivity limitations require larger sample sizes, making detecting low-abundance metabolites in complex mixtures challenging.[81]

On the other hand, MS provides superior sensitivity and high-throughput capabilities, allowing for the detection of a broader range of molecules in biological samples. This technique includes gas chromatography-mass spectrometry (GC-MS), liquid chromatography-mass spectrometry (LC-MS), and MSI, which can simplify complex mass spectra through metabolite separation and provide additional information on their properties.[72]

Despite its advantages, MS-based methods may result in the loss of metabolites during sample preparation, and the choice of ionization technique and sample introduction system may favor specific metabolite classes.

MS-based metabolomics has vast applications, including discovering disease biomarkers, drug development, nutritional science, toxicology, and forensic science.[81] Various types of mass spectrometers exist within MS, each with its strengths. Quadrupole (Q) mass analyzers are sensitive and selective but have low mass resolution. Combining a Q mass analyzer with a ToF analyzer in a QToF instrument enhances selectivity and mass resolution, improving the maximum mass resolution to approximately 40,000–60,000.[82] Orbitrap mass spectrometers achieve resolutions exceeding 250,000 and 1,000,000 for ions with m/z less than 300–350.[83] FT-ICR reaching >2,000,000 resolution offers a high resolving power.[82] However, its widespread use is limited due to its complexity.[84]

High-resolution MS reduces potential matches for unknown compounds based on elemental composition but does not provide definitive identification. MALDI-MS and MALDI mass spectrometry imaging (MALDI-MSI) are also useful for metabolite profiling in tissues, cells, and specific compartments.[85]

Advancements in tandem MS (MS/MS) and multistage MS (MSn) have significantly improved the ability to distinguish isomers and isobaric compounds and acquire structural information. Mass detection sensitivity and ion collection improvements have expanded fragmentation and mass detection capabilities beyond traditional MS/MS.[82]

Lipidomics and metabolomics are closely related fields in the broader area of systems biology. Both disciplines often use similar chromatographic separation methods, such as liquid chromatography (LC) or gas chromatography (GC) coupled with mass spectrometry (MS). Lipidomics, a subset of metabolomics, focuses on lipids specifically. Both fields generate large, complex datasets that require sophisticated bioinformatics tools for analysis. They frequently employ similar statistical and machine-learning approaches for data interpretation. Although similar, the sample preparation techniques for lipidomics may involve more specialized extraction methods tailored for lipids in LC-MS-based analysis. While lipidomics focuses on lipid species, it shares many methodological and conceptual similarities with the broader field of metabolomics. These similarities often allow the two fields to complement each other in comprehensive studies of biological systems.

Mass spectrometry (MS) is excellent at unraveling the complexities of the metabolome, but identifying metabolites is challenging. Predicted molecular formulas based on the accurate m/z and isotopic pattern of MS features can be searched in chemical databases like PubChem, ChemSpider, or Kyoto Encyclopedia of Genes and Genomes (KEGG). However, their coverage is limited due to many still-unidentified biomolecules.[82]

For lipids, specialized databases like LipidMaps, SphinGOMAP, METASPACE, and Lipid Bank provide a wealth of structural and nomenclature information alongside standardized analytical protocols. Accurate mass measurements, while highly precise, often lack the specificity needed to definitively identify the structure of a metabolite. This is why combining Mass Spectrometry Imaging (MSI) with tandem mass spectrometry imaging (MS2I) directly from tissue or with Liquid Chromatography-Mass Spectrometry/Mass Spectrometry (LC-MS/MS) of an adjacent homogenized tissue section is often necessary. Within metabolomics, tandem MS databases like MassBank, The National Institute of Standards and Technology (NIST), METLIN, Global Natural Products Social Molecular Networking (GNPS), mzCloud, Human Metabolome Database (HMDB), Spektraris, and ReSpect take center stage for metabolite identification and pathway assignment.[82] These meticulously assembled and maintained curated databases are instrumental in accurately classifying mass spectral features and linking them to specific metabolic pathways.

2. STUDY PLAN

The study focuses on metal allergies and uses mass spectrometry-based techniques to analyze metal complexes formed on everyday metallic objects like 1-euro coins. The main goal is to develop an analytical method to identify these metal complexes. The study also explores the direct impact of common metal allergens on the skin's metabolites and lipid composition.

A mass spectrometry workflow was developed to analyze metal-containing compounds formed on coins when exposed to artificial sweat, mimicking real-world scenarios. Tandem mass spectrometry (MS/MS) was crucial in identifying the various metal complexes present on the coin surface. The study also investigated the impact of sweat components on the formation of these complexes to pinpoint potential corrosion products that could contribute to skin allergies.

Significant Zn-, Cu-, and Ni-containing compounds were detected on the coin surface using AP-LDI MS imaging, validating the method's effectiveness. This method holds promise for analyzing a broad spectrum of metal complex classes on various everyday objects.

In addition, the study explored the effects of common metal allergens, particularly nickel, on skin metabolites and lipids using MALDI MSI for a detailed analysis of metabolic alterations induced by nickel exposure. A nickel staining method was developed and validated, offering insights into nickel's interaction with the skin and enhancing our understanding of nickel-induced allergic reactions.

These findings provide insights into nickel allergies and the interplay between metal exposure and lipid metabolism. These insights pave the way for developing targeted diagnostic and therapeutic strategies for individuals with nickel allergies. Future research directions include investigating the long-term effects of metal exposure on skin barrier function and immune responses. Additionally, exploring the impact of other common metal allergens on skin health represents a promising avenue for future studies.

By continuing to delve into these areas, we can improve the quality of life for individuals affected by metal allergies and develop more effective prevention and treatment strategies.

3. RESULTS and DISCUSSION

3.1 Mass spectrometric analysis of transition metal complexes formed through contact of artificial sweat with circulating Euro coins

Our study used three circulating 1-Euro coins from Spain, Germany, and France that were cleaned and treated with artificial sweat. These coins were chosen for initial experiments to evaluate if AP-LDI MS (atmospheric pressure laser desorption/ionization mass spectrometry) is suitable for detecting molecular and elemental components from the coin surfaces shown in Figure 4.

Figure 4. 1-euro coins from a) France 1992, b) Germany 2002 and Spain 2007.

Positively singly-charged nickel, copper, and zinc ions were detected. MS imaging of the 3D surface of a 1-Euro coin showed that Zn was most abundant in the outer ring, Cu was present in both inner and outer rings, Ni was found primarily in the inner ring, and several metal-organic compounds were readily detectable from the surface.

An exemplary AP-LDI MS imaging result of a cleaned 1-Euro coin is shown in Figure 5.

The signals at *m/z* 207.8941 ([$C_4HO_3NNi+K]^+$) and *m/z* 116.9527 ([$CH_4NZn+Na]^+$) are shown in red and green, respectively. The signals were assigned based on their accurate masses and isotopologue patterns using the XCalibur software.

Figure 5. 3D-surface red-green overlay MS image of m/z 207.8941 (red, [$C_4HO_3NNi+K]^+$), and m/z 116.9527 (green, [$CH_4NZn+Na]^+$). MS images of the two signals were generated from a cleaned 1-Euro coin (2002, Germany) with 320×189 pixels; 15 µm pixel size; m/z bin width: $\Delta(m/z)/(m/z)=\pm5$ ppm.

Pixel coverages, computed for three 1-Euro coins as a percentage of pixels with signal intensities of selected ions above a preset threshold value, are shown in Figure 6. As expected and consistent with reported coin compositions, Cu^+ ions had the highest pixel coverage, followed by zinc and nickel in the three coins.

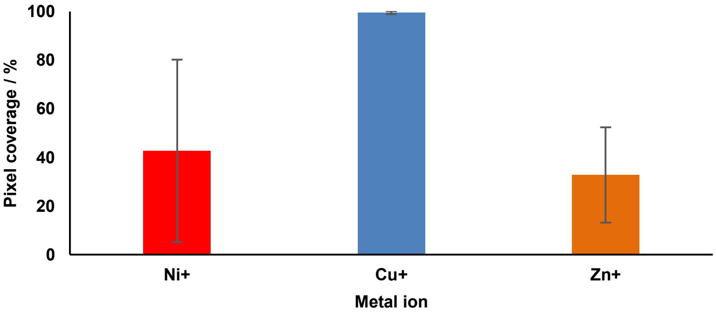

Figure 6. Average pixel coverages of Ni^+, Cu^+, and Zn^+ ions in the scanned area (see Figure 4) of three 1-Euro coins from Spain, Germany and France

A comparison of the three coins revealed that the pixel coverage of Ni^+ in the 1-Euro coin from France (1999) was higher than in the 1-Euro coins from Spain (2007) and Germany (2002) (Figure 7). We believe that the higher Ni^+ pixel coverage on the 1-Euro coin from France is because the French coin was produced in 1999, and the nickel directive guidelines, adopted in 1994, took effect in 2000 and have been implemented since 2001. Even if pixel coverage is not a quantitative measure for bulk concentration, these results demonstrate that AP-LDI MS can spatially probe metal appearances in coins and that these results align with reported region- and time-specific production processes.

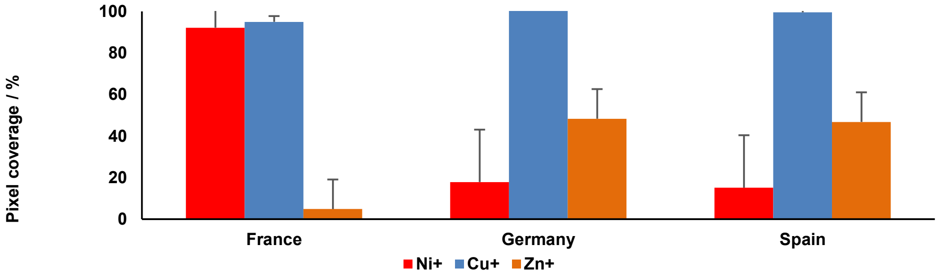

Figure 7. Pixel coverage percent of Ni$^+$, Cu$^+$, and Zn$^+$ ions in scanned area of 1 Euro coin France 1999, Germany 2002 and Spain 2007.

Besides metal ions, metal-organic ions from the coin surface were investigated. Examples besides those of Figure 8 are *m/z* 178.8832, assigned to $[CH_4NCu_2+Na]^+$, and *m/z* 258.8152, assigned to $[CH_5ONCu_3+Na]^+$. The signals were assigned based on their accurate masses and isotopologue patterns using the XCalibur software (for isotopologue patterns, MS images, and tandem mass spectrum; see Figures S2, S3, S4, S5 of the supporting information (SI) of the publication).

In addition, transition metal complexes formed during skin contact with Euro coins were studied. Since sweat can be essential in enhancing metal allergies, corrosion products produced by sweat on the surface of a 1-Euro coin were studied. In this study, three standard solutions, including urea (0.1 %), lactic acid (0.1 %), and artificial sweat solution (ASS), were sprayed homogeneously onto the surface of a cleaned 1-Euro coin.

After spraying the urea solution, the color of one of the coins changed to green in some parts after a day, as shown in Figure 9a, showing that metal ions had reacted with the urea solution.

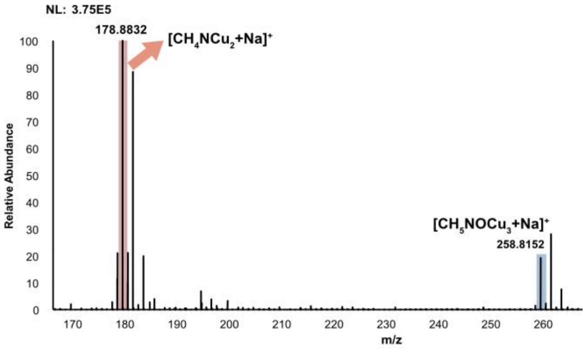

Figure 8. Positive-ion mode AP-LDI mass spectrum of m/z 178.8832 was assigned to $[CH_4NCu_2+Na]^+$ and m/z 258.8152 assigned to $[CH_5ONCu_3+Na]^+$. Spectra were generated from a cleaned 1-Euro coin (2002, Germany), averaging from 320×189 pixels; 15 µm pixel size.

AP-LDI MSI experiments probed the corrosion products on the surface and detected a signal at *m/z* 140.9720, assigned as $[CuCH_4N_2O+H_2O]^+$ (MS image before and after spraying ASS, see Figure 10; experimental and theoretical isotopologue patterns of $CuCH_4N_2O+H_2O]^+$, see SI Figure S8). Although the lactic acid solution did not cause any apparent change in the coin surface (Figure 9b), an unknown new signal at *m/z* 158.0821 was detected.

To confirm the identity of $[Cu(CH_4N_2O)+H_2O])^+$, formed on the surface of 1-Euro coins after spraying ASS, we compared tandem mass spectra from the surface (SI Figure S6) with those from the desired metal complex generated from a standard solution of 1 mol/L copper(II) chloride dihydrate ($CuCl_2 \cdot 2\ H_2O$) and 0.1 % (m/m) urea (Figure S7). α-cyano-4-hydroxycinnamic acid (CHCA, purity 97 %, Sigma-Aldrich, USA) was used as a matrix for tandem mass spectra of the standard. Due to the low signal intensity of the complex measured by AP-LDI from the surface, the isotopologue patterns from tandem measurements from the coin surface and the standard are only partly identical but still confirm the compound's identity.

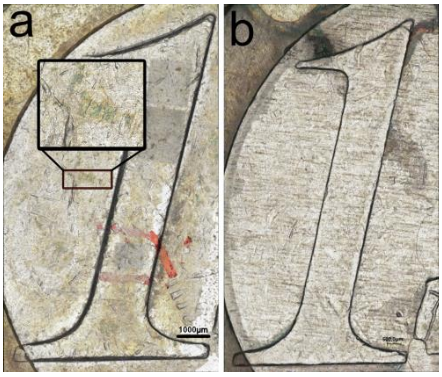

Figure 9. On a 1 Euro coin. a) urea 0.1 % solution, b) lactic acid 0.1 % solution after one day. The colour change is shown in a black rectangle, and the red marker shows the MALDI Mass Spectrometry analysis region.

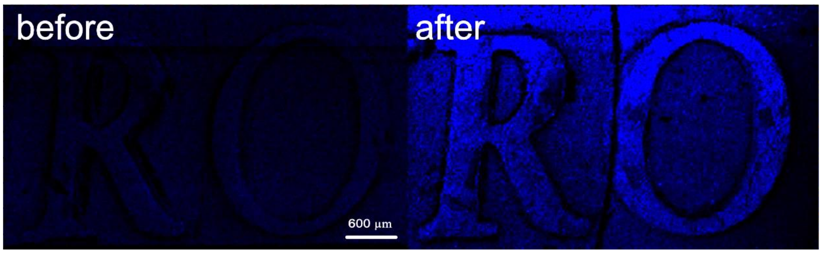

Figure 10. AP-LDI MS image of m/z 140.9728 (blue, $[Cu(CH_4N_2O)+H_2O])^+$) before and after spraying with ASS. MS images were generated with 325×193 pixels; 15 µm pixel size; m/z bin width: $\Delta(m/z)/(m/z)=\pm5$ ppm.

Compared to cleaned Euro coins, the relative abundance of Ni^+ and Cu^+ ions increased on the surface of coins sprayed with solutions of urea (1 g/L) and lactic acid (1 g/L). Comparing the relative abundances of metal ions on the surface showed that after three days, the lactic acid solution produced a higher concentration of Ni^+ and Cu^+ ions compared to the urea solution, while after six days, the urea solution yielded a higher concentration of Ni^+ and Cu^+ ions compared to the lactic acid solution. The results explain how lactic acid and urea impact the production of metal ions (by either oxidation of metals or by release from already oxidated metal compounds such as metal oxides or metal sulfides), particularly Cu^+ ions. As nickel allergy follows contact with the allergen, it can take 24 to 72 hours before symptoms manifest. These data suggest that acidic sweat can increase Ni^+ content in the first three days, resulting in an aggravated allergy, as shown in Figure 11.

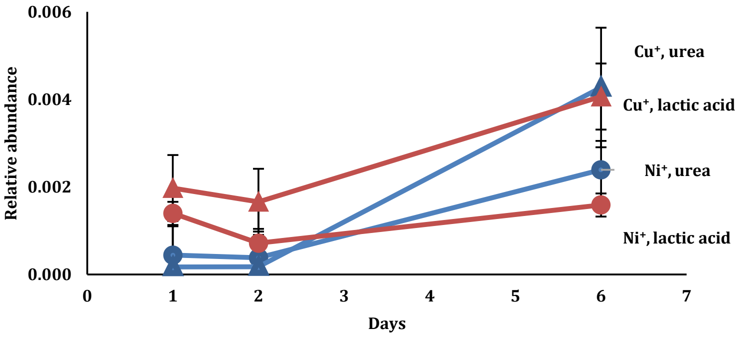

Figure 11. Relative abundance changes of Ni+ and Cu+ ions were detected after spraying coin surfaces with urea and lactic acid 0.1 % solutions for 6 days; signals normalized to TIC.

A comparison of the pixel coverages of the three metal ions on the scanned area before and after spraying ASS is shown in Figure 12.

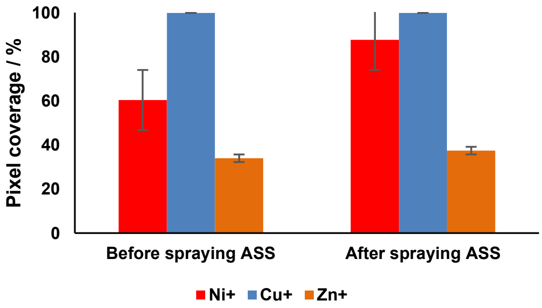

Figure 12. Pixel coverages of Ni^+, Cu^+, and Zn^+ ions in scanned areas before and after spraying ASS for 6 days.

Comparison of 3D-surface RGB MS images of the scanned area before and after spraying ASS also indicates the increase of pixel coverage of Ni^+ ions (Figure 13).

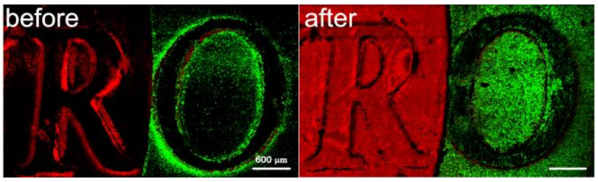

Figure 13. 3D-surface RGB MS images of m/z 57.93480 (red, $[Ni]^+$) and m/z 63.92860 (green, $[Zn]^+$), a) before and b) after spraying with ASS; m/z bin width: $\Delta(m/z)/(m/z) = \pm 5$ ppm

As shown by AP-LDI mass spectrometry, sweat increases the production of metal ions, especially nickel metal ions, which may play an important role in nickel allergy development. The increase of nickel metal ion abundances after one week is more influenced by urea, one of the main components of sweat, than by lactic acid.

3.2 Metabolipidomic changes induced by dermal nickel penetration determined in an ex vivo porcine ear skin model

Our study employed an *ex vivo* porcine ear skin model to comprehend the effects of nickel exposure on the skin. The well-known complexation reaction of nickel ions with dimethylglyoxime (H_2DMG) was used here to selectively stain nickel ions in skin cross-sections to track by light microscopy their penetration into the skin. MALDI MSI was used to study topographically the metabolomic and lipidomic profiles of control and nickel-treated skin. LC-MS/MS was utilized in parallel to reliably identify lipid species detected by MALDI MSI in the different skin layers.

CHAPTER I

The workflow of the study is shown in Figure 14. *Ex vivo* fresh porcine ear skin was organized into 4 cm^2 skin areas, and each area was treated with 30 µL nickel sulfate hexahydrate aqueous solutions of varying concentrations (1 $\%_w$, 5 $\%_w$, and 10 $\%_w$). Following a 2-hour open-air incubation in the oven at 32°C, punch biopsies measuring 15 mm in diameter were obtained and frozen at -80°C for future utilization. Frozen biopsies were sectioned at a thickness of 10 µm at -25 °C. After cryo-sectioning, skin cross-sections were covered with matrix by ultrafine spraying of a solution of 30 mg/mL α-Cyano-4-hydroxycinnamic acid (CHCA) in ACN/ H_2O /THF (70:30:0.1%, v:v:v). Metabolomic changes induced by nickel treatment were examined in positive-ion mode using an AP-SMALDI^5 AF ion source (TransMIT GmbH, Giessen, Germany) coupled to Q Exactive HF Orbitrap mass spectrometer (Thermo Fisher Scientific, Bremen, Germany).

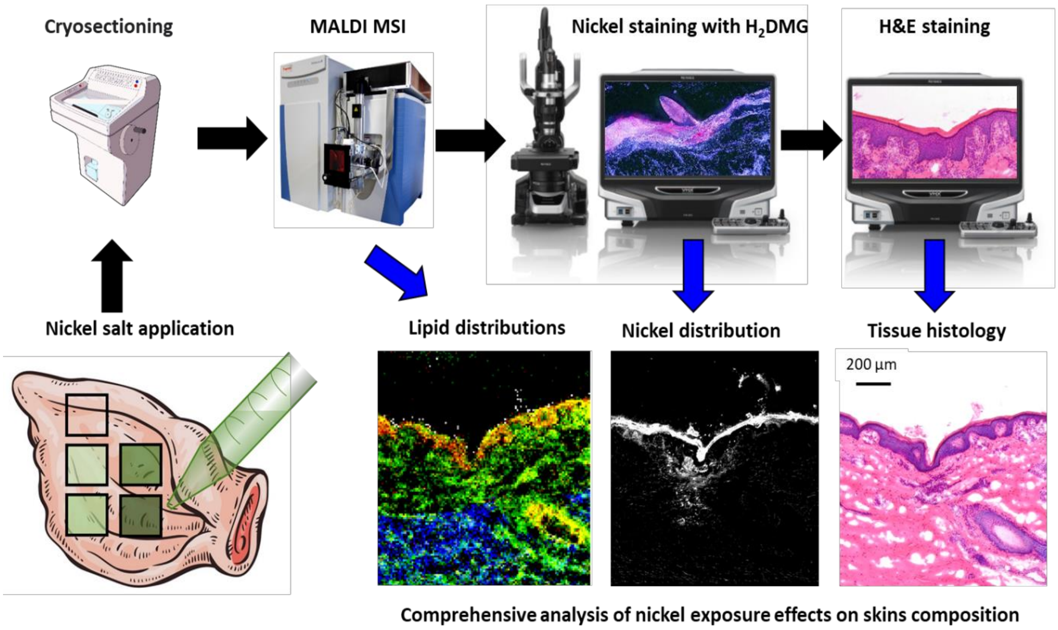

Figure 14. Experimental workflow illustrating the methodologies employed to investigate the effects of nickel exposure on skin. The study utilized ex vivo fresh porcine ear skin treated with nickel sulfate hexahydrate solutions of varying concentrations. After incubation, punch biopsies were taken, and tissues were processed for metabolomic and lipidomic analysis. MALDI MSI was used to examine metabolomic changes in skin cross-sections. Then, H_2DMG and H&E staining were employed to visualize nickel penetration and assess tissue morphology, respectively, by using a light microscope. LC-MS/MS was used for reliable lipid identification, allowing lipid class and fatty acid assignment (not shown).

Subsequently, the measured tissue sections were stained with H_2DMG to visualize nickel ion penetration, followed by light microscopy analysis. Afterward, H&E staining was performed to assess tissue morphology by light microscopy. The remaining tissue from cryo-sectioning was ground, and lipids were extracted for LC-MS/MS analysis to identify the fatty acid composition of the lipid species annotated by the METASPACE online platform in the MALDI MSI data sets.

Nickel ion penetration into pig ear skin

This study used nickel (II) sulfate hexahydrate in fresh pig ears as a model to simulate metal allergy responses in humans. Pig skin is very similar to human skin in its anatomy and thus is often used to study the effects of topically applied substances[86]. The microscopic anatomy of a pig ear cross-section and pig ear skin can be found in SI Figure S1. The skin layers most relevant for this study are the top, the stratum corneum, the viable epidermis (consisting of stratum granulosum, stratum spinosum, and stratum basale), and the dermis. The method for visualizing nickel penetration into pig skin using light microscopy is based on the complexation of H_2DMG with Ni^{2+} ions, forming nickel dimethylglyoxime square planar complexes ($Ni(HDMG)_2$) of pink color and low solubility in water (SI Figure S2a).[87] The reaction was first described in 1905 by L. Tschugajew and is a standard analytical method in classical qualitative and quantitative analysis[88], which is here applied for tissue staining. The semiquantitative performance of the H_2DMG staining method for tissue sections was evaluated for various nickel concentrations and biological replicates.

The workflow implemented to depict and measure the intensity of the pink color resulting from $Ni(HDMG)_2$ in the skin sections is outlined in SI Figure S2b. Initially, high-resolution images of samples treated with different nickel concentrations (0, 17, 84, and 167 µg/cm²) and stained by H_2DMG were captured by a light microscope under standardized lighting and magnification (250x). All images were converted to the same format (JPEG), maintaining consistent dimensions to ensure accurate comparison. Next, ImageJ software was used to split the images into red, green, and blue channels. To eliminate background interference from the tissue, the green channel was subtracted from the red channel (containing the $Ni(HDMG)_2$ signal). Finally, the total area and mean intensity of the derived gray-scale images showing only $Ni(HDMG)_2$ signal were measured, and the sum intensity was calculated.

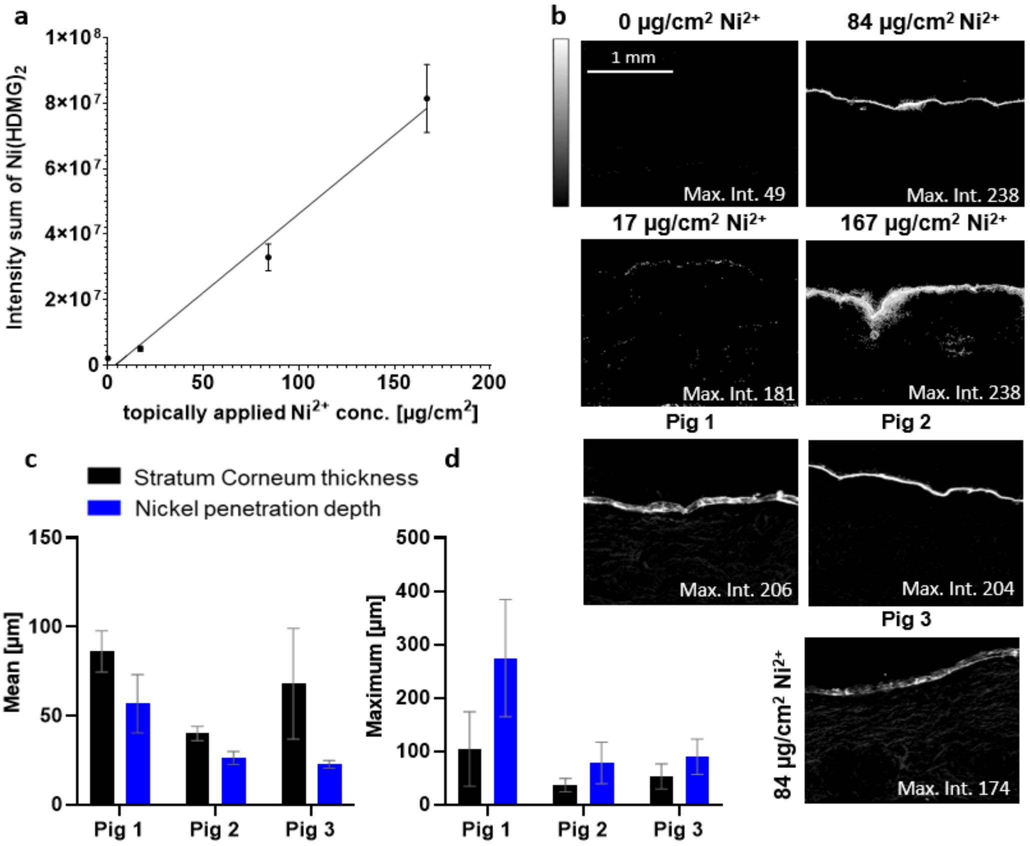

Figure 15. a) Intensity sum of Ni(HDMG)$_2$ complex for control and samples treated with 17, 84, and 167 µg/cm^2 of Ni^{2+} (one biological, three technical replicates), b) corresponding Ni(HDMG)$_2$ images of the samples (one technical replicate is shown), c) mean stratum corneum thickness (black) and mean nickel penetration depth (blue) for three biological replicates treated with 84 µg/cm^2 nickel ions (three technical replicates per biological replicate), d) Maximum nickel penetration depth and corresponding stratum corneum thickness for three biological replicates treated with 84 µg/cm^2 nickel ions (three technical replicates per biological replicate) as well as corresponding Ni(HDMG)$_2$ images of the samples (one technical replicate is shown). Error bars represent standard deviation.

Figure 15a shows the sum intensity of the Ni(HDMG)$_2$ complex for one biological replicate but three technical replicates, depending on the topically applied nickel concentration. The corresponding gray-scale images showing the distribution of Ni(HDMG)$_2$ in the skin cross-sections (one technical replicate) are depicted in Figure 15b. The sum intensity of Ni(HDMG)$_2$ increased linearly with Ni^{2+} concentration, with the highest intensity observed in the sample treated with 167 µg/cm² Ni^{2+} ($R^2 = 0.9292$). For concentrations up to 84 µg/cm², the applied nickel ions were predominately accumulated in the stratum corneum and barely detected in the viable epidermis. SI Figure S3 shows an overlay of Ni(HDMG)$_2$ distribution and H&E staining of the same skin cross-section treated with 84 µg/cm² Ni^{2+}.

In addition, the identity of the Ni(HDMG)$_2$ complex and its distribution in the skin cross-section was confirmed by positive-ion mode MALDI MSI. The [Ni(HDMG)$_2$+H]$^+$ ion was observed readily at *m/z* 289.0440 with the expected isotopic pattern of nickel. Microscopic and MALDI MS images revealed the same Ni(HDMG)$_2$ complex distribution in the stratum corneum (SI Figure S4). At 167 µg/cm² Ni^{2+} application, nickel ions penetrated deeper into the skin and were more often found in the viable epidermis and, to a small extent, in the dermis.

The nickel penetration depth was determined from the Ni(HDMG)$_2$ images of 84 µg/cm² Ni^{2+} treated skin samples (three technical replicates of three biological replicates) and compared to the stratum corneum thickness (Figure 15c and d). The Ni(HDMG)$_2$ distribution was strongly associated with the stratum corneum in all three biological replicates. Some penetration of nickel ions into the viable dermis was observed in one biological replicate. No Ni(HDMG)$_2$ signal was detected in the control skin cross-sections. The mean penetration depth of nickel ions was lower than the stratum corneum's mean thickness in each biological replicate (n=3) (Figure 2c). However, there were severe differences in the mean stratum corneum thickness (86, 40, and 68 µm) and nickel penetration depths (57, 26, and 23 µm) for different biological replicates. The maximum penetration depth of nickel ions was found to be, on average, about 2.3 times larger than the stratum corneum thicknesses at these measurement points, showing that trace levels of nickel ions cross the skin barrier, reaching viable epidermis and even dermis (Figure 15d). Overall, the data supports the method's effectiveness in detecting and quantifying nickel penetration. Compared to previous studies utilizing techniques such as TOF SIMS and ICP MS, the method developed in this study offers fast and cost-saving insights into nickel penetration mechanisms. Specifically, it provides valuable information on the localization of nickel within the skin's outermost layer.

Nickel-induced metabolomic and lipidomic changes in pig ear skin

Metabolites and lipids play a major role in the function of skin. Alterations to the metabolomic and lipidomic composition of the skin have been associated with various skin diseases. Nickel-induced lipidomic changes in the stratum corneum and viable epidermis have focused so far on MAGs, DAGs, and ceramides. Our study performed untargeted metabolomic and lipidomic analyses using MALDI MSI in the positive-ion mode on an *ex* *vivo* porcine ear skin model with a spatial resolution of 10 µm. Cross-sections of pig ear skin from three biological replicates treated with 84 µg/cm² nickel sulfate (topically applied) alongside untreated control pig ear skin were analyzed to discern the impact of nickel ion exposure on skin metabolite composition. The ion signals of the combined MALDI MSI data set (3 control + 3 nickel-treated samples) were annotated using METASPACE. In total, 536 ion signals were annotated using the databases LIPIDMAPS, swiss lipids, Human Metabolome Data Base (HMBD), and BraChem with a mass tolerance of ± 3 ppm, a false discovery rate of 10% and the following quasi-molecular ion: $[M+H]^+$, $[M+Na]^+$, $[M+K]^+$, $[M+NH_4]^+$. In addition, lipid extracts were prepared from the same tissues and analyzed with untargeted LC-MS/MS in positive-ion mode. 1012 lipids were identified by LipidMatchflow and 1063 by MSDial. *m/z* values of ions signal I annotated in the MALDI MSI data set with METASPACE were manually compared with m/z values found in the LC-MS/MS data set by LipidMatchflow and MSDial. 93 *m/z* values were found in both data sets and subjected to further analysis. After MALDI MSI, nickel ion distributions in the analyzed skin cross-section were determined by its reaction with H_2DMG, and tissue histology was obtained by subsequent H&E staining. Figure 16 shows the results from MALDI MSI (a), nickel staining with H_2DMG (b), and H&E staining (c) for control and an 84 µg/cm² nickel-treated sample. For MALDI MSI (Figure 16a), three MS images (with a mass tolerance of ±3 ppm, normalized to the total ion count (TIC)) were overlaid using the three native color channels (red, green, and blue) to illustrate the histology of the skin. Molecular markers for skin tissue layers were: *m/z* 522.4880, Cer-NS(d17:1/16:1), $[M + H]^+$ (red) for the stratum corneum; *m/z* 760.5851, PC(16:0/18:1), $[M + H]^+$ (blue) for dermis; and *m/z* 716.5225, PE(16:0/18:2), $[M + H]^+$ (green) for the viable epidermis. These markers were not influenced by the nickel treatment and reproduced well the histology of the skin cross-section as determined by H&E staining (Figure 16c). On the other hand, staining of the skin cross-sections with H_2DMG (Figure 16b) revealed nickel ion distribution strongly associated with the stratum corneum in the nickel-treated skin cross-section. In contrast, the control skin cross-section only showed some background noise.

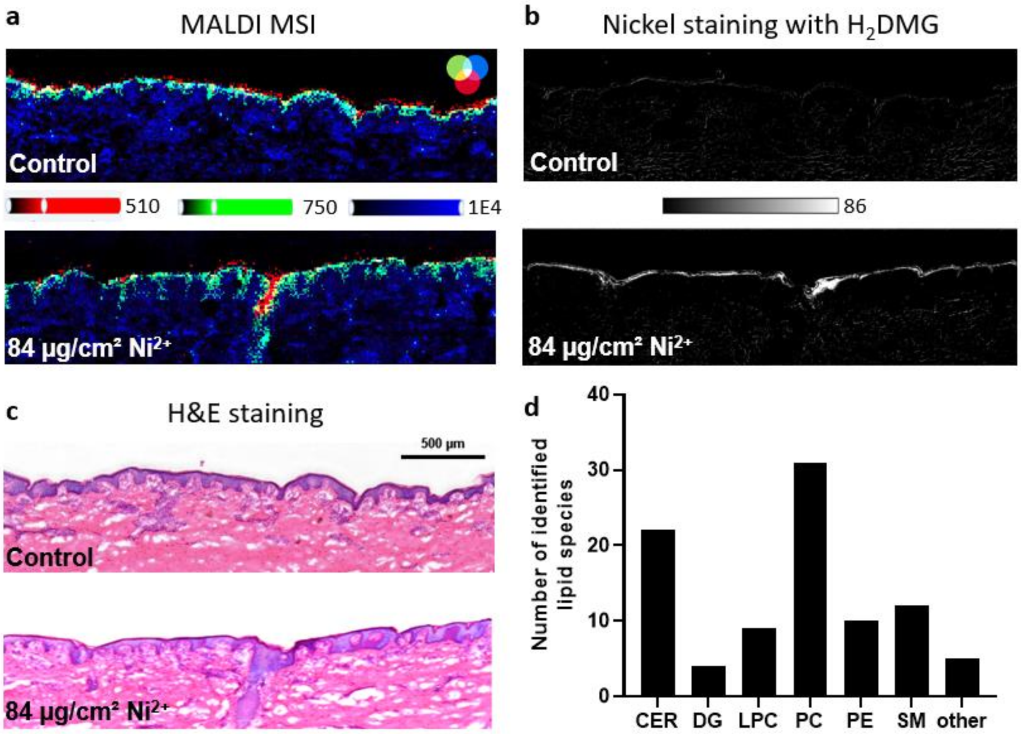

Figure 16. a) RGB overlay images of three lipids measured by MALDI MSI with a step size of 10 µm in positive-ion mode from a control sample (290 × 99 pixels) and an 84 µg/cm² nickel-treated sample (298 × 92 pixels): m/z 522.4880, Cer-NS(d17:1/16:1), $[M + H]^+$ (red), marker for stratum corneum; m/z 760.5851, PC(16:0/18:1), $[M + H]^+$ (blue), marker for dermis; and m/z 716.5225, PE(16:0/18:2), $[M + H]^+$ (green), marker for the viable epidermis. The data was normalized to TIC. b) Nickel distribution in a treated and a control sample was obtained by staining the samples with H_2DMG after MALDI MSI analysis. c) H&E staining of a control sample and an 84 µg/cm² nickel-treated sample subjected previously to MALDI MSI and nickel staining with H_2DMG. d) Number of lipid species per lipid class detected by MALDI MSI and further validated by LC MS/MS in nickel-treated and control groups.

Figure 16d shows the number of identified lipid species per lipid class: ceramides (CER, 22), diacylglycerols (DAG, 4), phosphatidylcholines (PC, 31), phosphatidylethanolamines (PE, 10), sphingomyelins (SM, 12) and lysophosphatidylcholines (LPC, 9).

Several lipid classes were readily accessible with MALDI MSI in positive-ion mode, ranging from small molecules like cholesterol at *m/z* 369.3515 to complex lipids such as TG (16:0/16:0/18:1) at *m/z* 855.7412. The high mass accuracy and mass resolution of the MALDI MSI data, in combination with LC-MS/MS data, allowed the reliable identification of individual lipid species, including the assignment of fatty acids. The results from MALDI MSI, nickel staining with H_2DMG, and H&E staining for all three biological replicates are shown in SI Figure S5.

The MALDI MSI data set described above was subjected to semi-quantitative analysis to identify which nickel ion treatment affects lipids and metabolites. The TIC-normalized mean intensities of all 93 identified lipids and two amino acids, arginine and histidine (identified by on-tissue MS/MS), were obtained from similar tissue areas (about 20.000-25.000 pixels) defined in SCILS Lab for the three control skin cross-sections and the three nickel-treated cross-sections. For each metabolite and lipid, a t-test was performed for the control versus nickel-treated group using the extracted TIC-normalized mean intensity values. A p-value smaller than 0.05 was considered significant. In total, 17 compounds were significantly downregulated in nickel-treated pig ear skin compared to control pig ear skin.

Changes in the lipid content were observed in all analyzed tissue layers (stratum corneum, viable epidermis, and dermis) and were not limited to those areas directly penetrated by nickel ions, indicating that response mechanisms are not dependent on direct contact with the trigger. In Figure 17, PC (16:0/16:0) (a), SM(d17:1/19:0) (b), and arginine (c) were selected as molecular markers to depict the decrease of ion intensities within the dermis, viable epidermis, and stratum corneum, respectively, after nickel exposure. Bar charts in Figure 17 d-f show the relative MALDI MSI intensities for all significantly down-regulated lipids and metabolites in relation to their main location (dermis, viable epidermis, and stratum corneum. The corresponding TIC-normalized ion images measured from three control and three nickel-treated samples can be found in SI Table S4. Notably, many of those lipids are structural lipids associated with the cell membranes belonging to sphingomyelin (SM) and phosphatidylcholine (PC) lipid classes. In addition, two PC species and four SM species feature odd-numbered fatty acids. The most abundant odd-numbered fatty acid features 17 carbons and one double bond. Fold-changes for downregulations ranged from 1.8 for arginine to 8.8 for SM(d17:1/22:0). Only arginine was found to be significantly downregulated in stratum corneum, but histidine and several ceramides showed a similar trend. Moreover, the observed downregulation of specific lipid species was dose-dependent. SI Figure S6 showed for one biological replicate decreasing signal intensities for arginine, histidine, SM(d18:1/20:0), and PC (16:0/18:0) with increasing nickel ion concentration (control, 42, 84, and 167 μg/cm^2).

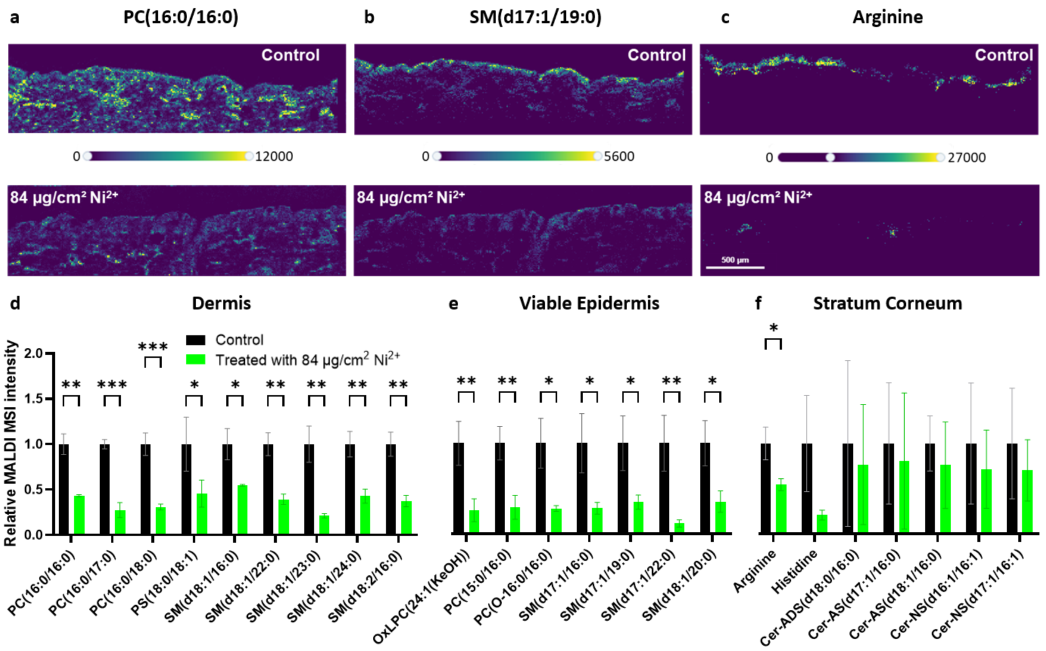

*Figure 17. Metabolites and lipids downregulated by nickel exposure. a)-c) MALDI MSI images of downregulated molecular markers a) for dermis: m/z 734.5694, (PC (16:0/16:0), [M+H]$^+$, b) for viable epidermis: m/z 731.6062, SM(d17:1/19:0), [M+H]$^+$ and c) stratum corneum: m/z 175.1190, arginine, [M+H]$^+$ (displayed m/z window: ±3 ppm). Depicted is a control skin sample with a size of 290 × 99 pixels and an 84 µg/cm^2 nickel-treated sample with a size of 298 × 92 pixels, acquired with a step size of 10 µm in positive-ion mode. d) Relative MALDI MSI intensities of metabolites and lipids significantly downregulated by nickel treatment in d) dermis, e) viable epidermis, and f) in stratum corneum. Relative MALDI MSI intensities were calculated by dividing mean intensities per sample by the average intensity of all control skin samples. Error bars show the standard deviation for three biological replicates. * p-value >0.05, ** p-value> 0.01 and *** p-value> 0.001. oxLPC(24:1(KeOH) refers to oxidized LPC, where KeOH represents a keto-hydroxy fatty acid.*

For the amino acids and ceramides, a localized effect in the stratum corneum was detected for one biological replicate with decreased molecular ion signals in areas with high nickel ion concentration (SI Figure S7). None of the 93 lipids semi-quantified in this study showed a significant up-regulation in the nickel-treated group.

Nickel ions, dissolved in water and deposited on the skin, first diffused into the stratum corneum. The middle of this layer is rich in arginine and serves as the first barrier for metal ions. [89] This barrier was also observed in our study for one biological replicate where the three stratum corneum layers were easily distinguished by microscopy, and most of the pink Ni(HDMG)$_2$ complex was found in the upper stratum corneum layer (SI Figure S8). Arginine is a natural moisturizing factor derived from filaggrin and is crucial to skin hydration. Our study found it to be significantly downregulated in stratum corneum upon nickel treatment, which aligns with findings observed using chromium salts instead of nickel salts.[89] In addition, several ceramides showed a similar trend as arginine. Ceramides are considered as “mortar” (together with cholesterol and free fatty acids) between the corneocytes, “bricks,” which build together the water-permeability barrier of the skin. A decrease of arginine and ceramides upon nickel treatment thus suggests damage to the skin’s barrier function. As demonstrated in this work, nickel ions penetrated in trace-level quantities into the viable epidermis and dermis, which is also in line with previous work. The lipid composition of the viable epidermis is dominated by phospholipids, especially phosphatidylcholines, and sphingomyelins. Phospholipids are membrane lipids. By their specific structure, they influence the fluidity and stiffness of the cell membranes and, therefore, their permeability. In addition, sphingomyelins form with cholesterol-specialized functional microdomains in the membrane, so-called “lipid rafts”. [90] Besides that, sphingomyelins are considered a reservoir for bioactive lipids such as free fatty acids, ceramides, sphingosine, ceramide-1-phosphate, and sphingosine-1-phosphate. [90] Each of them has its effect.[91] Metabolic pathways of ceramides, sphingomyelins, phosphatidylcholines, and their bioactive derivatives are highly interconnected. Changes in the concentration of any sphingolipid will result in changes in the concentration of other metabolites depending on the enzyme activity. Studies showed that any imbalance in ceramide/ sphingomyelin concentrations is leveled out by keratinocytes in vitro in about three hours and that fatty acids can be transferred between SMs and PCs. Therefore, the observed downregulation of PCs and SMs in the viable epidermis might result from changes in the ceramide concentrations of the stratum corneum. On the other hand, bioactive products might be generated from PCs and SMs, which trigger further immune responses. The fatty acid composition of skin lipids is unique among mammalian tissues.[92] Skin is enriched in odd-chained and branched fatty acids. 9.4% of the total fatty acids in human skin lipids are odd-chain fatty acids (OCFA). In addition, a proportion of fatty acids are unusual long-chain (so-called very long-chain fatty acids (22-26 carbons, VLCFA) and ultra-long chain fatty acids (> 26 carbons, ULCFA)) and/or have a double bond in unusual places. Functionally, these fatty acids pose metabolic problems to pathogens and improve the survival of only compatible microorganisms. Further, VLCFA and ULCFA contribute to the rigidity and impermeability of membranes and, thus, to the skin's barrier function.[93] In our study, several phosphatidylcholines and sphingomyelins containing OCFAs and

CHAPTER I

VLCFAs were found to be downregulated in viable epidermis and dermis. Possibly, they were degraded to bioactive lipids such as ceramides and free fatty acids to restore skin barrier function or trigger further immune responses.

CHAPTER I

4. CONCLUSION

ACD is a prevalent dermatological condition characterized by an allergic reaction to nickel-containing materials. So far, there is no clear understanding of how metals induce allergic reactions.

Our study has shown the effects of lactic acid and urea, the main components of sweat, on the surface of a 1-euro coin to identify corrosion products that might cause skin allergies. These data suggested that acidic sweat can increase Ni^+ content in the first three days, resulting in an aggravated allergy leading to the penetration of nickel ions into the skin. This penetration was visually confirmed using H_2DMG staining, which forms a pink complex with nickel, allowing us to track nickel's movement into the stratum corneum. Moreover, AP-LDI MS image of *m/z* 207.8941 $[C_4HO_3NNi+K]^+$, *m/z* 116.9527 $[CH_4NZn+Na]^+$ and *m/z* 140.9728 $[Cu(CH_4N_2O)+H_2O])^+$) showed that relevant Zn-, Cu- and Ni-containing compounds were detected with high signal intensities on the coin‘s surface.

Notably, our findings indicated that nickel exposure decreases essential lipid species, including sphingolipids and phosphatidylcholines, in the stratum corneum, epidermis, and dermis. These alterations suggest a disruption in the skin's barrier function, potentially contributing to the development of allergic reactions.

Our findings do not allow us to solve the health issues caused by nickel allergy; however, By elucidating the complex interactions between nickel ions and skin tissue at the molecular level, we can pave the way for more effective approaches to managing and preventing nickel-related dermatological conditions.

Future investigations should further elucidate the mechanisms of nickel penetration and its effects on skin lipid composition. By deepening our understanding of the complex interactions between nickel ions and skin tissue at the molecular level, we can improve patient care and develop more effective approaches to managing and preventing nickel-related dermatological conditions, ultimately enhancing the quality of life for those affected by nickel allergies.

CHAPTER I

5. REFERENCES

(1) Chen, J. K.; Thyssen, J. P. *Metal Allergy: From Dermatitis to Implant and Device Failure*; Springer, **2018**.

(2) Benvenuto, M. A. *Metals and Alloys: Industrial Applications*; Walter de Gruyter GmbH & Co KG, **2016**.

(3) Altmann, M.; Bartzsch, N. *The Volume of Euro Coins Held for Transaction Purposes in Germany*; ROME Discussion Paper Series, **2014**.

(4) Lidén, C.; Skare, L.; Vahter, M. Release of Nickel from Coins and Deposition onto Skin from Coin Handling - Comparing Euro Coins and SEK. *Contact Dermatitis.* **2008**, *59* (1), 31–37.

(5) Jomova, K.; Makova, M.; Alomar, S. Y.; Alwasel, S. H.; Nepovimova, E.; Kuca, K.; Rhodes, C. J.; Valko, M. Essential Metals in Health and Disease. *Chem. Biol. Interact.* **2022**, *367*, 110173.

(6) Awais, M.; Aziz, A.; Nazneen, A.; Wadood, A.; Rehman, M. A. U. A Review on the Recent Advancements on Therapeutic Effects of Metallic Ions in the Physiological Environments. **2022**.

(7) Swain, C. K. Environmental Pollution Indices: A Review on Concentration of Heavy Metals in Air, Water, and Soil near Industrialization and Urbanisation. *Discov. Environ.* **2024**, *2* (1), 5.

(8) Jyothi, N. R. Heavy Metal Sources and Their Effects on Human Health. *Heavy Met. Environ. Impacts Mitig.* **2020**, 1–12.

(9) Denkhaus, E.; Salnikow, K. Nickel Essentiality, Toxicity, and Carcinogenicity. *Crit. Rev. Oncol. Hematol.* **2002**, *42* (1), 35–56.

(10) Tramontana, M.; Bianchi, L.; Hansel, K.; Agostinelli, D.; Stingeni, L. Nickel Allergy: Epidemiology, Pathomechanism, Clinical Patterns, Treatment and Prevention Programs. *Endocrine, Metab. Immune Disord. Targets (Formerly Curr. Drug Targets-Immune, Endocr. Metab. Disord.* **2020**, *20* (7), 992–1002.

(11) Ahlström, M. G.; Thyssen, J. P.; Wennervaldt, M.; Menné, T.; Johansen, J. D. Nickel Allergy and Allergic Contact Dermatitis: A Clinical Review of Immunology, Epidemiology, Exposure, and Treatment. *Contact Dermatitis.* **2019**, *81* (4), 227–241.

CHAPTER I

(12) Garner, L. A. Contact Dermatitis to Metals. *Dermatol. Ther.* **2004**, *17* (4), 321–327.

(13) Saito, M.; Arakaki, R.; Yamada, A.; Tsunematsu, T.; Kudo, Y.; Ishimaru, N. Molecular Mechanisms of Nickel Allergy. *Int. J. Mol. Sci.* **2016**, *17* (2), 1–8.

(14) Magnano, G. C.; Marussi, G.; Crosera, M.; Hasa, D.; Adami, G.; Lionetti, N.; Larese Filon, F. Probing the Effectiveness of Barrier Creams against Human Skin Penetration of Nickel Powder. *Int. J. Cosmet. Sci.* **2024**, *46* (1), 39–50.

(15) Basketter, D. Nickel: Intrinsic Skin Sensitization Potency and Relation to Prevalence of Contact Allergy. *Dermat. contact, atopic, Occup. drug.* **2021**, *32* (2), 71–77.

(16) Torres, F.; das Graças, M.; Melo, M.; Tosti, A. Management of Contact Dermatitis Due to Nickel Allergy: An Update. *Clin. Cosmet. Investig. Dermatol.* **2009**, 39–48.

(17) Ahlström, M. G.; Thyssen, J. P.; Menné, T.; Johansen, J. D. Prevalence of Nickel Allergy in Europe Following the EU Nickel Directive – a Review. *Contact Dermatitis.* **2017**, *77* (4), 193–200.

(18) Riedel, F.; Aparicio-Soto, M.; Curato, C.; Thierse, H.-J.; Siewert, K.; Luch, A. Immunological Mechanisms of Metal Allergies and the Nickel-Specific TCR-PMHC Interface. *Int. J. Environ. Res. Public Health.* **2021**, *18* (20), 10867.

(19) Gorman, B. L.; Torti, S. V; Torti, F. M.; Anderton, C. R. Mass Spectrometry Imaging of Metals in Tissues and Cells: Methods and Biological Applications. *Biochim. Biophys. Acta (BBA)-General Subj.* **2024**, *1868* (2), 130329.

(20) Rezaei, A.; Heiles, S.; Spengler, B.; Schindler, S. Mass Spectrometric Analysis of Transition Metal Complexes Formed through Contact of Artificial Sweat with Circulating Euro Coins. *Zeitschrift für Anorg. und Allg. Chemie.* **2024**, *650* (4), e202300213.

(21) Blaser, P.; Rothmund, B.; Schmid, P.; Stadler, R.; Gemperle, C.; McCombie, G. Nickel Release from Metal Items in Contact with Skin: A Comparison of Methods and Practical Implications for Regulation in Europe. *J. Environ. Sci. Heal. Part A.* **2022**, *57* (1), 45–51.

(22) Martin, S. F.; Rühl-Muth, A.-C.; Esser, P. R. Orchestration of Inflammation in Contact Allergy by Innate Immune and Cellular Stress Responses. *Allergo J. Int.* **2024**, *33* (2), 41–48.

CHAPTER I

(23) Saito, M.; Arakaki, R.; Yamada, A.; Tsunematsu, T.; Kudo, Y.; Ishimaru, N. Molecular Mechanisms of Nickel Allergy. *International Journal of Molecular Sciences*. **2016**.

(24) Büdinger, L.; Hertl, M.; Büdinger, L. Immunologic Mechanisms in Hypersensitivity Reactions to Metal Ions: An Overview. *Allergy.* **2000**, *55* (2), 108–115.

(25) Rustemeyer, T. Immunological Mechanisms in Allergic Contact Dermatitis. *Curr. Treat. Options Allergy.* **2022**, *9* (2), 67–75.

(26) Su, C. T.-T.; Lua, W.-H.; Poh, J.-J.; Ling, W.-L.; Yeo, J. Y.; Gan, S. K.-E. Molecular Insights of Nickel Binding to Therapeutic Antibodies as a Possible New Antibody Superantigen. *Front. Immunol.* **2021**, *12*, 676048.

(27) Tan, C.-H.; Rasool, S.; Johnston, G. A. Contact Dermatitis: Allergic and Irritant. *Clin. Dermatol.* **2014**, *32* (1), 116–124.

(28) Panickar, K. S.; Bhathena, S. J. Control of Fatty Acid Intake and the Role of Essential Fatty Acids in Cognitive Function and Neurological Disorders.; Montmayeur, J.-P., le Coutre, J., Eds.; Boca Raton (FL), **2010**.

(29) Elias, P. M.; Wakefield, J. S. Skin Barrier Function. *Nutr. Heal. Ski. Strateg. Clin. Cosmet. Pract.* **2010**, 35–48.

(30) Elias, P. M.; Schmuth, M. Abnormal Skin Barrier in the Etiopathogenesis of Atopic Dermatitis. *Curr. Opin. Allergy Clin. Immunol.* **2009**, *9* (5), 437–446.

(31) Knox, S.; O'Boyle, N. M. Skin Lipids in Health and Disease: A Review. *Chem. Phys. Lipids.* **2021**, *236*, 105055.

(32) Agrawal, R.; Woodfolk, J. A. Skin Barrier Defects in Atopic Dermatitis. *Curr. Allergy Asthma Rep.* **2014**, *14* (5), 433.

(33) Simpson, E. L.; Chalmers, J. R.; Hanifin, J. M.; Thomas, K. S.; Cork, M. J.; McLean, W. H. I.; Brown, S. J.; Chen, Z.; Chen, Y.; Williams, H. C. Emollient Enhancement of the Skin Barrier from Birth Offers Effective Atopic Dermatitis Prevention. *J. Allergy Clin. Immunol.* **2014**, *134* (4), 818–823.

(34) Saunders, K.; Buse, B.; Kilburn, M. R.; Kearns, S.; Blundy, J. Nanoscale Characterisation of Crystal Zoning. *Chem. Geol.* **2014**, *364*, 20–32.

(35) Rinaldi, R.; Llovet, X. Electron Probe Microanalysis: A Review of the Past, Present, and Future. *Microsc. Microanal.* **2015**, *21* (5), 1053–1069.

(36) Hodoroaba, V.-D. Energy-Dispersive X-Ray Spectroscopy (EDS). In *Characterization of Nanoparticles*; Elsevier, **2020**, 397–417.

(37) Stewart, T. J. Across the Spectrum: Integrating Multidimensional Metal Analytics for: In Situ Metallomic Imaging. *Metallomics.* **2019**, *11* (1), 29–49.

(38) Bacquart, T.; Devès, G.; Carmona, A.; Tucoulou, R.; Bohic, S.; Ortega, R. Subcellular Speciation Analysis of Trace Element Oxidation States Using Synchrotron Radiation Micro-X-Ray Absorption near-Edge Structure. *Anal. Chem.* **2007**, *79* (19), 7353–7359.

(39) McRae, R.; Bagchi, P.; Sumalekshmy, S.; Fahrni, C. J. In Situ Imaging of Metals in Cells and Tissues. *Chem. Rev.* **2009**, *109* (10), 4780–4827.

(40) Hare, D. J.; New, E. J.; de Jonge, M. D.; McColl, G. Imaging Metals in Biology: Balancing Sensitivity, Selectivity and Spatial Resolution. *Chem. Soc. Rev.* **2015**, *44* (17), 5941–5958.

(41) Buchberger, A. R.; DeLaney, K.; Johnson, J.; Li, L. Mass Spectrometry Imaging: A Review of Emerging Advancements and Future Insights. *Anal. Chem.* **2018**, *90* (1), 240.

(42) Bernius, M. T.; Morrison, G. H. Mass Analyzed Secondary Ion Microscopy. *Rev. Sci. Instrum.* **1987**, *58* (10), 1789–1805.

(43) Orellana, F. A.; Gálvez, C. G.; Roldán, M. T.; García-Ruiz, C. Applications of Laser-Ablation-Inductively-Coupled Plasma-Mass Spectrometry in Chemical Analysis of Forensic Evidence. *TrAC Trends Anal. Chem.* **2013**, *42*, 1–34.

(44) Spengler, B.; Hubert, M.; Kaufmann, R. MALDI ion imagng and biological ion imaging with a new scanning UV-laser microprobe. 42nd ASMS Conference on Mass Spectrometry and Allied Topics, Chicago, Illinois **1994**, 1041.

(45) Xiao, Y.; Deng, J.; Yao, Y.; Fang, L.; Yang, Y.; Luan, T. Recent Advances of Ambient Mass Spectrometry Imaging for Biological Tissues: A Review. *Anal. Chim. Acta.* **2020**, *1117*, 74–88.

(46) Linton, R. W.; Goldsmith, J. G. The Role of Secondary Ion Mass Spectrometry (SIMS) in Biological Microanalysis: Technique Comparisons and Prospects. *Biol. Cell.* **1992**, *74* (1), 147–160.

(47) Lee, R. F. S.; Theiner, S.; Meibom, A.; Koellensperger, G.; Keppler, B. K.; Dyson,

P. J. Application of Imaging Mass Spectrometry Approaches to Facilitate Metal-Based Anticancer Drug Research. *Metallomics.* **2017**, *9* (4), 365–381.

(48) Liu, X.; Hummon, A. B. Chemical Imaging of Platinum-Based Drugs and Their Metabolites. *Sci. Rep.* **2016**, *6* (1), 38507.

(49) de Macedo, C. S.; Anderson, D. M.; Schey, K. L. MALDI (Matrix Assisted Laser Desorption Ionization) Imaging Mass Spectrometry (IMS) of Skin: Aspects of Sample Preparation. *Talanta.* **2017**, *174*, 325–335.

(50) Chughtai, K.; Heeren, R. M. A. Mass Spectrometric Imaging for Biomedical Tissue Analysis. *Chem. Rev.* **2010**, *110* (5), 3237–3277.

(51) Zavalin, A.; Yang, J.; Hayden, K.; Vestal, M.; Caprioli, R. M. Tissue Protein Imaging at 1 μm Laser Spot Diameter for High Spatial Resolution and High Imaging Speed Using Transmission Geometry MALDI TOF MS. *Anal. Bioanal. Chem.* **2015**, *407*, 2337–2342.

(52) Kompauer, M.; Heiles, S.; Spengler, B. Atmospheric Pressure MALDI Mass Spectrometry Imaging of Tissues and Cells at 1.4-μm Lateral Resolution. *Nat. Methods.* **2017**, *14* (1), 90–96.

(53) Kompauer, M.; Heiles, S.; Spengler, B. Chemical and Topographical 3D Surface Profiling Using Atmospheric Pressure LDI and MALDI MS Imaging. *Protoc. Exch.* **2017**.

(54) Gerbig, S.; Brunn, H. E.; Spengler, B.; Schulz, S. Spatially Resolved Investigation of Systemic and Contact Pesticides in Plant Material by Desorption Electrospray Ionization Mass Spectrometry Imaging (DESI-MSI). *Anal. Bioanal. Chem.* **2015**, *407*, 7379–7389.

(55) Rubakhin, S. S.; Sweedler, J. V. A Mass Spectrometry Primer for Mass Spectrometry Imaging. *Mass Spectrom. Imaging Princ. Protoc.* **2010**, 21–49.

(56) Eliuk, S.; Makarov, A. Evolution of Orbitrap Mass Spectrometry Instrumentation. *Annu. Rev. Anal. Chem.* **2015**, *8*, 61–80.

(57) Hayasaka, T.; Goto-Inoue, N.; Sugiura, Y.; Zaima, N.; Nakanishi, H.; Ohishi, K.; Nakanishi, S.; Naito, T.; Taguchi, R.; Setou, M. Matrix-assisted Laser Desorption/Ionization Quadrupole Ion Trap Time-of-flight (MALDI-QIT-TOF)-based Imaging Mass Spectrometry Reveals a Layered Distribution of Phospholipid

Molecular Species in the Mouse Retina. *Rapid Commun. Mass Spectrom. An Int. J. Devoted to Rapid Dissem. Up-to-the-Minute Res. Mass Spectrom.* **2008**, *22* (21), 3415–3426.

(58) Allen, D. R.; McWhinney, B. C. Quadrupole Time-of-Flight Mass Spectrometry: A Paradigm Shift in Toxicology Screening Applications. *Clin. Biochem. Rev.* **2019**, *40* (3), 135.

(59) Aichler, M.; Walch, A. MALDI Imaging Mass Spectrometry: Current Frontiers and Perspectives in Pathology Research and Practice. *Lab. Investig.* **2015**, *95* (4), 422–431.

(60) Perry, R. H.; Cooks, R. G.; Noll, R. J. Orbitrap Mass Spectrometry: Instrumentation, Ion Motion and Applications. *Mass Spectrom. Rev.* **2008**, *27* (6), 661–699.

(61) Schwaiger-Haber, M.; Stancliffe, E.; Arends, V.; Thyagarajan, B.; Sindelar, M.; Patti, G. J. A Workflow to Perform Targeted Metabolomics at the Untargeted Scale on a Triple Quadrupole Mass Spectrometer. *ACS Meas. Sci. Au.* **2021**, *1* (1), 35–45.

(62) Meicheng, L.; Antoine, S.; Frédéric, W.; Marcus, P.; Jolanta, Ś. Localized Corrosion Induced Surface Modifications of Al-Cu-Li Alloy Studied by ToF-SIMS 3D Imaging. *Npj Mater. Degrad.* **2021**, *5* (1).

(63) Malmberg, P.; Guttenberg, T.; Ericson, M. B.; Hagvall, L. Imaging Mass Spectrometry for Novel Insights into Contact Allergy – a Proof-of-Concept Study on Nickel. *Contact Dermatitis.* **2018**, *78* (2), 109–116.

(64) Hagvall, L.; Pour, M. D.; Feng, J.; Karma, M.; Hedberg, Y.; Malmberg, P. Skin Permeation of Nickel, Cobalt and Chromium Salts in Ex Vivo Human Skin, Visualized Using Mass Spectrometry Imaging. *Toxicol. Vitr.* **2021**, *76* (July), 105232.

(65) Bluestein, B. M.; Morrish, F.; Graham, D. J.; Huang, L.; Hockenbery, D.; Gamble, L. J. Analysis of the Myc-Induced Pancreatic β Cell Islet Tumor Microenvironment Using Imaging ToF-SIMS. *Biointerphases.* **2018**, *13* (6).

(66) Legin, A. A.; Schintlmeister, A.; Jakupec, M. A.; Galanski, M. S.; Lichtscheidl, I.; Wagner, M.; Keppler, B. K. NanoSIMS Combined with Fluorescence Microscopy as a Tool for Subcellular Imaging of Isotopically Labeled Platinum-Based Anticancer Drugs. *Chem. Sci.* **2014**, *5* (8), 3135–3143.

(67) Sabine Becker, J. Imaging of Metals in Biological Tissue by Laser Ablation Inductively Coupled Plasma Mass Spectrometry (LA–ICP–MS): State of the Art and Future Developments. *J. mass Spectrom.* **2013**, *48* (2), 255–268.

(68) Becker, J. S.; Breuer, U.; Hsieh, H.-F.; Osterholt, T.; Kumtabtim, U.; Wu, B.; Matusch, A.; Caruso, J. A.; Qin, Z. Bioimaging of Metals and Biomolecules in Mouse Heart by Laser Ablation Inductively Coupled Plasma Mass Spectrometry and Secondary Ion Mass Spectrometry. *Anal. Chem.* **2010**, *82* (22), 9528–9533.

(69) Strekopytov, S.; Billimoria, K.; Goenaga-Infante, H. A Systematic Study of High Resolution Multielemental Quantitative Bioimaging of Animal Tissue Using LA-ICP-TOFMS. *J. Anal. At. Spectrom.* **2023**, *38* (3), 704–715.

(70) Pamphlett, R.; Satgunaseelan, L.; Kum Jew, S.; Doble, P. A.; Bishop, D. P. Elemental Bioimaging Shows Mercury and Other Toxic Metals in Normal Breast Tissue and in Breast Cancers. *PLoS One.* **2020**, *15* (1), e0228226.

(71) Köfeler, H. C.; Fauland, A.; Rechberger, G. N.; Trötzmüller, M. Mass Spectrometry Based Lipidomics: An Overview of Technological Platforms. *Metabolites.* **2012**, *2* (1), 19–38.

(72) Dettmer, K.; Aronov, P. A.; Hammock, B. D. Mass Spectrometry-based Metabolomics. *Mass Spectrom. Rev.* **2007**, *26* (1), 51–78.

(73) Karnovsky, A.; Li, S. Pathway Analysis for Targeted and Untargeted Metabolomics. *Comput. methods data Anal. metabolomics.* **2020**, 387–400.

(74) Scalbert, A.; Brennan, L.; Fiehn, O.; Hankemeier, T.; Kristal, B. S.; van Ommen, B.; Pujos-Guillot, E.; Verheij, E.; Wishart, D.; Wopereis, S. Mass-Spectrometry-Based Metabolomics: Limitations and Recommendations for Future Progress with Particular Focus on Nutrition Research. *Metabolomics.* **2009**, *5*, 435–458.

(75) Vuckovic, D. Current Trends and Challenges in Sample Preparation for Global Metabolomics Using Liquid Chromatography–Mass Spectrometry. *Anal. Bioanal. Chem.* **2012**, *403* (6), 1523–1548.

(76) Vuckovic, D. Chapter 4 - Sample Preparation in Global Metabolomics of Biological Fluids and Tissues; Issaq, H. J., Veenstra, T. D. B. T.-P. and M. A. to B. D. (Second E., Eds.; Academic Press: Boston, **2020**; 53–83.

(77) Raterink, R.-J.; Lindenburg, P. W.; Vreeken, R. J.; Ramautar, R.; Hankemeier, T.

Recent Developments in Sample-Pretreatment Techniques for Mass Spectrometry-Based Metabolomics. *TrAC Trends Anal. Chem.* **2014**, *61*, 157–167.

(78) Zhang, J.; Hu, B. Liquid-Liquid Extraction (LLE). *Sep. Purif. Technol. biorefineries* **2013**, 61–78.

(79) Liu, R.; Chou, J.; Hou, S.; Liu, X.; Yu, J.; Zhao, X.; Li, Y.; Liu, L.; Sun, C. Evaluation of Two-Step Liquid-Liquid Extraction Protocol for Untargeted Metabolic Profiling of Serum Samples to Achieve Broader Metabolome Coverage by UPLC-Q-TOF-MS. *Anal. Chim. Acta.* **2018**, *1035*, 96–107.

(80) Leuthold, P.; Schaeffeler, E.; Winter, S.; Büttner, F.; Hofmann, U.; Mürdter, T. E.; Rausch, S.; Sonntag, D.; Wahrheit, J.; Fend, F. Comprehensive Metabolomic and Lipidomic Profiling of Human Kidney Tissue: A Platform Comparison. *J. Proteome Res.* **2017**, *16* (2), 933–944.

(81) Zhang, X.; Li, Q.; Dou, J. Mass Spectrometry-Based Metabolomics in Health and Medical Science: A Systematic Review. *RSC Adv.* **2020**, *10* (6), 3092–3104.

(82) Collins, S. L.; Koo, I.; Peters, J. M.; Smith, P. B.; Patterson, A. D. Current Challenges and Recent Developments in Mass Spectrometry–Based Metabolomics. *Annu. Rev. Anal. Chem.* **2021**, *14* (1), 467–487.

(83) Denisov, E.; Damoc, E.; Lange, O.; Makarov, A. Orbitrap Mass Spectrometry with Resolving Powers above 1,000,000. *Int. J. Mass Spectrom.* **2012**, *325*, 80–85.

(84) Hendrickson, C. L.; Quinn, J. P.; Kaiser, N. K.; Smith, D. F.; Blakney, G. T.; Chen, T.; Marshall, A. G.; Weisbrod, C. R.; Beu, S. C. 21 Tesla Fourier Transform Ion Cyclotron Resonance Mass Spectrometer: A National Resource for Ultrahigh Resolution Mass Analysis. *J. Am. Soc. Mass Spectrom.* **2015**, *26* (9), 1626–1632.

(85) Spengler, B. Mass Spectrometry Imaging of Biomolecular Information. *Anal. Chem.* **2015**, *87* (1), 64–82.

(86) Khiao In, M.; Richardson, K. C.; Loewa, A.; Hedtrich, S.; Kaessmeyer, S.; Plendl, J. Histological and Functional Comparisons of Four Anatomical Regions of Porcine Skin with Human Abdominal Skin. *Anat. Histol. Embryol.* **2019**, *48* (3), 207–217.

(87) Julander, A.; Skare, L.; Vahter, M.; Lidén, C. Nickel Deposited on the Skin–Visualization by DMG Test. *Contact Dermatitis.* **2011**, *64* (3), 151–157.

(88) Tschugaeff, L. Ueber Ein Neues, Empfindliches Reagens Auf Nickel. *Berichte der*

Dtsch. Chem. Gesellschaft. **1905**, *38* (3), 2520–2522.

(89) Kubo, A.; Ishizaki, I.; Kubo, A.; Kawasaki, H.; Nagao, K.; Ohashi, Y.; Amagai, M. The Stratum Corneum Comprises Three Layers with Distinct Metal-Ion Barrier Properties. *Sci. Rep.* **2013**, *3*, 1–11.

(90) Wanner, R.; Peiser, M.; Wittig, B. Keratinocytes Rapidly Readjust Ceramide–Sphingomyelin Homeostasis and Contain a Phosphatidylcholine–Sphingomyelin Transacylase. *J. Invest. Dermatol.* **2004**, *122* (3), 773–782.

(91) Vietri Rudan, M.; Watt, F. M. Mammalian Epidermis: A Compendium of Lipid Functionality. *Front. Physiol.* **2022**, *12*.

(92) Nicolaides, N. Skin Lipids: Their Biochemical Uniqueness. *Science (80-.).* **1974**, *186* (4158), 19–26.

(93) Zwara, A.; Wertheim-Tysarowska, K.; Mika, A. Alterations of Ultra Long-Chain Fatty Acids in Hereditary Skin Diseases—Review Article. *Front. Med.* **2021**, *8* (August), 1–21.

CHAPTER II

1. Mass spectrometric analysis of transition metal complexes formed through contact of artificial sweat with circulating Euro coins

Rezaei, A.; Heiles, S.; Spengler, B.; Schindler, S. Mass Spectrometric Analysis of Transition Metal Complexes Formed through Contact of Artificial Sweat with Circulating Euro Coins. *Zeitschrift für Anorg. und Allg. Chemie* **2024**, *650* (4), e202300213.

Journal of Inorganic and General Chemistry
ZAAC
Zeitschrift für anorganische und allgemeine Chemie
www.zaac.wiley-vch.de
RESEARCH ARTICLE

DOI: 10.1002/zaac.202300213

Special Issue

Mass spectrometric analysis of transition metal complexes formed through contact of artificial sweat with circulating Euro coins

Azar Rezaei,[a] Sven Heiles,[b, c] Bernhard Spengler,*[a] and Siegfried Schindler*[a]

Dedicated to Professor Rhett Kempe on the occasion of his 60th birthday.

It is well-known that some metals/alloys sensitize the skin of susceptible individuals. Trace amounts of metals and chemical compounds containing metal ions can affect human health, i.e., cause allergy or inflammation. However, the details of this metal-induced allergic reaction are not well understood. Complexes of nickel, copper, and zinc are known to be easily formed through contact of metal alloys with ubiquitously available organic compounds such as triacylglycerols, amino acids, urea, and fatty acids found in skin secretions or skin care products. Thus, an analytical technique is required to characterize and identify metal complexes formed on metallic everyday products, ideally offering a chemically specific, laterally resolved view of allergy-causing processes. Here we present a mass-spectrometry-based analytical workflow to characterize metal-containing compounds formed on the surface of 1-euro coins when in contact with artificial sweat. This study identified different metal complexes by using tandem mass spectrometry (MS/MS). Surface imaging of 1-Euro coins employing laser-based mass spectrometry revealed the lateral distribution of Zn, Cu, and Ni complexes with low-micrometer resolution.

Introduction

Nickel ions with physiologically relevant ligands in small concentrations are spectroscopically difficult to detect. Therefore, nickel was not considered an element of biological importance for long.[1] However, the evidence of the essentiality of this element for plants goes back to the ’70s of the twentieth century, when a group of researchers suggested the possible role of Ni in the metabolism of nitrogen through its participation in the structure of the enzyme urease.[2] In the 1980s, Eskew et al.,[3] demonstrated the essential role of Ni in the nitrogen metabolism of leguminous plants (soybeans), a role that was independent of the form of available nitrogen (NO$_3^-$ or NH$_4^+$). The evidence generated by this research suggested the essentiality of Ni for higher plants. Nickel ions are required for the active synthesis and metabolism of urease in plant cells such as jack beans (*Canavalia sp.*), soybeans (*Glycine max*), rice (*Oryza sativa*), and tobacco (*Nicotiana tabacum*).[4]

Since then, nickel chemistry in biological systems has been intensively investigated, and several nickel-dependent enzymes have been discovered. Nickel is now considered an essential element in the active site of enzymes of animals, microorganisms, and plants.[5] Furthermore, it is suggested to be an essential micronutrient for the proper function of the human body.[6] However, nickel is also a toxin and it is thus important to better understand why cells select nickel ions among a pool of different and more readily available metal ions.

Gastritis can often be caused by the bacterium *Helicobacter pylori*,[7] which a urease test can detect. Nickel-containing urease contains two nickel(II) ions in the active site, forms carbon dioxide and ammonia (which protects *Helicobacter* against the stomach's hydrochloric acid), and a color change of an indicator simply detects ammonia.

Besides its biological occurrence, nickel furthermore is released into the environment by anthropogenic sources such as the combustion of fossil fuels (coal-fired power plants or the combustion of fossil oil)[8] and from mining as well as from agriculture (especially fertilizers).[9] People can develop allergies to some metals; nickel is one of the most common causes of allergic contact dermatitis.[10] Exposure typically occurs from

---

[a] *A. Rezaei, Prof. Dr. B. Spengler, Prof. Dr. S. Schindler*
Institute of Inorganic and Analytical Chemistry
Justus Liebig University Gießen
Heinrich-Buff-Ring 17, 35392 Gießen
Germany
Fax: (+49) 641-99-34809
E-mail: siegfried.schindler@anorg.chemie.uni-giessen.de
bernhard.spengler@anorg.chemie.uni-giessen.de
[b] *Prof. Dr. S. Heiles*
Leibniz-Institut für Analytische Wissenschaften – ISAS – e.V.
44139 Dortmund
Germany
[c] *Prof. Dr. S. Heiles*
Lipidomics, Faculty of Chemistry, University of Duisburg-Essen
45141 Essen
Germany

Supporting information for this article is available on the WWW under https://doi.org/10.1002/zaac.202300213

This article is part of a Special Collection dedicated to Professor Rhett Kempe on the occasion of his 60th birthday. Please see our homepage for more articles in the collection.

metallic items such as household products, jewellery, or coins.[11] The reaction of a nickel-allergic person, after contact with nickel items, is a local skin rush (Figure 1), that usually disappears after a few days.

However, much more severe effects can develop.[12] Molecular mechanisms of nickel allergy have been investigated.[13] Tests for a nickel allergy are usually done by exposing the individual to a small amount of a diluted nickel sulfate solution (tape stripping).[14] The sensitization and elicitation thresholds for nickel allergy and dermatitis differ at least 250 – fold, making it impossible to define a safe threshold level.[11a] There is a significant variation in the degree of sensitivity to nickel between individuals. Even tiny amounts of nickel can cause a reaction in nickel-allergic individuals.

Nickel allergy and dermatitis are sought to be prevented by limiting nickel exposure from items used for prolonged contacts. Nickel release is measured by a test technique called EN 1811 in which the test object is placed in an artificial sweat solution for one week, after which it is measured by atomic absorption spectroscopy or another suitable method.[10] According to the 'Nickel Directive', jewellery and other products intended to come into direct and prolonged contact with the skin shall not release too much nickel. In the case of post assemblies inserted into pierced ears and other pierced parts of the body, this should be less than 0.2 $\mu g/cm^2$/week and 0.5 $\mu g/cm^2$/week for other products destined for direct and prolonged contact.

While the first coins were made of precious metals such as gold and silver, less expensive metals such as copper and nickel were used soon after. For example, the 5-cent coin in the US, called a nickel, consists today of 75% copper and 25% nickel. This alloy is widely used for coins due to its silver color, corrosion resistance, resilience, and durability.[15] The compositions of coins often changed over time. Currently, nickel is widely used in the coins of the European Union. A total of two alloys are included in the metal composition of coins in circulation in the EU countries as of 2012. The main characteristics of the 1 Euro coin are a diameter of 23.25 mm, a thickness of 2.33 mm, and a mass of 7.5 g.[16] It contains a metallic outer ring that appears yellow (nickel brass), consisting of 75% copper, 20% zinc, and 5% nickel (Figure 2).

Figure 1. Skin rush of a nickel-allergic person in our lab after wearing a lab coat with buttons attached to nickel-containing metal rings.

The white alloy in the center (cupro nickel) is 75% copper with 25% nickel. The composition of 1-euro coins can vary slightly, depending on the country that issues the coin. The skin contact of both alloys could, thus, potentially cause an allergic reaction in people sensitized by nickel. An increase in contact dermatitis has raised concerns because of the introduction of the new Euro coins in 2002.[17]

It is well known that to cause an allergic reaction, enough of the allergenic metal must be dissolved to enter the body through the skin. Solubilization of the allergenic metal (forming ions) can occur due to corrosion of the metal (or alloy) by itself or by body fluids. The corrosion rate, duration, and frequency of skin contact, nature, and concentration of the dissolved allergenic metal ions, play an important role in determining the extent of an allergic reaction.[15]

Several factors affect nickel release from coins, including the composition of the coins, their size, the solvents, and the immersion duration and temperature. A simple spot test for nickel release from surfaces is applying a solution of dimethylglyoxime (DMG), which gives a positive test due to the characteristic color of the formed nickel complex (Figure 3), well known in basic analytical chemistry protocols, where it can be used to quantify nickel gravimetrically. The test can also be used after the skin has been exposed to metal.[18]

In a quantitative nickel-release test (EN 1811), 1- and 2-Euro coins released approximately a mean of 86 $\mu g/cm^2$/week and a

Figure 2. 1-euro coins from a) France 1992, b) Germany 2002 and Spain 2007.

Figure 3. Formation of the nickel dimethylglyoximate complex on a cotton swap.

Journal of Inorganic and General Chemistry
ZAAC
Zeitschrift für anorganische und allgemeine Chemie
RESEARCH ARTICLE

mean of 99 μg/cm^2/week, respectively.[19] Therefore, the nickel release from the present 1- and 2-Euro coins exceeds the acceptable threshold for prolonged contact with human skin, which is considered to be potentially harmful to individuals with nickel allergies or sensitivities. Hence, coin handling is probably contributing to nickel dermatitis. To determine how much nickel and other metals have been deposited on the skin, two sampling methods were developed: finger immersion and acid wipe sampling. The amount of nickel present on the fingers of players, cashiers, sales assistants, caterers, and office staff was measured. Studies have revealed that some people, such as players, cashiers, sales assistants, caterers, and office staff, may have elevated levels of nickel on their fingers that surpass 0.035 grams per cm^{-2}. This can cause allergic reactions in 22% of those who are allergic to nickel.[20] For studies of skin exposure to nickel under standardized experimental conditions in the workplace and in the general setting, the acid wipe sampling technique is suitable.[19]

The EU is recommending for the testing of nickel from coins to use either an inductively-coupled plasma optical emission spectrometer (ICP-OES), or ICP mass spectrometer (ICP-MS), or an electrothermal excitation atomic absorption spectrometer (GFAAS). Regarding the importance of the uptake of the nickel ions from the surface of the coins, we investigated nickel compounds and complexes that form in contact of 1-Euro coins with sweat by using the molecularly-sensitive laser desorption ionization mass spectrometry (LDI-MS).

Results and Discussion

For our study, we used three circulating 1-Euro coins from Spain, Germany, and France that were cleaned and treated with artificial sweat. These coins were chosen for initial experiments to evaluate if AP-LDI MS (atmospheric pressure laser desorption/ionization mass spectrometry) is suitable for detecting molecular and elemental components from the coin surfaces shown in Figure 2.

Positively singly-charged nickel, copper, and zinc ions were detected, as shown in Figure S1. MS imaging of the 3D surface of a 1-Euro coin showed that Zn was most abundant in the outer ring, Cu was present in both inner and outer rings, and Ni was found primarily in the inner ring and that several metal-organic compounds were readily detectable from the surface. An exemplary AP-LDI MS imaging result of a cleaned 1-Euro coin is shown in Figure 4. The signals at *m/z* 207.8941 ($[C_4HO_3NNi+K]^+$), and *m/z* 116.9527 ($[CH_4NZn+Na]^+$) are shown in red, and green, respectively. The signals were assigned based on their accurate masses and isotopologue patterns using the XCalibur software (Figures S9).

Pixel coverages, computed for three 1-Euro coins as percentage of pixels with signal intensities of selected ions above a preset threshold value, are shown in Figure 5. As expected and consistent with reported coin compositions, Cu$^+$ ions had the highest pixel coverage, followed by zinc and nickel in the three coins.

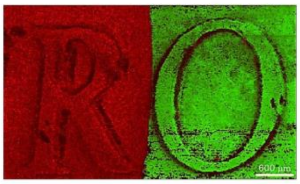

Figure 4. 3D-surface red-green overlay MS image of *m/z* 207.8941 (red, $[C_4HO_3NNi+K]^+$), and *m/z* 116.9527 (green, $[CH_4NZn+Na]^+$). MS images of the two signals were generated from a cleaned 1-Euro coin (2002, Germany) with 320×189 pixels; 15 μm pixel size; *m/z* bin width: $\Delta(m/z)/(m/z) = \pm 5$ ppm.

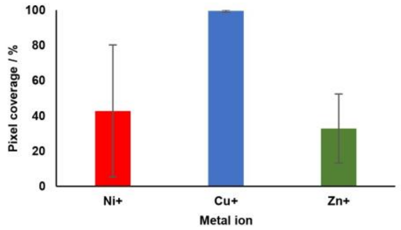

Figure 5. Average pixel coverages of Ni$^+$, Cu$^+$ and Zn$^+$ ions in scanned area (see Figure 4) of three 1-Euro coins from Spain, Germany and France.

A comparison of the three coins revealed that the pixel coverage of Ni$^+$ in the 1-Euro coin from France (1999) was higher than in the 1-Euro coins from Spain (2007) and Germany (2002) (Figure 6). We believe that the higher Ni$^+$ pixel coverage on the 1-Euro coin from France is due to the fact that the French coin was produced in 1999 and the nickel directive

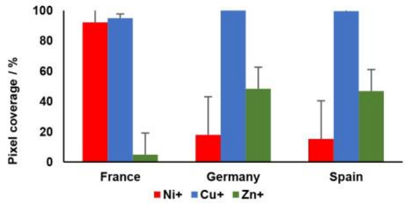

Figure 6. Pixel coverage percent of Ni$^+$, Cu$^{+,}$ and Zn$^+$ ions in scanned area of 1 Euro coin France 1999, Germany 2002 and Spain 2007.

Journal of Inorganic and General Chemistry
ZAAC
Zeitschrift für anorganische und allgemeine Chemie

guidelines, which were adopted in 1994, took effect in 2000 and have been implemented since 2001.

Even if pixel coverage is not a quantitative measure for bulk concentration, these results demonstrate that AP-LDI MS is capable to spatially probe metal appearances in coins and that these results are in line with reported region- and time-specific production processes.

Besides metal ions, metal-organic ions from the coin surface were investigated. Examples besides those of Figure 4 are *m/z* 178.8832, assigned to $[CH_4NCu_2+Na]^+$ and *m/z* 258.8152 assigned to $[CH_5ONCu_3+Na]^+$, shown in Figure 7. The signals were assigned based on their accurate masses and isotopologue patterns using the XCalibur software (for isotopologue patterns, MS images and tandem mass spectrum see Figures S2, S3, S4, S5).

In addition, transition metal complexes formed during skin contact with Euro coins were studied. Since sweat can play an important role in enhancing metal allergies, corrosion products produced by sweat on the surface of a 1-Euro coin were studied. In this study, three standard solutions, including urea (0.1 %), lactic acid (0.1 %), and artificial sweat solution (ASS), were sprayed homogeneously onto the surface of a cleaned 1-Euro coin. The color of one of the coins after spraying the urea solution changed to green in some parts after a day, as shown in Figure 8a, visibly indicating that metal ions had reacted with the urea solution. AP-LDI MSI experiments probed the corrosion products on the surface and detected a signal at *m/z* 140.9720, assigned as $[CuCH_4N_2O+H_2O]^+$ (MS image before and after spraying ASS, see Figure 9; experimental and theoretical isotopologue patterns of $CuCH_4N_2O+H_2O]^+$, see Figure S8). Although the lactic acid solution did not cause any apparent change in the coin surface (Figure 8b), an unknown new signal at *m/z* 158.0821 was detected.

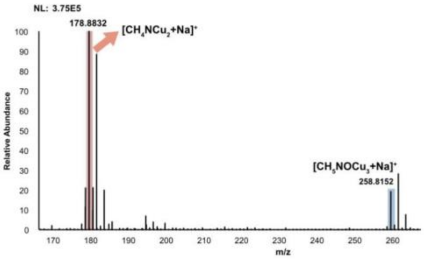

Figure 7. Positive-ion mode AP-LDI mass spectrum of *m/z* 178.8832 that was assigned to $[CH_4NCu_2+Na]^+$ and *m/z* 258.8152 assigned to $[CH_5ONCu_3+Na]^+$. Spectra were generated from a cleaned 1-Euro coin (2002, Germany) by averaging from 320×189 pixels; 15 µm pixel size. For isotopologue patterns see Figure S2.

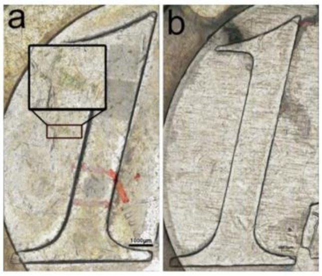

Figure 8. On a 1 Euro coin. a) urea 0.1 % solution, b) lactic acid 0.1 % solution after one day. The colour change is shown in a black rectangle, and the red marker shows the MALDI Mass Spectrometry analysis region.

To confirm the identity of $[Cu(CH_4N_2O)+H_2O])^+$, formed on the surface of 1-Euro coins after spraying ASS, we compared tandem mass spectra from the surface (Figure S6) with those from the desired metal complex generated from a standard solution of 1 mol/L copper(II) chloride dihydrate ($CuCl_2 \cdot 2\ H_2O$) and 0.1 % (m/m) urea (Figure S7). α-cyano-4-hydroxycinnamic acid (CHCA, purity 97 %, Sigma-Aldrich, USA) was used as a matrix for tandem mass spectra of the standard. Due to the low signal intensity of the complex measured by AP-LDI from the surface, the isotopologue patterns from tandem measurements from the coin surface and from the standard are only partly identical, but still confirm the identity of the compound.

Compared to cleaned Euro coins, the relative abundance of Ni^+ and Cu^+ ions increased on the surface of coins sprayed with solutions of urea (1 g/L) and lactic acid (1 g/L). Comparing the relative abundances of metal ions on the surface showed that after three days, the lactic acid solution produced a higher concentration of Ni^+ and Cu^+ ions compared to the urea solution, while after six days, the urea solution yielded a higher concentration of Ni^+ and Cu^+ ions compared to the lactic acid solution. The results provide an explanation for how lactic acid and urea impact the production of metal ions (by either oxidation of metals or by release from already oxidated metal compounds such as metal oxides or metal sulfides), particularly Cu^+ ions. As nickel allergy follows contact with the allergen, it can take 24 to 72 hours before symptoms manifest. These data suggest that acidic sweat can increase Ni^+ content in the first

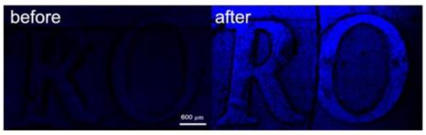

Figure 9. AP-LDI MS image of *m/z* 140.9728 (blue, $[Cu(CH_4N_2O)+H_2O])^+$) before and after spraying with ASS. MS images were generated with 325×193 pixels; 15 µm pixel size; *m/z* bin width: $\Delta(m/z)/(m/z) = \pm 5$ ppm.

Journal of Inorganic and General Chemistry
ZAAC
Zeitschrift für anorganische und allgemeine Chemie
RESEARCH ARTICLE

three days, resulting in an aggravated allergy, shown in Figure 10. A comparison of the pixel coverages of the three metal ions on the scanned area before and after spraying ASS, is shown in Figure 11.

Comparison of 3D-surface RGB MS images of the scanned area before and after spraying ASS also indicate the increase of pixel coverage of Ni^+ ions (Figure 12).

As shown by AP-LDI mass spectrometry, sweat increases the production of metal ions, especially nickel metal ions, which may play an important role in nickel allergy development. The increase of nickel metal ion abundances after one week is more influenced by urea, one of the main components of sweat, than by lactic acid.

Conclusions

A metal object interacting with sweaty skin will cause sensitive skin to become itchy and prickly within 15 to 20 minutes. Wearing these metallic items for several hours without a problem is common if people don't sweat.[21] So far, there is no clear understanding of how metals induce allergic reactions.

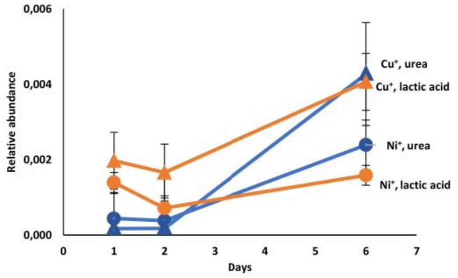

Figure 10. Relative abundance changes of Ni^+ and Cu^+ ions detected after spraying coin surfaces with urea and lactic acid 0.1 % solutions during 6 days; signals normalized to TIC.

Metal alloys such as nickel, copper, and zinc are known to easily form complexes with organic compounds found in skin secretions, such as triacylglycerols, amino acids, urea, and fatty acids. Identifying metal complexes formed on metallic surfaces of everyday products requires an analytical technique that offers a chemically specific, laterally resolved view of the allergy-causing processes. The summed mass spectrum of the scanned area of the 1-euro coin revealed different metal complexes with high intensities. The signal at *m/z* 178.8832 was assigned to $[CH_4NCu_2+Na]^+$ and the signal at *m/z* 258.8152 to $[CH_5ONCu_3+Na]^+$ (Figures S3, S4). Depending on material and usage time, coins lose their original color, appearance, and pits over time. Sweat is the main cause of these surface alterations, gradually damaging the coin's surface. We studied the effects of lactic acid and urea, which are the main components of sweat, on the surface of a 1-euro coin to identify corrosion products that might cause skin allergies. Compared to urea solution, lactic acid solution produced more metal ions in the first three days. Furthermore, a new metal complex at *m/z* 140.9728 $[Cu(CH_4N_2O)+H_2O)]^+$ was assigned in positive-ion mode. Limitations of our approach are variations of limits of detection of different metal-organic substances. Physiologically relevant compounds might be present on the surface of coins which are not detectable by our method. However, the 3D-surface red-green overlay MS image of *m/z* 207.8941 (red, $[C_4HO_3NNi+K]^+$)

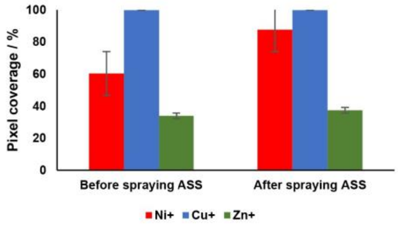

Figure 11. Pixel coverages of Ni^+, Cu^+ and Zn^+ ions in scanned area before and after spraying ASS for 6 days.

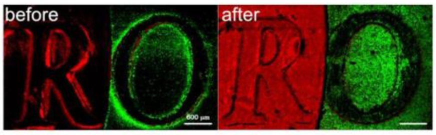

Figure 12. 3D-surface RGB MS images of *m/z* 57.93480 (red, $[Ni]^+$) and *m/z* 63.92860 (green, $[Zn]^+$), a) before and b) after spraying with ASS; *m/z* bin width: $\Delta(m/z)/(m/z) = \pm 5$ ppm

and *m/z* 116.9527 (green, $[CH_4NZn+Na]^+$) in Figure 4 and the AP-LDI MS image of *m/z* 140.9728 (blue, $[Cu(CH_4N_2O)+H_2O])^+$) in Figure 9 shows that relevant Zn-, Cu- and Ni-containing compounds were detected with high signal intensities on the coin's surface. The method is able to investigate a large variety of other metal complex classes, provided that the signal intensity is high enough for tandem mass spectrometry. Still, we cannot completely exclude that some further compounds form that we did not detect.

Our findings do not allow us to solve the health issues caused by nickel allergy; however, having identified how the metals are dissolved from the coin surface, we will now start to investigate how the metal ions are penetrating the skin when causing the allergic reaction.

Experimental Section

Coins

For this study, coins were selected from the wide-ranging circulation.

Solutions and reagents

Sodium chloride (Sigma-Aldrich, Steinheim, Germany); lactic acid (Sigma-Aldrich); urea (Fluka™, urea ≥99.5%, Fisher scientific, Schwerte, Germany); 1 mol/L and 0,1 mol/L aqueous sodium hydroxide solution (Sigma-Aldrich). α-cyano-4-hydroxycinnamic acid (CHCA, purity 97%, Sigma-Aldrich) was used as a matrix in MALDI experiments. Matrix solution was prepared in a concentration of 10 g/L in acetonitrile/water 7:3 v:v with addition of 0.1 vol% trifluoroacetic acid (TFA, uvasol for spectroscopy, Merck, Darmstadt, Germany; acetonitrile uvasol, Merck; water HiPerSolv Chromanorm for HPLC, filtered at 0.2 μm, VWR, Darmstadt, Germany). Copper(II) chloride dihydrate ($CuCl_2 \cdot 2\ H_2O$) was purchased from Sigma-Aldrich.

Solutions for MS and MSI analysis

Lactic acid solution and urea solution were prepared in a concentration of 0.1% m/m in deionized water. An artificial sweat solution containing sodium chloride (0.5% m/m), lactic acid (0.1% m/m), and urea (0.1% m/m), dissolved in deionized water was prepared. The pH was adjusted to 6.5 by adding sodium hydroxide solution, following EN 1811, the reference method for testing in compliance with the EU Nickel Directive.

$[Cu(urea)]^+$ standard solution for MALDI MS measurements was prepared by mixing 1 mol/L copper(II) chloride dihydrate ($CuCl_2 \cdot 2\ H_2O$) and 0,1% (m/m) urea in 1:1 CH_3OH/H_2O. The solution were premixed in a ratio of 1:1 (v:v:) with CHCA matrix solution.

Sample preparation

Volumes of 200-μl of the lactic acid solution, the urea solution and the artificial sweat solution were sprayed onto pre-washed 1-Euro coins with a flow rate of 10 μl/min, an N_2 pressure of 1 bar and a rotation of 500 rpm using an ultrafine pneumatic sprayer system (SMALDIPrep, TransMIT GmbH, Giessen, Germany). The three coins were kept at a temperature of 37±2 °C for a week at normal laboratory atmosphere. An optical image of the coins was recorded with a Keyence VHX-5000 digital microscope (Keyence Deutschland GmbH, Neu-Isenburg, Germany) equipped with a VH–Z250R objective lens. Finally, the coins were inserted into the ion source of the mass spectrometer for 3D-surface AP-LDI MSI measurements.

Sample preparation of standards

One microliter of standard solution was deposited on a microscopy glass slide used as an MS target. After evaporation of the solvent, a 3D optical image of the sample was recorded by means of the digital microscope. Finally, the glass slide was inserted into the ion source of the mass spectrometer.

Instrumentation

Imaging experiments were performed on a Q Exactive HF orbital trapping mass spectrometer (Thermo Fisher Scientific, Bremen, Germany) equipped with an autofocusing AP-SMALDI^5 AF ion source (TransMIT GmbH). Fifty UV-laser pulses per pixel at a frequency of 100 Hz were used to desorb and ionize sample atoms and/or molecules. Step sizes between 15 and 25 μm were chosen for imaging experiments according to the sample size (region of interest, ROI). The ion injection time was set to 500 ms, the s-lens level was set to 100 arbitrary units, and the capillary temperature was set to 250 °C. An acceleration voltage of 3.0 kV was used in the ion source. All measurements were performed in positive-ion mode with a mass resolution of 240,000 at *m/z* 200. The mass spectrometer was calibrated with known matrix signals prior to LDI or MALDI measurements, resulting in a mass accuracy of better than 2 ppm root mean square error (RMSE).

3D-surface AP-LDI imaging measurements

Autofocusing AP-LDI MSI experiments were performed using 25 μm step size with 177x120 pixels for 1-euro coin (2007, Spain), 25 μm step size with 320x189 pixels for 1-euro coin (2002, Germany) and 15 μm step size with 198x122 pixels for 1-euro coin (1999, France). The mass spectrometer was calibrated with known Cu^+ signals at *m/z* 62.92905 in RecalOffline software. Processing, evaluation and MS image generation were performed in Mirion software.

Data evaluation and image generation

Q Exactive Tune (version 2.4, Thermo Fisher Scientific, Bremen, Germany) was used for data acquisition. The SMALDIControl software (V1.1-118, TransMIT GmbH) was used for image acquisition and for system control and autofocusing 3D-surface operation.[22]

Mirion software package (v3.2.64.29) (TransMIT GmbH) was used for data evaluation and image generation. The absolute mass variance of spectra was set to 0.005 u.[23] The bin width was adjusted to 0.005 u. No TIC normalization was applied in the image creation process.

XCalibur (version 4.0.27.13, Thermo Fisher Scientific) was utilized to display mass spectra. Ion images of selected *m/z* values were generated using MIRION imaging software with a mass bin width of *m/z* ±5 ppm from the accurate mass. MS images were normalized to the highest intensity measured for each ion separately. No further image processing steps such as smoothing or TIC normalization were used. Red-green-blue (RGB) overlay images were obtained by selecting and overlaying *m/z* bins for the three channels.

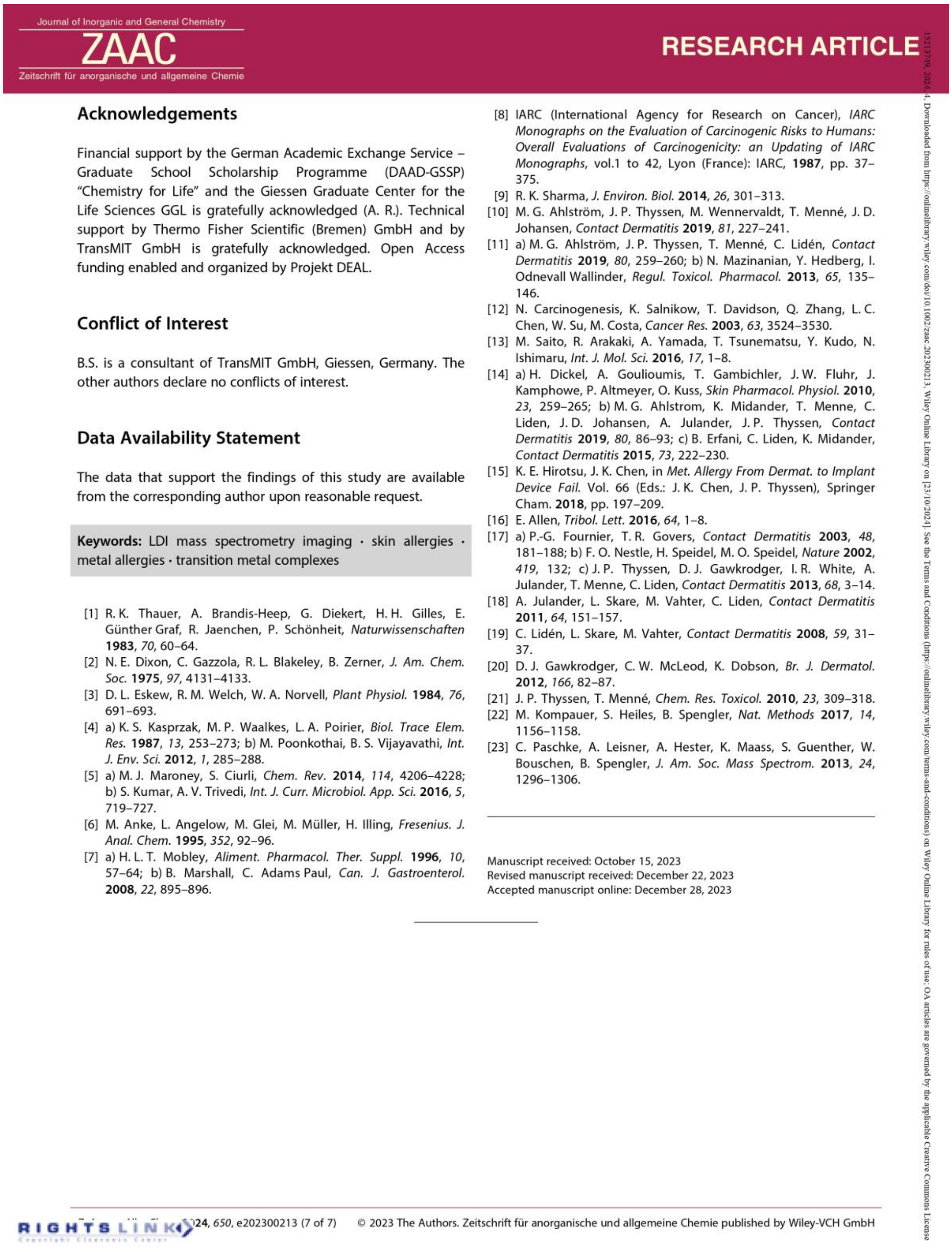

Journal of Inorganic and General Chemistry
ZAAC
Zeitschrift für anorganische und allgemeine Chemie

RESEARCH ARTICLE

Acknowledgements

Financial support by the German Academic Exchange Service – Graduate School Scholarship Programme (DAAD-GSSP) "Chemistry for Life" and the Giessen Graduate Center for the Life Sciences GGL is gratefully acknowledged (A. R.). Technical support by Thermo Fisher Scientific (Bremen) GmbH and by TransMIT GmbH is gratefully acknowledged. Open Access funding enabled and organized by Projekt DEAL.

Conflict of Interest

B.S. is a consultant of TransMIT GmbH, Giessen, Germany. The other authors declare no conflicts of interest.

Data Availability Statement

The data that support the findings of this study are available from the corresponding author upon reasonable request.

Keywords: LDI mass spectrometry imaging · skin allergies · metal allergies · transition metal complexes

[1] R. K. Thauer, A. Brandis-Heep, G. Diekert, H. H. Gilles, E. Günther Graf, R. Jaenchen, P. Schönheit, *Naturwissenschaften* **1983**, *70*, 60–64.

[2] N. E. Dixon, C. Gazzola, R. L. Blakeley, B. Zerner, *J. Am. Chem. Soc.* **1975**, *97*, 4131–4133.

[3] D. L. Eskew, R. M. Welch, W. A. Norvell, *Plant Physiol.* **1984**, *76*, 691–693.

[4] a) K. S. Kasprzak, M. P. Waalkes, L. A. Poirier, *Biol. Trace Elem. Res.* **1987**, *13*, 253–273; b) M. Poonkothai, B. S. Vijayavathi, *Int. J. Env. Sci.* **2012**, *1*, 285–288.

[5] a) M. J. Maroney, S. Ciurli, *Chem. Rev.* **2014**, *114*, 4206–4228; b) S. Kumar, A. V. Trivedi, *Int. J. Curr. Microbiol. App. Sci.* **2016**, *5*, 719–727.

[6] M. Anke, L. Angelow, M. Glei, M. Müller, H. Illing, *Fresenius. J. Anal. Chem.* **1995**, *352*, 92–96.

[7] a) H. L. T. Mobley, *Aliment. Pharmacol. Ther. Suppl.* **1996**, *10*, 57–64; b) B. Marshall, C. Adams Paul, *Can. J. Gastroenterol.* **2008**, *22*, 895–896.

[8] IARC (International Agency for Research on Cancer), *IARC Monographs on the Evaluation of Carcinogenic Risks to Humans: Overall Evaluations of Carcinogenicity: an Updating of IARC Monographs*, vol.1 to 42, Lyon (France): IARC, **1987**, pp. 37–375.

[9] R. K. Sharma, *J. Environ. Biol.* **2014**, *26*, 301–313.

[10] M. G. Ahlström, J. P. Thyssen, M. Wennervaldt, T. Menné, J. D. Johansen, *Contact Dermatitis* **2019**, *81*, 227–241.

[11] a) M. G. Ahlström, J. P. Thyssen, T. Menné, C. Lidén, *Contact Dermatitis* **2019**, *80*, 259–260; b) N. Mazinanian, Y. Hedberg, I. Odnevall Wallinder, *Regul. Toxicol. Pharmacol.* **2013**, *65*, 135–146.

[12] N. Carcinogenesis, K. Salnikow, T. Davidson, Q. Zhang, L. C. Chen, W. Su, M. Costa, *Cancer Res.* **2003**, *63*, 3524–3530.

[13] M. Saito, R. Arakaki, A. Yamada, T. Tsunematsu, Y. Kudo, N. Ishimaru, *Int. J. Mol. Sci.* **2016**, *17*, 1–8.

[14] a) H. Dickel, A. Goulioumis, T. Gambichler, J. W. Fluhr, J. Kamphowe, P. Altmeyer, O. Kuss, *Skin Pharmacol. Physiol.* **2010**, *23*, 259–265; b) M. G. Ahlstrom, K. Midander, T. Menne, C. Liden, J. D. Johansen, A. Julander, J. P. Thyssen, *Contact Dermatitis* **2019**, *80*, 86–93; c) B. Erfani, C. Liden, K. Midander, *Contact Dermatitis* **2015**, *73*, 222–230.

[15] K. E. Hirotsu, J. K. Chen, in *Met. Allergy From Dermat. to Implant Device Fail.* Vol. 66 (Eds.: J. K. Chen, J. P. Thyssen), Springer Cham. **2018**, pp. 197–209.

[16] E. Allen, *Tribol. Lett.* **2016**, *64*, 1–8.

[17] a) P.-G. Fournier, T. R. Govers, *Contact Dermatitis* **2003**, *48*, 181–188; b) F. O. Nestle, H. Speidel, M. O. Speidel, *Nature* **2002**, *419*, 132; c) J. P. Thyssen, D. J. Gawkrodger, I. R. White, A. Julander, T. Menne, C. Liden, *Contact Dermatitis* **2013**, *68*, 3–14.

[18] A. Julander, L. Skare, M. Vahter, C. Liden, *Contact Dermatitis* **2011**, *64*, 151–157.

[19] C. Lidén, L. Skare, M. Vahter, *Contact Dermatitis* **2008**, *59*, 31–37.

[20] D. J. Gawkrodger, C. W. McLeod, K. Dobson, *Br. J. Dermatol.* **2012**, *166*, 82–87.

[21] J. P. Thyssen, T. Menné, *Chem. Res. Toxicol.* **2010**, *23*, 309–318.

[22] M. Kompauer, S. Heiles, B. Spengler, *Nat. Methods* **2017**, *14*, 1156–1158.

[23] C. Paschke, A. Leisner, A. Hester, K. Maass, S. Guenther, W. Bouschen, B. Spengler, *J. Am. Soc. Mass Spectrom.* **2013**, *24*, 1296–1306.

Manuscript received: October 15, 2023
Revised manuscript received: December 22, 2023
Accepted manuscript online: December 28, 2023

2. Supplementary Information

Mass spectrometric analysis of transition metal complexes formed through contact of artificial sweat with circulating Euro coins

Rezaei, A.; Heiles, S.; Spengler, B.; Schindler, S. Mass Spectrometric Analysis of Transition Metal Complexes Formed through Contact of Artificial Sweat with Circulating Euro Coins. *Zeitschrift für Anorg. und Allg. Chemie* **2024**, *650* (4), e202300213

https://onlinelibrary.wiley.com/action/downloadSupplement?doi=10.1002%2Fzaac.202300213&file=zaac202300213-sup-0001-misc_information.pd

Mass spectrometric analysis of transition metal complexes formed through contact of artificial sweat with circulating Euro coins

Azar Rezaei,[a] Sven Heiles,[b, c] Bernhard Spengler,*[a] and Siegfried Schindler*[a]

Supporting Information

[a] Prof. Dr. S. Schindler

Institute of Inorganic and Analytical Chemistry

Justus Liebig University Giessen, Giessen, Germany

Heinrich-Buff-Ring 17, 35392 Gießen (Germany)

Fax: (+49)641-993-4149

E-mail: siegfried.schindler@chemie.uni-giessen.de

Prof. Dr. B. Spengler

Institute of Inorganic and Analytical Chemistry

Justus Liebig University Giessen, Giessen, Germany

Heinrich-Buff-Ring 17, 35392 Gießen (Germany)

Fax: (+49) 641-99-34809

E-mail: bernhard.spengler@anorg.chemie.uni-giessen.de

[b] Jun.-Prof. Dr. Sven Heiles

Leibniz-Institut für Analytische Wissenschaften – ISAS – e.V.

44139 Dortmund, Germany

E-mail: sven.heiles@isas.de

[c] Jun.-Prof. Dr. Sven Heiles

Lipidomics, Faculty of Chemistry, University of Duisburg-Essen

45141 Essen, Germany

E-mail: sven.heiles@isas.de

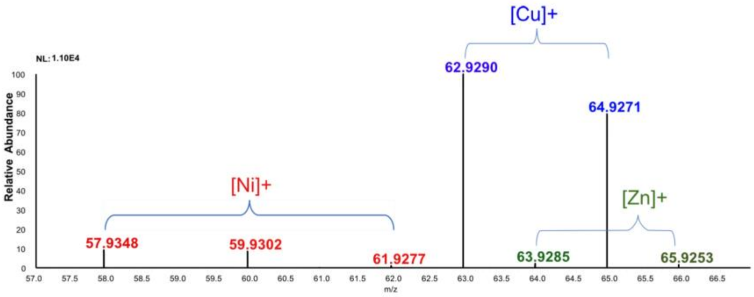

Figure S1. Positive-ion mode AP-LDI mass spectrum of m/z 57.9348 (Red, [Ni]$^+$), m/z 62.9290 (Blue, [Cu]$^+$), and m/z 63.9286 (Green, [Zn]$^+$) isotopes. Spectra were generated from a clean 1-Euro coin (2002, Germany) by averaging from 320 × 189 pixels; 15 µm pixel size. The Ni^{2+}, Cu^{2+}, and Zn^{2+} ions were non-detectable.

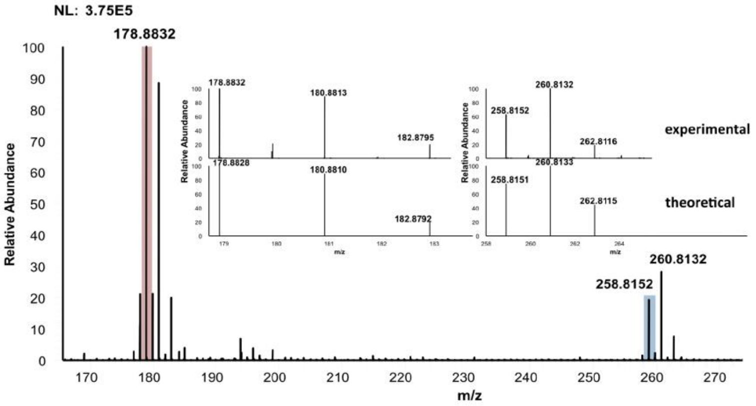

Figure S2. Positive-ion mode AP-LDI mass spectrum and experimental/theoretical isotopologue patterns of m/z 178.8832 that was assigned to [CH_4NCu_2+Na]$^+$ and m/z 258.8152 assigned to [CH_5ONCu_3+Na]$^+$. Spectra were generated from a cleaned 1-Euro coin (2002, Germany) by averaging from 320 × 189 pixels; 15 µm pixel size.

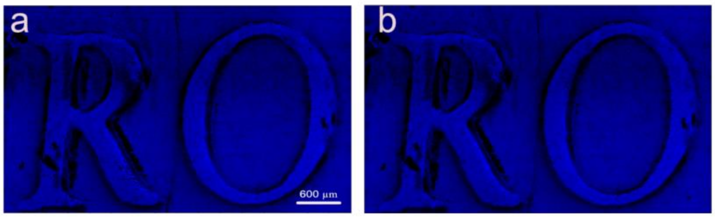

Figure S3 . AP-LDI MS image of a) m/z 178.8832 ($[CH_4NCu_2+Na]^+$) and b) m/z 180.8813 (second isotopologue of $[CH_4NCu_2+Na]^+$). MS images were generated from a cleaned 1-euro coin with 320 × 189 pixels; 15 µm pixel size; m/z bin width: Δ(m/z)/(m/z) = ±5 ppm.

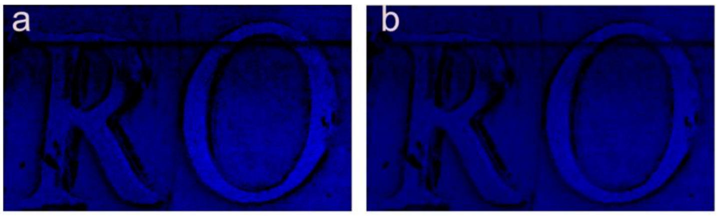

Figure S4. AP-LDI MS image of a) m/z 258.8152 ($[CH_5ONCu_3+Na]^+$) and b) m/z 260.8133 (second isotopologue of $[CH_5ONCu_3+Na]^+$). MS images were generated from a cleaned 1-euro coin with 320 × 189 pixels; 15 µm pixel size; m/z bin width: Δ(m/z)/(m/z) = ±5 ppm.

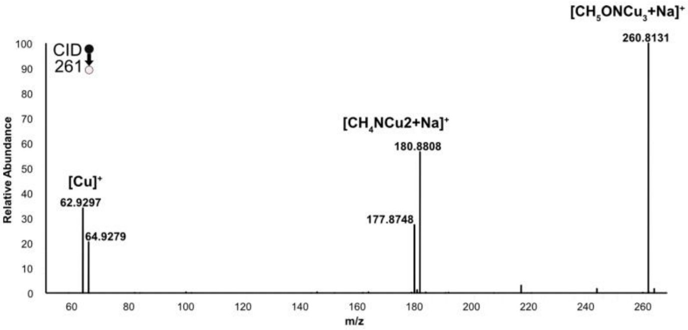

Figure S5. Positive-ion mode AP-LDI CID tandem mass spectrum of m/z 260.8133, assigned to the second isotopologue of $[CH_5ONCu_3+Na]^+$, confirming the presence of ^{65}Cu. Spectra were generated from a clean 1-Euro coin (2002, Germany) by averaging from 320 × 189 pixels; 15 µm pixel size.

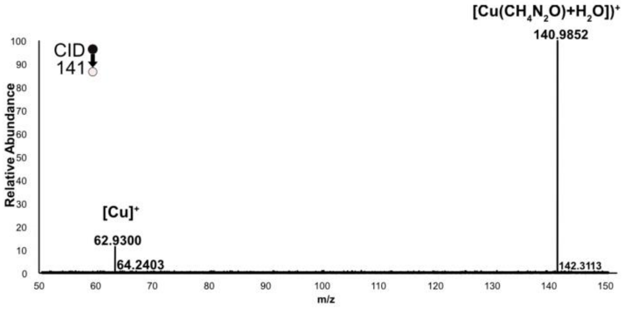

Figure S6. Positive-ion mode AP-LDI CID tandem mass spectrum of m/z 140.9852 that was assigned to [Cu(CH$_4$N$_2$O)+H$_2$O])$^+$, confirming the presence of Cu. Spectra were generated from a 1-euro coin after spraying ASS by averaging from 320 × 189 pixels, 15 µm pixel size.

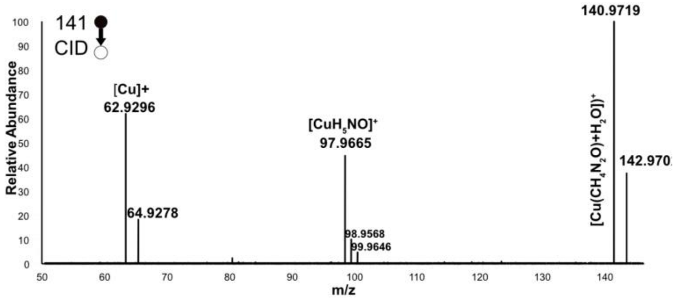

Figure S7. Positive-ion mode AP-MALDI CID tandem mass spectrum of m/z 140.9718, assigned to [Cu(CH$_4$N$_2$O)+H$_2$O])$^+$. Spectra were generated from standard solutions of 1 mol/L copper(II) chloride dihydrate (CuCl$_2$·2 H$_2$O),and 0,1 % (m/m) urea. α-cyano-4-hydroxycinnamic acid (CHCA) was used as a matrix.

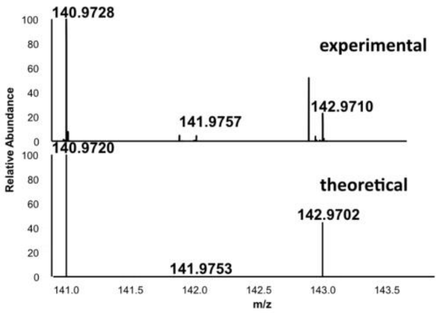

Figure S8. Experimental and theoretical isotopologue patterns of positive-ion-mode AP-LDI mass spectrum of m/z 140.9728, assigned to $[Cu(CH_4N_2O)+H_2O])^+$. Spectra were generated from a 1-euro coin after spraying ASS by averaging from 320 × 189 pixels, 15 µm pixel size.

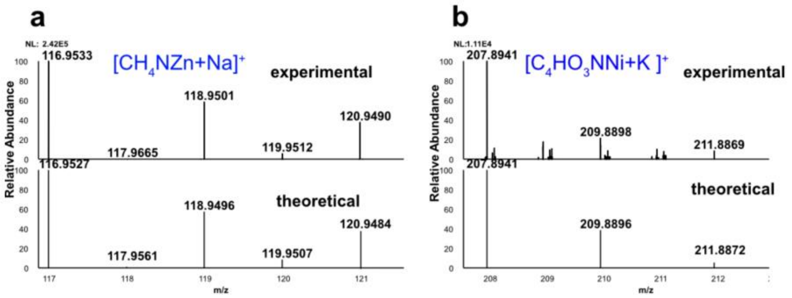

Figure S9. Positive-ion mode AP-LDI mass spectrum and experimental/theoretical isotopologue patterns of a) m/z 116.9533 that was assigned to $[CH_4NZn+Na]^+$ and b) m/z 207.8941 assigned to $[C_4HO_3NNi+K\ ]^+$. Spectra were generated from a clean 1-Euro coin (2002, Germany) by averaging from 320 × 189 pixels; 15 µm pixel size.

CHAPTER III

1. Metabolipidomic changes induced by dermal nickel penetration determined in an ex vivo porcine ear skin model

Rezaei, A.; Ganashalingam, Y.; Schindler, S.; Spengler, B.; Keck, C. M.; Schulz, S. Metabolipidomic Changes Induced by Dermal Nickel Penetration Determined in an Ex Vivo Porcine Ear Skin Model. *Rapid Commun. Mass Spectrom*. **2024**, 38 (20), e9891.

Received: 18 June 2024 | Revised: 30 July 2024 | Accepted: 31 July 2024
DOI: 10.1002/rcm.9891

Rapid Communications in Mass Spectrometry WILEY

RESEARCH ARTICLE

Metabolipidomic changes induced by dermal nickel penetration determined in an ex vivo porcine ear skin model

Azar Rezaei[1] | Yameera Ganashalingam[2] | Siegfried Schindler[1] | Bernhard Spengler[1] | Cornelia M. Keck[2] | Sabine Schulz[1]

[1]Institute of Inorganic and Analytical Chemistry, Justus Liebig University, Giessen, Germany

[2]Department of Pharmaceutics and Biopharmaceutics, Philipps University Marburg, Marburg, Germany

Correspondence
Sabine Schulz, Institute of Inorganic and Analytical Chemistry, Justus Liebig University, Giessen, Germany.
Email: sabine.schulz@anorg.chemie.uni-giessen.de

Funding information
German Academic Exchange Service-Graduate School Scholarship Programme (DAAD-GSSP), Grant/Award Number: 57450037; Giessen Graduate Center for the Life Sciences GGL

Rational: Nickel is one of humans' most prevalent triggers of allergic contact dermatitis. However, the underlying mechanisms of this allergy still need to be fully understood. One aspect that has yet to be explored is the direct impact of common metal allergens on the skin's metabolites and lipids composition.

Method: Our study employed matrix-assisted laser desorption/ionization mass spectrometry imaging (MALDI MSI) to analyze spatially resolved metabolic alterations induced by nickel exposure. Cross-sections of ex vivo porcine ear skin exposed to increasing nickel (II) ion concentrations (17–167 μg/cm^2) were measured with an AP-SMALDI^5 AF ion source coupled to Q Exactive HF Orbitrap mass spectrometer. Additionally, the penetration of nickel ions into the skin was observed through its pink complexation with dimethylglyoxime under light microscopy.

Results: For nickel ion concentrations up to 84 μg/cm^2, most nickel ions were stopped within the stratum corneum, while only a very small proportion of nickel ions penetrated the viable epidermis and dermis. Stratum corneum locations with high nickel ion concentrations showed a decrease in arginine and ceramides. Furthermore, several phosphatidylcholine and sphingomyelin species were found to be downregulated in the viable epidermis and dermis due to the nickel exposure.

Conclusion: Nickel penetrates at a trace level into the viable skin and induces severe metabolomic and lipidomic changes in the stratum corneum, epidermis, and dermis, indicating a change in the skin (barrier) function. These findings contribute to a deeper understanding of nickel-induced skin allergies and provide a solid foundation for further research.

1 | INTRODUCTION

Allergic contact dermatitis (ACD) is a multifaceted immune reaction triggered by exposure to small molecules in our surroundings. It causes an inflammatory skin condition triggered by exposure to certain organic chemicals and metal ions,[1,2] so-called haptens. This immune response engages the innate immune system and cellular stress responses, initiating crucial skin inflammation necessary for the initial sensitization and subsequent development of ACD. Upon contact, allergens bind to proteins, activating specific T cells that further exacerbate inflammation through their actions.[3] ACD is classified as a delayed-type hypersensitivity reaction (type 4) orchestrated by an individual's immune system in response to exposure to particular small molecules. Sensitization occurs initially when these substances interact with skin proteins, priming the skin for dermatitis upon subsequent encounters during the elicitation phase. ACD accounts for approximately 20% of contact dermatitis cases, with variations influenced by geographic location, personal practices, and permissible preservatives.[4] Various cell types, including T regulatory cells, play vital roles in regulating and resolving the inflammatory process. Effector cells such as CD4 + and CD8 + T cells, natural killer T cells (NKT), natural killer cells, B cells, and innate lymphoid cells contribute to the diverse clinical symptoms observed in ACD reactions.[5] Previous research has shed light on the cellular and molecular mechanisms of ACD, providing valuable insights into the role of different effector cells and the triggering role of haptens in initiating this immune response.[4] Lipids are critical in ACD, serving essential functions in skin structure and immune responses. Fatty acids contribute to the skin's integrity and function among these lipids. They are integral to forming triglycerides, which store energy and provide cell insulation.[6] In the context of ACD, lipids also participate in various signaling pathways and immune reactions.

Lipid mediators, such as prostaglandins and leukotrienes derived from arachidonic acid, play significant roles in inflammation and immune responses. These bioactive lipids act as signaling molecules by binding to specific receptors on target cells upon local synthesis. Notably, the protein CD36 acts as a sensor for long-chain fatty acids, influencing interorgan signaling and facilitating enhanced dietary fat digestion.[7] The skin is a primary defense mechanism against external threats, including pathogens, chemicals, irritants, and allergens, preventing ACD. However, if these substances penetrate the deeper layers of the skin, they may trigger an immune response, highlighting the crucial role of the skin's barrier function.[8] Disruptions in the stratum corneum, the outermost layer of the epidermis, can lead to atopic dermatitis (AD) by compromising the skin barrier function. Restoring the skin barrier function becomes pivotal in preventing or halting the progression of AD, given that the root cause is believed to lie within the skin barrier itself.[9] Skin barrier dysfunction significantly contributes to ACD by enhancing skin permeability, facilitating the rapid penetration of allergens, and triggering immune responses. AD, closely associated with ACD, exhibits skin barrier defects, including changes in lipid composition and reduced ceramide levels, resulting in compromised barrier function.[10] The lipid bilayer in the stratum corneum, comprising hydrophobic lipids such as ceramides, cholesterol, and free fatty acids, plays a crucial role in maintaining skin hydration and integrity.[10] Alterations in lipid composition, such as shorter chain lengths of fatty acids and ceramides observed in AD skin, further exacerbate skin permeability and contribute to barrier dysfunction.[10] Metals are common culprits for contact allergies, with nickel, cobalt, and chromium traditionally being the most significant offenders. Recently, attention has also been directed towards gold and palladium due to their increasing prevalence of contact allergies.[11]

The prevalence of metal hypersensitivity is strikingly high, affecting approximately 10–15% of individuals, with a higher incidence observed in women (around 10–20% versus 1–3% in men).[12,13] Nickel is the most frequently encountered contact allergen in various studies and clinical observations.[14] Hence, caution should be exercised to avoid potential health risks associated with metal exposure. Several factors influence the ability of a substance to penetrate the skin, including the quantity applied, the exposed area, duration of contact, location on the body, skin thickness and condition, sweating, temperature, humidity, physical activity, gender, race, age, and substance properties.[12] Metal allergies, particularly in the context of ACD,[15] cause skin lipid content changes. By examining the lipid profiles of ex vivo human skin, it was found that nickel, cobalt, and chromium significantly alter the levels of monoacylglycerides (MAG) and diacylglycerides (DAG), resulting in a down-regulation of these lipids upon nickel application in the stratum layers.[16]

Many skin diseases, such as psoriasis, AD, and ichthyoses, are linked to changes in the composition and metabolism of epidermal sphingolipids.[17] Changes in the levels of these sphingolipids in the skin have been associated with various skin disorders, such as inflammatory and allergic reactions. Studies of the lipid composition of diseased skin have indicated a decreased level of ceramide in the stratum corneum and altered ceramide profiles in such conditions.[18] Additionally, it has been reported that AD is associated with lipid composition changes and epidermal organization, suggesting a role for lipids like phosphatidylcholine (PC) in allergic skin conditions.[19] Further research into how metal allergies specifically alter these lipid contents and their interplay with the immune system holds immense potential for unlocking new strategies to manage and prevent conditions like ACD. Another substance important for skin health is arginine, a major component of filaggrin-derived natural moisturizing factors found predominantly in the middle layer of the stratum corneum. It contributes significantly to skin hydration.[20]

Recent technological advancements enabled researchers to track metal movement through skin tissue. Inductively coupled plasma mass spectrometry (ICP MS) allowed researchers to measure nickel permeation through skin depending on different nickel counter ions (sulfate, chloride, nitrate, and acetate) applied as an aqueous salt solution. The study used carefully controlled experimental conditions and ICP MS analysis to measure the steady-state flux of nickel through human stratum corneum isolated through trypsinization.[21]

In another study, Malmberg et al used time-of-flight secondary ion mass spectrometry (ToF SIMS) to investigate the distribution and penetration of nickel in ex vivo human skin. The study found that the highest concentration of nickel ions was in the outer layer of the skin, the stratum corneum, and the upper epidermis. The exposure time was 24 hours. In the 3D constructs, a depth of 500 μm into full-thickness human skin and a depth of approximately 400 μm down into punch biopsies (diameter 8 mm) were observed.[22]

Furthermore, they used ToF SIMS to investigate the penetration of three metal salts, nickel, cobalt, and chromium (III) salts, in ex vivo human skin. The results showed that all three metal salts were mainly accumulated in the stratum corneum, with only trace amounts present in the epidermis.[23]

Researchers have used MALDI MSI to analyze the distribution of lipids in normal ex vivo human skin[24] and skin biopsies taken from patients with Fabry's disease. In Fabry's disease, an accumulation of glycosphingolipids was observed in the skin of affected patients, indicating the potential role of these substances in the disease's pathogenesis.[25] MALDI-MSI was also used to study the spatial distribution of a psoriasis drug (acetretin) in a 3D tissue-engineered psoriatic skin model, demonstrating the potential of this technique to provide insights into disease mechanisms and drug delivery.[26]

Although ToF SIMS offers high spatial resolution and elemental analysis, reliable identification of complex biomolecules such as lipids is hampered by instrumental mass resolving power and ionization-induced fragmentation of molecular ions. For biomolecules, MALDI MSI is the preferred choice in many dermatological applications, providing the unique capability to analyze biomolecules in their native state without complex labeling. Recent advancements in atmospheric-pressure scanning microprobe matrix-assisted laser desorption/ionization (AP-SMALDI) resulted in a substantial improvement of sensitivity and lateral resolution (down to 1.4 µm laser spot diameter) of the method for visualizing the distribution of various biomolecules within tissues.[27] Moreover, coupling with an orbital trapping mass spectrometer featuring high mass resolution and accuracy allows for reliable biomolecule assignment on the sum formula level, making it ideal for high throughput metabolite profiling.[28] Despite its efficiency in lipidomic and skin disease research, MALDI MSI has not yet been applied to investigate nickel allergy mechanisms. Our study utilized MALDI MSI to detect metabolomic changes after nickel exposure in ex vivo porcine skin sections. Reliable biomolecule identification was achieved by additional analysis of the adjacent tissue sections by liquid chromatography–tandem mass spectrometry (LC-MS/MS). Furthermore, the study used dimethylglyoxime (H_2DMG) to visualize by light microscopy the nickel ion distribution in the skin, revealing insights into its penetration behavior.

2 | METHODS

2.1 | Chemicals

LC–MS grade acetonitrile (ACN) and water (H_2O) were purchased from VWR International, Fontenay-sous-Bois, France. Methanol, ethanol, and trifluoroacetic acid were obtained from Merck, Darmstadt, Germany, isopropanol (IPA) from Chemsolute, Renningen, Germany, and formic acid (FA) from Honeywell, Morris Plains, NJ, USA. Methyl-tert-butyl ether (MTBE), ammonium formate (AF), Mayer's hematoxylin solution, Eosin Y solution, xylene, Eukitt, Dimethylglyoxime (H_2DMG), α-Cyano-4-hydroxycinnamic acid (CHCA), Nickel (II) sulfate hexahydrate, and ammonium hydroxide (28% NH_3 in water) were obtained from Sigma-Aldrich, Steinheim, Germany. Synthetic lipid internal standards were procured from Avanti Polar Lipids (Alabaster, AL, USA) and phosphate-buffered saline (PBS) from Gibco, Carlsbad, CA, USA.

2.2 | Tissue sample preparation

Fresh pig ears (three biological replicates) were obtained from a local slaughterhouse and used within an hour after slaughter. First, the ears were cleansed with lukewarm water at approximately 23–25°C and softly dried using a paper towel with gentle dabbing, avoiding rubbing. Subsequently, examination areas measuring 2 × 2 cm (equivalent to an area of 4 cm^2) on the dorsal side of the ears were identified, ensuring that these skin regions were intact and devoid of any injuries.[29] The hair within these designated areas was meticulously trimmed to a length of approximately 1–3 mm using scissors. Then, Nickel (II) sulfate hexahydrate solutions in water with concentrations of $0\%_w$, $1\%_w$, $5\%_w$, and $10\%_w$ were administered to each examination area. The solutions were evenly distributed using a pipette without any massage. A 30 µL dose of the nickel solution was applied to each 4 cm^2 skin area. Control areas of skin treated with 30 µL water were also prepared. After an incubation period of 2 hours at 32°C, punch biopsies with a diameter of 15 mm were obtained from each examination area. Punch biopsies were preserved without further fixation by freezing at −80°C until further analysis.

2.3 | MALDI MSI sample preparation

Skin cross-sections of 10 µm thickness were created at −25°C using a Microm Sec35p® blade on a micro cryotome (Microm HM 525, Microm International GmbH, part of Thermo Fisher Scientific, Walldorf, Germany) and thaw-mounted onto microscopic glass slides. The quality of the sections was checked using a digital microscope (VHX-5000, Keyence, Japan). Prepared sections were kept at −80°C until analyzed with atmospheric-pressure scanning microprobe matrix-assisted laser desorption/ionization mass spectrometry imaging (AP-SMALDI MSI). For MS imaging analysis, the samples were thawed in a desiccator for 30 minutes. CHCA was used as a matrix at a 30 mg/mL concentration dissolved in ACN/H_2O/trifluoroacetic acid (69.95:29.95:0.1, v:v:v). The matrix was applied using an ultrafine pneumatic sprayer (SMALDIPrep, TransMIT GmbH, Giessen, Germany) as described elsewhere.[30] In brief, 100 µLl matrix solution was applied at a flow rate of 10 µLL/min and a nitrogen pressure of 1 bar.

2.4 | MALDI MSI measurements

Imaging experiments were conducted using a Q Exactive HF orbital trapping mass spectrometer (Thermo Fisher Scientific [Bremen] GmbH, Bremen, Germany) equipped with an autofocusing AP-$SMALDI^5$ AF ion source (TransMIT GmbH, Giessen, Germany). Desorption and ionization of sample molecules were achieved using 50 UV-laser pulses per pixel at a frequency of 100 Hz. A step size of 10 µm was selected for imaging experiments based on the sample size (region of interest, ROI). The ion injection time was set to 500 ms, the s-lens RF level was adjusted to 100 arbitrary units, and the capillary temperature was maintained at 250°C. An acceleration voltage of 3.0 kV was applied to the sample target. All measurements were conducted in positive-ion mode with a mass resolution of 240,000 at *m/z* 200 and a *m/z* range of 100–1,200 (two microinjections: *m/z* 100–400, *m/z* 400–1,200). Internal mass calibration of each recorded mass spectrum was performed with the lock mass *m/z* 249.9877 corresponding to the matrix ion $[CHCA+Na+K\text{-}H]^+$.

2.5 | Nickel staining with H_2DMG

After the MALDI MSI measurements were completed, one µL of $1\%_w$ H_2DMG solution in ethanol and ammonium hydroxide (9.9% [v/v]) was pipetted onto the skin cross-sections. Subsequently, the samples were placed in a desiccator for 15 minutes to complete the complexation reaction.[31] After this time, excess H_2DMG was removed by washing the stained tissue section with 500 µL ethanol. After drying, images of the stained skin cross-sections were taken with a digital microscope (VHX-5000, Keyence, Japan), magnification (250x). For the development and performance evaluation of the nickel staining method, skin-cross sections were thawed in a desiccator for 30 min and immediately stained following the procedure described above. Image processing to obtain grayscale images containing only the $Ni(HDMG)_2$ signal is described in the results section. To determine nickel ion penetration depths, an intensity threshold was applied to $Ni(HDMG)_2$ images to convert them into B&W images in ImageJ software.[32] Then, B&W images were saved as date files and imported into Excel. Subsequently, the number of white pixels representing $Ni(HDMG)_2$ was counted in 5,000 columns per image, and the mean and maximum number of white pixels per column were determined. After the conversion of pixel scale to micrometer scale, calculated numbers equal the mean and maximum penetration depths of nickel ions into the skin. Stratum corneum thickness was determined the same way from B&W image data files as nickel penetration depth, but in this case, B&W images of stratum corneum were generated by cropping the stratum corneum layer from the other tissue layers in the original light microscopic images.

2.6 | H&E staining

H&E staining was performed after nickel staining with H_2DMG to evaluate the histology of the skin cross-sections. The staining process involved rehydration using 100%, 70%, and 40% ethanol and deionized water for 2 minutes each. The samples were then kept in a hematoxylin solution for 12 minutes, followed by 10 minutes in tap water and 5 minutes in deionized water. After 1 minute in eosin Y solution, the samples were dehydrated using deionized water, 40%, 70%, 100% ethanol, and xylene for 2 minutes each. Finally, the samples were covered with Eukitt and a cover slip.

2.7 | LC–MS/MS sample preparation

For LC–MS/MS experiments, the lipid extraction method described elsewhere[33] was slightly modified. After cryo-sectioning, 70 mg of skin homogenate prepared from the remaining tissue was mixed with 100 µL of PBS buffer and 350 µL of methanol. The mixture was vortexed for 1 minute at 1500 rpm. Then, 1 mL of MTBE was added, and the mix was shaken for one hour at 20°C and 1,000 rpm. Then 300 µL H_2O was added to enhance phase separation, mixed for 1 minute at 1000 rpm, and centrifuged for 8 minutes at 13,000 rpm. The organic upper phase (1 mL) was collected and dried under nitrogen flow. The dried samples were stored at −80°C until analysis. Before analysis, the samples were reconstituted with 100 µL of ACN/IPA/H_2O (65:30:5, v:v:v). The extraction process used 100 µL of PBS as an extraction blank and the reconstitution buffer as the blank.

2.8 | LC–MS/MS analysis

The extracted lipids were separated on a UHPLC system (Ultimate 3,000 UHPLC, Thermo Fisher Scientific) equipped with a Kinetex C18 analytical column (Phenomenex, Torrance, CA, USA) (2.1 × 100 mm, 2.6 µm particle size, 100 Å pore size) and detected with an Orbitrap Exploris 480 mass spectrometer. Two mobile phases – phase A and phase B – were used. Phase A comprised a mixture of water and acetonitrile (40:60, v:v), while phase B was a mix of iso-propanol and acetonitrile (90:10, v:v). Both mobile phases contained 10mM ammonium formate and 0.1 vol-% formic acid. The experiment used a 28-minute multi-step gradient from 30% to 100% eluent B (Table S1) to separate the lipids. The flow rate was kept constant at 0.25 mL/min, and the injection volume was 10 µl. The column temperature was set to 50°C, while the autosampler temperature was set to 15°C. The lipidomic datasets were acquired using a data-dependent approach with the top-15 method (full MS/ddMS2, Top15) in positive-ion mode. The Orbitrap Exploris 480 was equipped with a heated electrospray ion source (HESI-II), and settings of data-dependent MS/MS acquisition and the HESI source can be found in Tables S2 and S3.

2.9 | Analysis of the mass spectrometric data

LC–MS/MS data were analyzed using LipidMatch Flow 3.1[34] and MS-DIAL. Individual MALDI MSI data sets were converted to imzML, stitched together, and uploaded to METASPACE. Metabolites and lipids were annotated with a mass tolerance of ± 3 ppm and a false discovery rate of 10% using the databases LIPIDMAPS (12.12.2017), swiss lipids (02.02.2018), HMDB-v4 and BraChem (01–2018). Annotation lists from METASPACE were manually compared with lipid lists obtained from MSDIAL and LipidMatch (LC–MS/MS data). Only those lipids detected by MALDI MSI, which were fully identified with fatty acid assignment by LC–MS/MS, were subjected to further semi-quantitative analysis in SCiLS Lab software (version 2016b, SCiLS GmbH, Bruker Daltonics). There, tissue areas of similar size were defined for each MALDI MSI measurement, and total ion count (TIC)-normalized mean intensities of all identified lipids and metabolites were extracted for those tissue areas. Samples were then divided into control and nickel-treated groups, and multiple t-tests were performed in GraphPad Prism on the semi-quantitative data obtained from the SCiLS Lab. Metabolites and lipids with a *p*-value of less than 0.05 were considered significantly different in the control and nickel-treated groups. The corresponding TIC-normalized MS images and RGB overlay images of three lipids were downloaded from METASPACE. Relative MALDI MSI intensities for the significantly different molecules were calculated by dividing each sample's mean TIC-normalized intensity by the mean TIC-normalized intensity of the control group. Then, average and standard deviation were calculated within the control and nickel-treated groups and displayed as bar charts with error bars.

3 | RESULTS AND DISCUSSION

Our study employed an ex vivo porcine ear skin model to comprehend the effects of nickel exposure on the skin. The well-known complexation reaction of nickel ions with dimethylglyoxime (H_2DMG) was used here to selectively stain nickel ions in skin cross-sections to track their penetration into the skin by light microscopy. MALDI MSI was used to study the metabolomic and lipidomic profile of control and nickel-treated skin topographically. LC–MS/MS was utilized in parallel to reliably identify lipid species detected by MALDI MSI in the different skin layers.

The workflow of the study is shown in Figure 1. Ex vivo fresh porcine ear skin was organized into 4 cm^2 skin areas, and each area was treated with 30 μl nickel sulfate hexahydrate aqueous solutions of varying concentrations ($1\%_w$, $5\%_w$, and $10\%_w$). Following a 2-hour open-air incubation in the oven at 32°C, punch biopsies measuring 15 mm in diameter were obtained and frozen at −80°C for future utilization. Frozen biopsies were sectioned at a thickness of 10 μm at −25°C. After cryo-sectioning, skin cross-sections were covered with matrix by ultrafine spraying of a solution of 30 mg/mL α-Cyano-4-hydroxycinnamic acid (CHCA) in ACN/H_2O/THF (70:30:0.1%, v:v:v). Metabolomic changes induced by nickel treatment were examined in positive-ion mode using an AP-SMALDI^5 AF ion source (TransMIT GmbH, Giessen, Germany) coupled to Q Exactive HF Orbitrap mass spectrometer (Thermo Fisher Scientific, Bremen, Germany). Subsequently, the measured tissue sections were stained with H_2DMG to visualize nickel ion penetration, followed by light microscopy analysis. Afterward, H&E staining was performed to assess tissue morphology by light microscopy. The remaining tissue from cryo-sectioning was ground, and lipids were extracted for LC–MS/MS analysis to identify the fatty acid composition of the lipid species annotated by the METASPACE online platform in the MALDI MSI data sets.

3.1 | Nickel ion penetration into pig ear skin

This study used nickel (II) sulfate hexahydrate in fresh pig ears as a model to simulate metal allergy responses in humans. Pig skin is very similar to human skin in its anatomy and thus is often used to study the effects of topically applied substances.[35] The microscopic anatomy of a pig ear cross-section and pig ear skin can be found in Figure S1. The skin layers most relevant for this study are the top, the stratum corneum, the viable epidermis (consisting of stratum granulosum, stratum spinosum, and stratum basale), and the dermis.

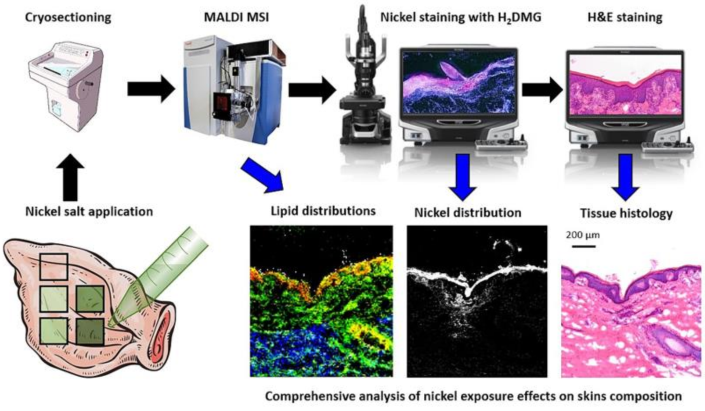

FIGURE 1 Experimental workflow illustrating the methodologies employed to investigate the effects of nickel exposure on skin. The study utilized ex vivo fresh porcine ear skin treated with nickel sulfate hexahydrate solutions of varying concentrations. After incubation, punch biopsies were taken, and tissues were processed for metabolomic and lipidomic analysis. MALDI MSI was used to examine metabolomic changes in skin cross-sections. Then, H_2DMG and H&E staining were employed to visualize nickel penetration and assess tissue morphology, respectively, by using a light microscope. LC-MS/MS was used for reliable lipid identification allowing lipid class and fatty acid assignment (not shown). [Color figure can be viewed at wileyonlinelibrary.com]

The method for visualizing nickel penetration into pig skin using light microscopy is based on the complexation of H_2DMG with Ni^{2+} ions, forming nickel dimethylglyoxime square planar complexes (Ni$(HDMG)_2$) of pink color and low solubility in water (Figure S2a).[31] The reaction was first described in 1905 by L. Tschugajew and is a standard analytical method in classical qualitative and quantitative analysis,[36] which is here applied for tissue staining. The semiquantitative performance of the H_2DMG staining method for tissue sections was evaluated for various nickel concentrations and biological replicates.

The workflow implemented to depict and measure the intensity of the pink color resulting from Ni$(HDMG)_2$ in the skin sections is outlined in Figure S2b. Initially, high-resolution images of samples treated with different nickel concentrations (0, 17, 84, and 167 μg/cm^2) and stained by H_2DMG were captured by a light microscope under standardized lighting and magnification (250x). All images were converted to the same format (JPEG), maintaining consistent dimensions to ensure accurate comparison. Next, ImageJ software was used to split the images into red, green, and blue channels. To eliminate background interference from the tissue, the green channel was subtracted from the red channel (containing the Ni$(HDMG)_2$ signal). Finally, the total area and mean intensity of the derived gray-scale images showing only Ni$(HDMG)_2$ signal were measured, and the sum intensity was calculated.

Figure 2A shows the sum intensity of the Ni$(HDMG)_2$ complex for one biological replicate but three technical replicates, depending on the topically applied nickel concentration. The corresponding gray-scale images showing the distribution of Ni$(HDMG)_2$ in the skin cross-sections (one technical replicate) are depicted in Figure 2B. The sum intensity of Ni$(HDMG)_2$ increased linearly with Ni^{2+} concentration, with the highest intensity observed in the sample treated with 167 μg/cm^2 Ni^{2+} ($R^2 = 0.9292$). For concentrations up to 84 μg/cm^2, the applied nickel ions were predominately accumulated in the stratum corneum and barely detected in the viable epidermis. Figure S3 shows an overlay of Ni$(HDMG)_2$ distribution and H&E staining of the same skin cross-section treated with 84 μg/cm^2 Ni^{2+}. In addition, the identity of the Ni$(HDMG)_2$ complex and its distribution in the skin cross-section was confirmed by positive-ion

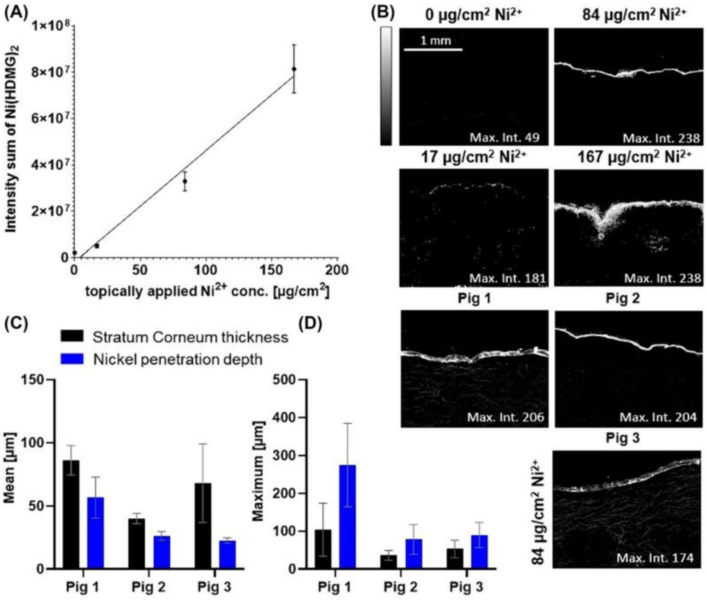

FIGURE 2 (A) Intensity sum of Ni$(HDMG)_2$ complex for control and samples treated with 17, 84, and 167 μg/cm^2 of Ni^{2+} (one biological, three technical replicates), (B) corresponding Ni$(HDMG)_2$ images of the samples (one technical replicate is shown), (C) mean stratum corneum thickness (black) and mean nickel penetration depth (blue) for three biological replicates treated with 84 μg/cm^2 nickel ions (three technical replicates per biological replicate), (D) maximum nickel penetration depth and corresponding stratum corneum thickness for three biological replicates treated with 84 μg/cm^2 nickel ions (three technical replicates per biological replicate) as well as corresponding Ni$(HDMG)_2$ images of the samples (one technical replicate is shown). Error bars represent standard deviation. [Color figure can be viewed at wileyonlinelibrary.com]

mode MALDI MSI. The $[Ni(HDMG)_2 + H]^+$ ion was observed readily at *m/z* 289.0440 with the expected isotopic pattern of a nickel ion. Microscopic and MALDI MS images revealed the same $Ni(HDMG)_2$ complex distribution in the stratum corneum (Figure S4). At 167 µg/cm² Ni^{2+} application, nickel ions penetrated deeper into the skin and were more often found in the viable epidermis and, to a small extent, in the dermis.

The nickel penetration depth was determined from the $Ni(HDMG)_2$ images of 84 µg/cm² Ni^{2+} treated skin samples (three technical replicates of three biological replicates) and compared to the stratum corneum thickness (Figure 2C,D). The $Ni(HDMG)_2$ distribution was strongly associated with the stratum corneum in all three biological replicates. Some penetration of nickel ions into the viable dermis was observed in one biological replicate. No $Ni(HDMG)_2$ signal was detected in the control skin cross-sections. The mean penetration depth of nickel ions was found to be lower than the mean thickness of the stratum corneum in each biological replicate ($n = 3$) (Figure 2C). However, there were severe differences in the mean stratum corneum thickness (86, 40, and 68 µm) and nickel penetration depths (57, 26, and 23 µm) for different biological replicates. The maximum penetration depth of nickel ions was found to be, on average, about 2.3 times larger than the stratum corneum thicknesses at these measurement points, showing that trace levels of nickel ions cross the skin barrier, reaching viable epidermis and even dermis (Figure 2D).

Overall, the data supports the method's effectiveness in detecting and quantifying nickel penetration. Compared to previous studies utilizing techniques such as TOF SIMS and ICP MS, the method developed in this study offers fast and cost-saving insights into nickel penetration mechanisms. Specifically, it provides valuable information on the localization of nickel within the skin's outermost layer.

3.2 | Nickel-induced metabolomic and lipidomic changes in pig ear skin

Metabolites and lipids play a major role in the function of skin. Alterations to the metabolomic and lipidomic composition of the skin have been associated with various skin diseases. Nickel-induced lipidomic changes in the stratum corneum and viable epidermis have focused so far on MAGs, DAGs, and ceramides. In our study, untargeted metabolomic and lipidomic analyses using MALDI MSI in the positive-ion mode were performed on an ex vivo porcine ear skin model with a spatial resolution of 10 µm. Cross-sections of pig ear skin from three biological replicates treated with 84 µg/cm² nickel sulfate (topically applied) alongside untreated control pig ear skin were analyzed to discern the impact of nickel ion exposure on skin metabolite composition. The ion signals of the combined MALDI MSI data set (3 control+3 nickel-treated samples) were annotated using METASPACE. In total, 536 ion signals were annotated using the databases LIPIDMAPS, swiss lipids, Human Metabolome Data Base (HMBD), and BraChem with a mass tolerance of ± 3 ppm, a false discovery rate of 10% and the following quasi-molecular ion: $[M + H]^+$, $[M + Na]^+$, $[M + K]^+$, $[M + NH_4]^+$. In addition, lipid extracts were prepared from the same tissues and analyzed with untargeted LC–MS/MS in positive-ion mode. A total of 1,012 lipids were identified by LipidMatchflow and 1,063 by MSDial. *m/z* values of the ions signal annotated in the MALDI MSI data set with METASPACE were manually compared with m/z values found in the LC–MS/MS data set by LipidMatchflow and MSDial. Ninety-three *m/z* values were found in both data sets and subjected to further analysis. After MALDI MSI, nickel ion distributions in the analyzed skin cross-section were determined by its reaction with H_2DMG, and tissue histology was obtained by subsequent H&E staining. Figure 3 shows the results from MALDI MSI (a), nickel staining with H_2DMG (b), and H&E staining (c) for control and an 84 µg/cm² nickel-treated sample. For MALDI MSI (Figure 3A), three MS images (with a mass tolerance of ±3 ppm, normalized to the total ion count (TIC)) were overlaid using the three native color channels (red, green, and blue) to illustrate the histology of the skin. Molecular markers for skin tissue layers were: *m/z* 522.4880, Cer-NS(d17:1/16:1), $[M + H]^+$ (red) for the stratum corneum; *m/z* 760.5851, PC(16:0/18:1), $[M + H]^+$ (blue) for dermis; and *m/z* 716.5225, PE(16:0/18:2), $[M + H]^+$ (green) for the viable epidermis. These markers were found to be not influenced by the nickel treatment and reproduced well the histology of the skin cross-section as determined by H&E staining (Figure 3C). On the other hand, staining of the skin cross-sections with H_2DMG (Figure 3B) revealed nickel ion distribution strongly associated with the stratum corneum in the nickel-treated skin cross-section. In contrast, the control skin cross-section only showed some background noise. Figure 3D shows the number of identified lipid species per lipid class: ceramides (CER, 22), diacylglycerols (DAG, 4), phosphatidylcholines (PC, 31), phosphatidylethanolamines (PE, 10), sphingomyelins (SM, 12) and lysophosphatidylcholines (LPC, 9). Several lipid classes were readily accessible with MALDI MSI in positive-ion mode, ranging from small molecules like cholesterol at *m/z* 369.3515 to complex lipids such as TG (16:0/16:0/18:1) at *m/z* 855.7412. High mass accuracy and mass resolution of the MALDI MSI data in combination with LC–MS/MS data allowed the reliable identification of individual lipid species, including the assignment of fatty acids. The results from MALDI MSI, nickel staining with H_2DMG, and H&E staining for all three biological replicates are shown in Figure S5.

The MALDI MSI data set described above was subjected to semi-quantitative analysis to identify which nickel ion treatment affects lipids and metabolites. The TIC-normalized mean intensities of all 93 identified lipids and two amino acids, arginine and histidine (identified by on-tissue MS/MS), were obtained from similar tissue areas (about 20.000–25.000 pixels) defined in SCILS Lab for the three control skin cross-sections and the three nickel-treated cross-sections. For each metabolite and lipid, a t-test was performed for the control versus nickel-treated group using the extracted TIC-normalized mean intensity values. A *p*-value smaller than 0.05 was considered significant. In total, 17 compounds were significantly downregulated in nickel-treated pig ear skin compared to control pig ear skin.

Changes in the lipid content were observed in all analyzed tissue layers (stratum corneum, viable epidermis, and dermis) and were not

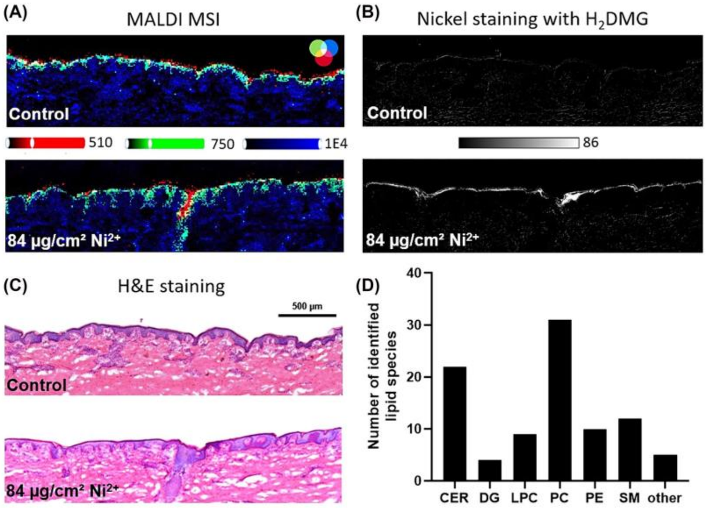

FIGURE 3 (A) RGB overlay images of three lipids measured by MALDI MSI with a step size of 10 µm in positive-ion mode from a control sample (290 × 99 pixels) and an 84 µg/cm^2 nickel-treated sample (298 × 92 pixels): *m/z* 522.4880, Cer-NS(d17:1/16:1), $[M + H]^+$ (red), marker for stratum corneum; *m/z* 760.5851, PC(16:0/18:1), $[M + H]^+$ (blue), marker for dermis; and *m/z* 716.5225, PE(16:0/18:2), $[M + H]^+$ (green), marker for the viable epidermis. The data was normalized to TIC. (B) Nickel distribution in a treated and a control sample was obtained by staining the samples with H_2DMG after MALDI MSI analysis. (C) H&E staining of a control sample and an 84 µg/cm^2 nickel-treated sample subjected previously to MALDI MSI and nickel staining with H_2DMG. d) Number of lipid species per lipid class detected by MALDI MSI and further validated by LC MS/MS in both nickel-treated and control groups. [Color figure can be viewed at wileyonlinelibrary.com]

limited to those areas directly penetrated by nickel ions, indicating that response mechanisms are not dependent on direct contact with the trigger. In Figure 4, PC (16:0/16:0) (A), SM(d17:1/19:0) (B), and arginine (C) were selected as molecular markers to depict the decrease of ion intensities within the dermis, viable epidermis, and stratum corneum, respectively, after nickel exposure. Bar charts in Figure 4D–F show the relative MALDI MSI intensities for all significantly down-regulated lipids and metabolites in relation to their main location (dermis, viable epidermis, and stratum corneum. The corresponding TIC-normalized ion images measured from three control and three nickel-treated samples can be found in Table S4. Notably, many of those lipids are structural lipids associated with the cell membranes belonging to sphingomyelin (SM) and phosphatidylcholine (PC) lipid classes. In addition, two PC species and four SM species feature odd-numbered fatty acids. The most abundant odd-numbered fatty acid features 17 carbons and one double bond. Fold-changes for downregulations ranged from 1.8 for arginine to 8.8 for SM(d17:1/22:0). Only arginine was found to be significantly downregulated in stratum corneum, but histidine and several ceramides showed a similar trend. Moreover, the observed downregulation of specific lipid species was dose-dependent. Figure S6 showed for one biological replicate decreasing signal intensities for arginine, histidine, SM(d18:1/20:0), and PC (16:0/18:0) with increasing nickel ion concentration (control, 42, 84, and 167 µg/cm^2). For the amino acids and ceramides, additionally, a localized effect in the stratum corneum was detected for one biological replicate with decreased molecular ion signals in areas with high nickel ion concentration (Figure S7). None of the 93 lipids semi-quantified in this study showed a significant up-regulation in the nickel-treated group.

Nickel ions, dissolved in water and deposited on the skin, first diffused into the stratum corneum. The middle of this layer is rich in arginine and serves as the first barrier for metal ions.[20] This barrier was also observed in our study for one biological replicate where the three stratum corneum layers were easily distinguished by microscopy, and most of the pink $Ni(HDMG)_2$ complex was found in the upper stratum corneum layer (Figure S8). Arginine is a natural moisturizing factor derived from filaggrin and is crucial to skin hydration. It was found in our study to be significantly downregulated in stratum corneum upon nickel treatment, which aligns with findings observed using chromium salts instead of nickel salts.[20] In addition, several ceramides showed a similar trend as arginine. Ceramides are considered as "mortar" (together with cholesterol and free fatty acids) between the corneocytes "bricks,"

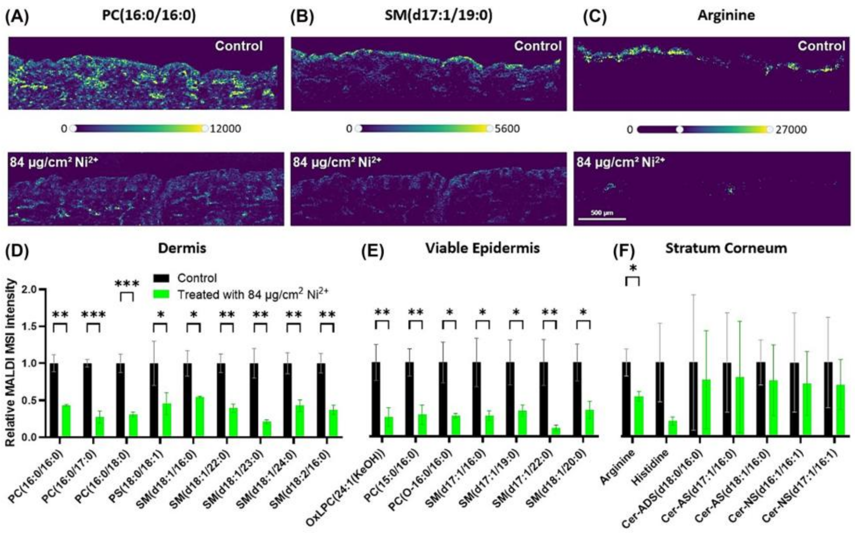

FIGURE 4 Metabolites and lipids downregulated by nickel exposure. (A–C) MALDI MSI images of downregulated molecular markers (A) for dermis: m/z 734.5694, (PC (16:0/16:0), $[M + H]^+$, (B) for viable epidermis: m/z 731.6062, SM(d17:1/19:0), $[M + H]^+$ and (C) stratum corneum: m/z 175.1190, arginine, $[M + H]^+$ (displayed m/z window: ±3 ppm). Depicted is a control skin sample with a size of 290 × 99 pixels and an 84 µg/cm^2 nickel-treated sample with a size of 298 × 92 pixels, acquired with a step size of 10 µm in positive-ion mode. (D) Relative MALDI MSI intensities of metabolites and lipids significantly downregulated by nickel treatment in (D) dermis, (E) viable epidermis, and (F) in stratum corneum. Relative MALDI MSI intensities were calculated by dividing mean intensities per sample by the average intensity of all control skin samples. Error bars show the standard deviation for three biological replicates. *p-value > 0.05, **p-value > 0.01 and ***p-value > 0.001. oxLPC(24:1(KeOH) refers to oxidized LPC, where KeOH represents a keto-hydroxy fatty acid. [Color figure can be viewed at wileyonlinelibrary.com]

which build together the water-permeability barrier of the skin. A decrease of arginine and ceramides upon nickel treatment thus suggests damage to the skin's barrier function. As demonstrated in this work, nickel ions penetrated in trace-level quantities into the viable epidermis and dermis, which is also in line with previous work. The lipid composition of the viable epidermis is dominated by phospholipids, especially phosphatidylcholines, and sphingomyelins. Phospholipids are membrane lipids. By their specific structure, they influence the fluidity and stiffness of the cell membranes and, therefore, their permeability. In addition, sphingomyelins form with cholesterol-specialized functional microdomains in the membrane, so-called "lipid rafts".[37] Besides that, sphingomyelins are considered a reservoir for bioactive lipids such as free fatty acids, ceramides, sphingosine, ceramide-1-phosphate, and sphingosine-1-phosphate.[37] Each of them has its own effect.[38] Metabolic pathways of ceramides, sphingomyelins, phosphatidylcholines, and their bioactive derivatives are highly interconnected. Changes in the concentration of any sphingolipid will result in changes in the concentration of other metabolites depending on the enzyme activity. Studies showed that any imbalance in ceramide/sphingomyelin concentrations is leveled out by keratinocytes in vitro in about three hours and that fatty acids can be transferred between SMs and PCs. Therefore, the observed downregulation of PCs and SMs in the viable epidermis might result from changes in the ceramide concentrations of the stratum corneum. On the other hand, bioactive products might be generated from PCs and SMs, which trigger further immune responses. The fatty acid composition of skin lipids is unique among mammalian tissues.[39] Skin is enriched in odd-chained and branched fatty acids. 9.4% of the total fatty acids in human skin lipids are odd-chain fatty acids (OCFA). In addition, a proportion of fatty acids are unusual long-chain (so-called very long-chain fatty acids (22–26 carbons, VLCFA) and ultra-long chain fatty acids (> 26 carbons, ULCFA)) and/or have a double bond in unusual places. Functionally, these fatty acids pose metabolic problems to pathogens and improve the survival of only compatible microorganisms. Further, VLCFA and ULCFA contribute to the rigidity and impermeability of membranes and, thus, to the skin's barrier function.[40] In our study, several phosphatidylcholines and sphingomyelins containing OCFAs and VLCFAs were found to be downregulated in viable epidermis and dermis. Possibly, they were degraded to bioactive lipids such as ceramides and free fatty acids to restore skin barrier function or trigger further immune responses.

4 | CONCLUSION

Based on the comprehensive investigation conducted in this study, several key findings have emerged regarding the impact of nickel exposure on skin tissue, explicitly focusing on nickel penetration mechanisms and alterations in lipid composition. We have gained valuable insights into the intricate relationship between nickel exposure and skin physiology using advanced analytical techniques such as MALDI MSI, nickel staining with H_2DMG, and meticulous sample preparation methods. The development and validation of the nickel staining method with H_2DMG represent a significant advancement in the field, offering a cost-effective and rapid means of visualizing nickel penetration within the skin's outermost layer, the stratum corneum. Using this method, we can accurately detect the penetration of nickel ions by forming a pink complex of nickel bis (dimethylglyoximate), even at low concentrations. This method provides crucial information for understanding the mechanisms behind nickel-induced allergic reactions. The H_2DMG staining intensity consistently observed across different nickel concentrations highlights the reliability and reproducibility of this approach, making it a valuable tool for assessing various nickel exposure scenarios. Furthermore, our investigation into the metabolite profile of skin tissue following nickel exposure has revealed notable alterations in essential lipid and amino acid species, particularly sphingolipids, phosphatidylcholines, histidine, and arginine, which play crucial roles in maintaining skin structure and function. The observed decreases in specific lipid species in the stratum corneum, epidermis, and dermis suggest a disruption in the skin's barrier function in response to nickel exposure. These findings provide important insights into the potential mechanisms by which nickel allergy manifests and highlight the intricate interplay between metal exposure, lipid metabolism, and immune response in the skin. Overall, the findings of this study contribute to a deeper understanding of nickel-induced skin allergies and provide a foundation for further research to develop targeted diagnostic and therapeutic strategies for individuals with nickel sensitivities. By elucidating the complex interactions between nickel ions and skin tissue at the molecular level, we can pave the way for more effective approaches to managing and preventing nickel-related dermatological conditions. Future investigations should continue to explore the mechanisms underlying nickel penetration and its effects on skin lipid composition, aiming to improve patient care and quality of life for those affected by nickel allergies.

AUTHOR CONTRIBUTIONS

Conceptualization, A.R., S.Schu., Y.G. C.M.K., S.Sch. and B.S; methodology, A.R. and Y.G; software, A.R. and S.Schu; validation, S. Schu., C.M.K., B.S. and S.Sch.; formal analysis, A.R., S.Schu.; investigation, A.R.; resources, C.M.K., S.Sch. and B.S.; data curation, A.R. and S.Schu; writing—original draft preparation, A.R.; writing—review and editing, S.Schu., C.M.K. and B.S.; visualization, A.R. and S. Schu; supervision, S. Schu, S.Sch. and B.S.; funding acquisition, B.S. All authors have read and agreed to the published version of the manuscript.

ACKNOWLEDGMENTS

Financial support by the German Academic Exchange Service-Graduate School Scholarship Programme (DAAD-GSSP) "Chemistry for Life" and the Giessen Graduate Center for the Life Sciences GGL is gratefully acknowledged (A. R.). Technical support by Thermo Fisher Scientific GmbH (Bremen, Germany) and by TransMIT GmbH (Giessen, Germany) is gratefully acknowledged. Open Access funding enabled and organized by Projekt DEAL.

CONFLICT OF INTEREST STATEMENT

B.S. and C.M.K. are consultants of TransMIT GmbH (Giessen, Germany). The other authors declare no conflicts of interest.

DATA AVAILABILITY STATEMENT

The data presented in this study are public available at METASPACE online platform: https://metaspace2020.eu/project/Ni_pig_skin_24.

ORCID

Siegfried Schindler https://orcid.org/0000-0002-9991-9513
Bernhard Spengler https://orcid.org/0000-0003-0179-5653
Cornelia M. Keck https://orcid.org/0000-0001-8888-2340
Sabine Schulz https://orcid.org/0000-0002-6561-5562

REFERENCES

1. Martin SF, Rühl-Muth A-C, Esser PR. Orchestration of inflammation in contact allergy by innate immune and cellular stress responses. *Allergo J Int*. 2024;33(2):41-48. doi:10.1007/s40629-023-00275-4
2. El Ali Z, Gerbeix C, Hemon P, et al. Allergic skin inflammation induced by chemical sensitizers is controlled by the transcription factor Nrf2. *Toxicol Sci*. 2013;134(1):39-48. doi:10.1093/toxsci/kft084
3. Salazar F, Ghaemmaghami AM. Allergen recognition by innate immune cells: critical role of dendritic and epithelial cells. *Front Immunol*. 2013;4:356. doi:10.3389/fimmu.2013.00356
4. Tan C-H, Rasool S, Johnston GA. Contact dermatitis: allergic and irritant. *Clin Dermatol*. 2014;32(1):116-124. doi:10.1016/j.clindermatol.2013.05.033
5. Rustemeyer T. Immunological mechanisms in allergic contact dermatitis. *Curr Treat Options Allergy*. 2022;9(2):67-75. doi:10.1007/s40521-022-00299-1
6. Panickar KS, Bhathena SJ. *Control of Fatty Acid Intake and the Role of Essential Fatty Acids in Cognitive Function and Neurological Disorders*. In: Montmayeur J-P, le Coutre J, eds.; 2010, doi:10.1201/9781420067767-c18.
7. Glatz JFC. Challenges in fatty acid and lipid physiology. *Front Physiol*. 2011;2:45. doi:10.3389/fphys.2011.00045
8. Elias PM, Schmuth M. Abnormal skin barrier in the etiopathogenesis of atopic dermatitis. *Curr Opin Allergy Clin Immunol*. 2009;9(5):437-446. doi:10.1097/ACI.0b013e32832e7d36
9. Simpson EL, Chalmers JR, Hanifin JM, et al. Emollient enhancement of the skin barrier from birth offers effective atopic dermatitis prevention. *J Allergy Clin Immunol*. 2014;134(4):818-823. doi:10.1016/j.jaci.2014.08.005

10. Agrawal R, Woodfolk JA. Skin barrier defects in atopic dermatitis. *Curr Allergy Asthma Rep*. 2014;14(5):433. doi:10.1007/s11882-014-0433-9
11. Thyssen JP, Menné T. Metal allergy—a review on exposures, penetration, genetics, prevalence, and clinical implications. *Chem Res Toxicol*. 2010;23(2):309-318. doi:10.1021/tx9002726
12. Saito M, Arakaki R, Yamada A, Tsunematsu T, Kudo Y, Ishimaru N. Molecular mechanisms of nickel allergy. *Int J Mol Sci*. 2016;17(2):202. doi:10.3390/ijms17020202
13. Magnano GC, Marussi G, Crosera M, et al. Probing the effectiveness of barrier creams against human skin penetration of nickel powder. *Int J Cosmet Sci*. 2024;46(1):39-50. doi:10.1111/ics.12893
14. Basketter D. Nickel: Intrinsic skin sensitization potency and relation to prevalence of contact allergy. *Dermat Contact, Atopic, Occup Drug*. 2021;32(2):71-77. doi:10.1097/DER.0000000000000666
15. Yamaguchi HL, Yamaguchi Y, Peeva E. Role of innate immunity in allergic contact dermatitis: an update. *Int J Mol Sci*. 2023;24(16):12975. doi:10.3390/ijms241612975
16. Knox S, Hagvall L, Malmberg P, O'Boyle NM. Topical application of metal allergens induces changes to lipid composition of human skin. *Front Toxicol*. 2022;4(August):867163. doi:10.3389/ftox.2022.867163
17. Borodzicz S, Rudnicka L, Mirowska-Guzel D, Cudnoch-Jedrzejewska A. The role of epidermal sphingolipids in dermatologic diseases. *Lipids Health Dis*. 2016;15(1):13. doi:10.1186/s12944-016-0178-7
18. Choi MJ, Maibach HI. Role of ceramides in barrier function of healthy and diseased skin. *Am J Clin Dermatol*. 2005;6(4):215-223. doi:10.2165/00128071-200506040-00002
19. Franco J, Rajwa B, Ferreira CR, Sundberg JP, HogenEsch H. Lipidomic profiling of the epidermis in a mouse model of dermatitis reveals sexual dimorphism and changes in lipid composition before the onset of clinical disease. *Metabolites*. 2020;10(7):299. doi:10.3390/metabo10070299
20. Kubo A, Ishizaki I, Kubo A, et al. The stratum corneum comprises three layers with distinct metal-ion barrier properties. *Sci Rep*. 2013;3(1):1731. doi:10.1038/srep01731
21. Tanojo H, Hostýnek JJ, Mountford HS, Maibach HI. In vitro permeation of nickel salts through human stratum corneum. *Acta Derm Venereol*. 2021;81(212 SE-Articles):19-23. doi:10.1080/000155501753279596
22. Malmberg P, Guttenberg T, Ericson MB, Hagvall L. Imaging mass spectrometry for novel insights into contact allergy—a proof-of-concept study on nickel. *Contact Dermatitis*. 2018;78(2):109-116. doi:10.1111/cod.12911
23. Hagvall L, Pour MD, Feng J, Karma M, Hedberg Y, Malmberg P. Skin permeation of nickel, cobalt and chromium salts in ex vivo human skin, visualized using mass spectrometry imaging. *Toxicol In Vitro*. 2021;76(July):105232. doi:10.1016/j.tiv.2021.105232
24. Hart PJ, Francese S, Claude E, Woodroofe MN, Clench MR. MALDI-MS imaging of lipids in ex vivo human skin. *Anal Bioanal Chem*. 2011;401(1):115-125. doi:10.1007/s00216-011-5090-4
25. Roy S, Touboul D, Brunelle A, et al. Application à la maladie de Fabry. *Ann Pharm Fr*. 2006;64(5):328-334. doi:10.1016/S0003-4509(06)75325-1
26. Harvey A, Cole LM, Day R, et al. MALDI-MSI for the analysis of a 3D tissue-engineered psoriatic skin model. *Proteomics*. 2016;16(11–12):1718-1725. doi:10.1002/pmic.201600036
27. Kompauer M, Heiles S, Spengler B. Atmospheric pressure MALDI mass spectrometry imaging of tissues and cells at 1.4-μm lateral resolution. *Nat Methods*. 2016;14(1):90-96. doi:10.1038/nmeth.4071
28. Kompauer M, Heiles S, Spengler B. Chemical and topographical 3D surface profiling using atmospheric pressure LDI and MALDI MS imaging. *Protoc Exch Published*. 2017;18. doi:10.1038/protex.2017.103
29. Pelikh O, Pinnapireddy SR, Keck CM. Dermal penetration analysis of curcumin in an ex vivo porcine ear model using epifluorescence microscopy and digital image processing. *Skin Pharmacol Physiol*. 2021;34(5):281-299. doi:10.1159/000514498
30. Bouschen W, Schulz O, Eikel D, Spengler B. Matrix vapor deposition/recrystallization and dedicated spray preparation for high-resolution scanning microprobe matrix-assisted laser desorption/ionization imaging mass spectrometry (SMALDI-MS) of tissue and single cells. *Rapid Commun Mass Spectrom*. 2010;24(3):355-364. doi:10.1002/rcm.4401
31. Julander A, Skare L, Vahter M, Lidén C. Nickel deposited on the skin–visualization by DMG test. *Contact Dermatitis*. 2011;64(3):151-157. doi:10.1111/j.1600-0536.2010.01856.x
32. Schneider CA, Rasband WS, Eliceiri KW. NIH image to ImageJ: 25 years of image analysis. *Nat Methods*. 2012;9(7):671-675. doi:10.1038/nmeth.2089
33. Matyash V, Liebisch G, Kurzchalia TV, Shevchenko A, Schwudke D. Lipid extraction by methyl-tert-butyl ether for high-throughput lipidomics. *J Lipid Res*. 2008;49(5):1137-1146. doi:10.1194/jlr.D700041-JLR200
34. Koelmel JP, Kroeger NM, Ulmer CZ, et al. LipidMatch: an automated workflow for rule-based lipid identification using untargeted high-resolution tandem mass spectrometry data. *BMC Bioinformatics*. 2017;18(1):331. doi:10.1186/s12859-017-1744-3
35. Khiao In M, Richardson KC, Loewa A, Hedtrich S, Kaessmeyer S, Plendl J. Histological and functional comparisons of four anatomical regions of porcine skin with human abdominal skin. *Anat Histol Embryol*. 2019;48(3):207-217. doi:10.1111/ahe.12425
36. Tschugaeff L. Ueber ein neues, empfindliches Reagens auf nickel. *Berichte der Dtsch Chem Gesellschaft*. 1905;38(3):2520-2522. doi:10.1002/cber.19050380317
37. Wanner R, Peiser M, Wittig B. Keratinocytes rapidly readjust ceramide–sphingomyelin homeostasis and contain a phosphatidylcholine–sphingomyelin transacylase. *J Invest Dermatol*. 2004;122(3):773-782. doi:10.1111/j.0022-202X.2004.22340.x
38. Vietri Rudan M, Watt FM. Mammalian epidermis: a compendium of lipid functionality. *Front Physiol*. 2022;12:12. doi:10.3389/fphys.2021.804824
39. Nicolaides N. Skin lipids: their biochemical uniqueness. *Science (80-)*. 1974;186(4158):19-26. doi:10.1126/science.186.4158.19
40. Zwara A, Wertheim-Tysarowska K, Mika A. Alterations of ultra long-chain fatty acids in hereditary skin diseases—review article. *Front Med*. 2021;8(August):730855. doi:10.3389/fmed.2021.730855

SUPPORTING INFORMATION

Additional supporting information can be found online in the Supporting Information section at the end of this article.

How to cite this article: Rezaei A, Ganashalingam Y, Schindler S, Spengler B, Keck CM, Schulz S. Metabolipidomic changes induced by dermal nickel penetration determined in an ex vivo porcine ear skin model. *Rapid Commun Mass Spectrom*. 2024;38(20):e9891. doi:10.1002/rcm.9891

2. Supplementary Information

Metabolipidomic changes induced by dermal nickel penetration determined in an ex vivo porcine ear skin model

Rezaei, A.; Ganashalingam, Y.; Schindler, S.; Spengler, B.; Keck, C. M.; Schulz, S. Metabolipidomic Changes Induced by Dermal Nickel Penetration Determined in an Ex Vivo Porcine Ear Skin Model. *Rapid Commun. Mass Spectrom*. **2024**, 38 (20), e9891.

https://analyticalsciencejournals.onlinelibrary.wiley.com/action/downloadSupplement?doi=10.1002%2Frcm.9891&file=rcm9891-sup-0001-SI.docx

Supporting information

Metabolipidomic changes induced by dermal nickel penetration determined in an ex vivo porcine ear skin model

Azar Rezaei [1], Yameera Ganashalingam [2], Siegfried Schindler [1], Bernhard Spengler [1], Cornelia M Keck [2], Sabine Schulz [1] *

[1]Institute of Inorganic and Analytical Chemistry, Justus Liebig University, Giessen

[2]Department of Pharmaceutics and Biopharmaceutics, Philipps University Marburg, Marburg

*corresponding author

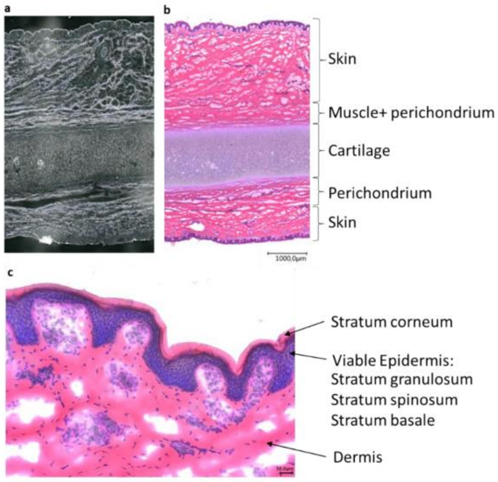

Figure S1. Fresh frozen pig ear cross-section (10 µm thickness) a) Optical images of the sample (magnification 250x), b) H&E staining of the same sample, c) H&E staining of pig ear skin (magnification 500x).

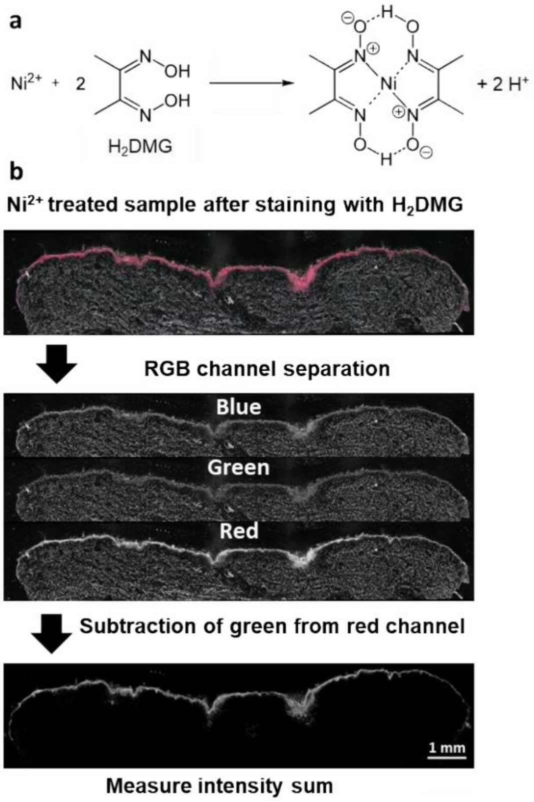

Figure S2. a) Complexation reaction of Ni^{2+} and dimethylglyoxime forming the pink $Ni(HDMG)_2$ complex. b) workflow implemented in ImageJ software for analyzing and measuring the intensity of the $Ni(HDMG)_2$ complex.

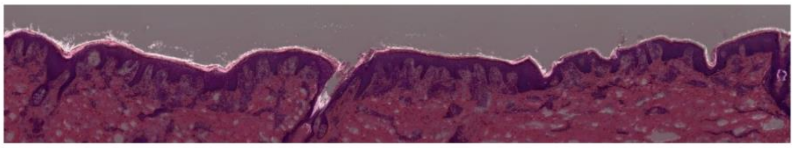

Figure S3. Overlay of H&E staining and $Ni(HDMG)_2$ distribution for 84 µg/cm² nickel-treated pig ear skin cross-section (10 µm thickness, magnification 500x).

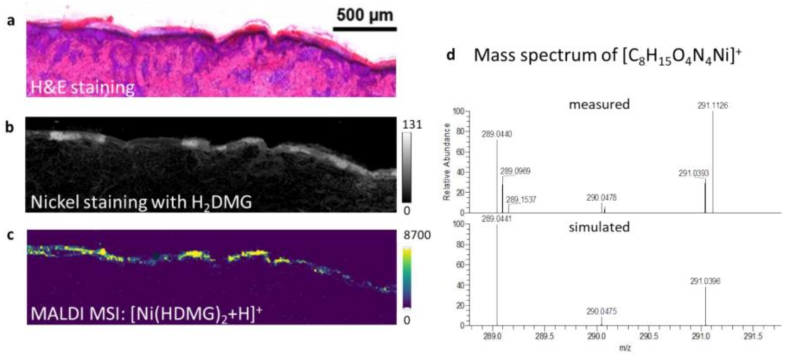

Figure S4. a) H&E staining of 84 µg/cm² nickel-treated pig ear skin, b) distribution of Ni(HDMG)$_2$ in the same sample obtained by light microscopy, c) MALDI MS image of [Ni(HDMG)$_2$+H]$^+$ m/z 289.0440, d) Positive-ion mode AP-MALDI mass spectrum showing the experimental isotopic patterns of [Ni(HDMG)$_2$+H]$^+$ m/z 289.0440 in comparison to the theoretical one.

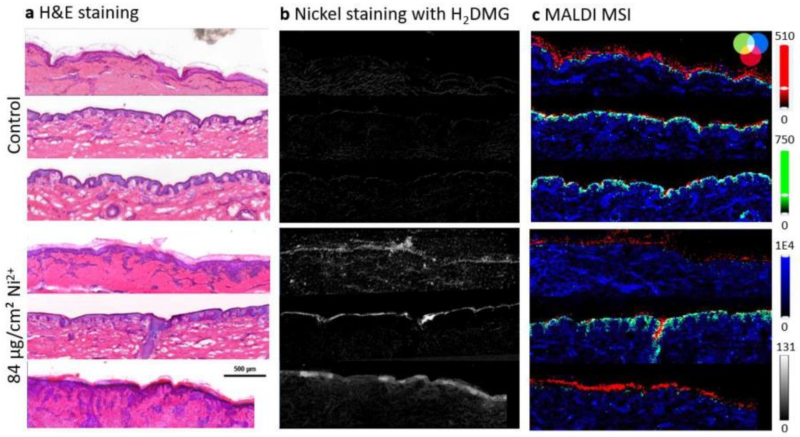

Figure S5. a) H&E staining of three control skin samples and three skin samples treated 84 µg/cm² Ni^{2+}. b) Nickel distribution in the same samples obtained by staining the samples with H$_2$DMG. c) RGB overlay-images of three lipids measured by MALDI MSI of the same samples with a step size of 10 µm in positive ion mode: m/z 522.4880, Cer-NS(d17:1/16:1), [M+H]$^+$ (red), marker for stratum corneum; m/z 760.5851, PC(16:0/18:1), [M+H]$^+$ (blue), marker for dermis; and m/z 716.5225, PE(16:0/18:2), [M+H]$^+$ (green), marker for the viable epidermis. The data was normalized to the total ion count. Skin cross-sections were first analyzed with MALDI MSI, then stained with H$_2$DMG, and afterward stained with H&E.

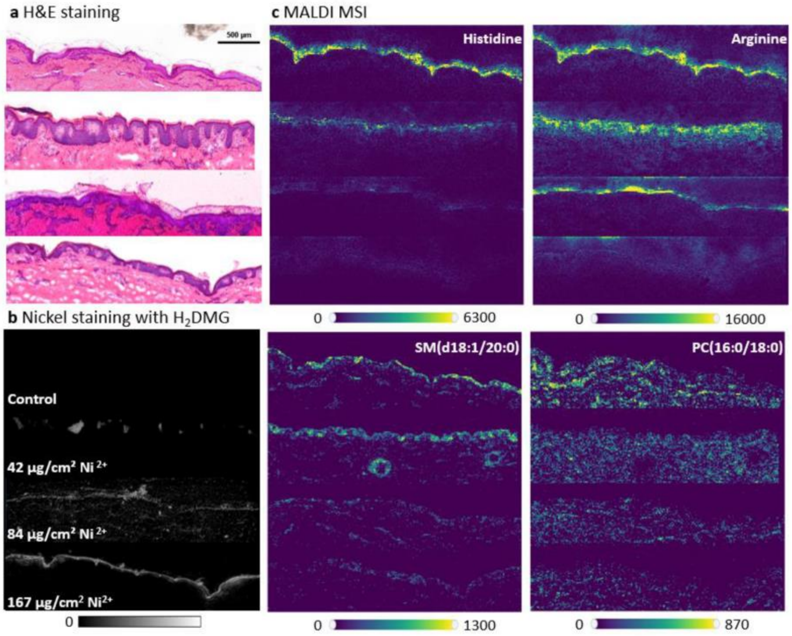

Figure S6. a) H&E staining of control pig ear skin and 42, 84, 167 µg/cm² nickel-treated skin, b) Nickel ion distribution in the same samples obtained by staining with H_2DMG, c) MALDI MSI of the same samples showing the distribution of the following analytes: Histidine (m/z 156.0768, $[M+H]^+$) and Arginine (m/z 175.1190, $[M+H]^+$) found in stratum corneum, SM(d18:1/20:0) (m/z 759.6375, $[M+H]^+$) located in the viable epidermis and PC(16:0/18:0) (m/z 762.6007, $[M+H]^+$) detected in the dermis. Image sizes of 291 × 88 pixels, 298 × 92 pixels, and 302 × 132 for nickel-treated skin samples (42, 84, 167 µg/cm²) respectively and 297 × 103 pixels for control. Pixel resolution 10 µm.

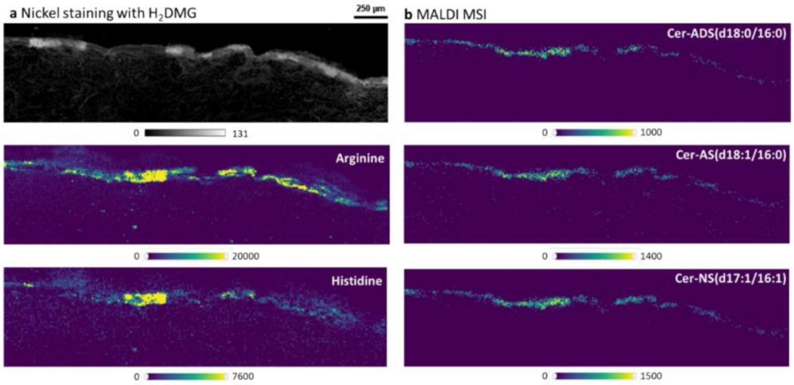

Figure S7. a) Nickel ion distribution in a 84 µg/cm² nickel-treated skin obtained by staining with H_2DMG, b) MALDI MSI of the same sample showing the distribution of the following analytes: Arginine (m/z 175.1190, $[M+H]^+$), Histidine (m/z 156.0768, $[M+H]^+$), Cer-ADS(d18:0/16:0) (m/z 556.5299, $[M+H]^+$), Cer-AS(d18:1/16:0) (m/z 536.5037, $[M+H]^+$) and Cer-NS(d17:1/16:1) (m/z 522.4880, $[M+H]^+$). Pixel resolution 10 µm.

Figure S8. Ni(HDMG)$_2$ distribution (pink color) in an 84 µg/cm² nickel-treated pig ear skin cross-section (10 µm thickness, magnification 500x). Ni(HDMG)$_2$ is mainly found in the top layer of the stratum corneum.

***Table S1**: Reversed-phase chromatographic separation method for lipidomics experiments in positive-ion mode.*

Time (min)	*Flow rate (mL/min)*	*Mobile phase A (%)*	*Mobile phase B (%)*
0	*0.250*	*70*	*30*
2	*0.250*	*57*	*43*
2.1	*0.250*	*45*	*55*
12	*0.250*	*35*	*65*
18	*0.250*	*15*	*85*
20	*0.250*	*0*	*100*
25	*0.250*	*0*	*100*
25.1	*0.250*	*70*	*30*
28	*0.250*	*70*	*30*

Mobile phase A: H_2O: ACN, 40:60 (v/v) with 10 mM ammonium formate and 0.1% formic acid

Mobile phase B: IPA: ACN, 90:10 (v/v) with 10 mM ammonium formate and 0.1% formic acid

***Table S2**: Heated electrospray ionization source parameters for lipidomics experiments in positive-ion mode.*

Tune parameters	*Positive-ion mode*
Sheath gas (a.u.)	*35*
Auxiliary gas (a.u.)	*12*
Sweep gas (a.u.)	*1*
Spray voltage (kV)	*4.35*
Capillary temperature (°C)	*330*
S-lens RF	*55*
Auxiliary heater temperature (°C)	325

a.u.: Arbitrary units, kV: Kilovolt, RF: Radiofrequency

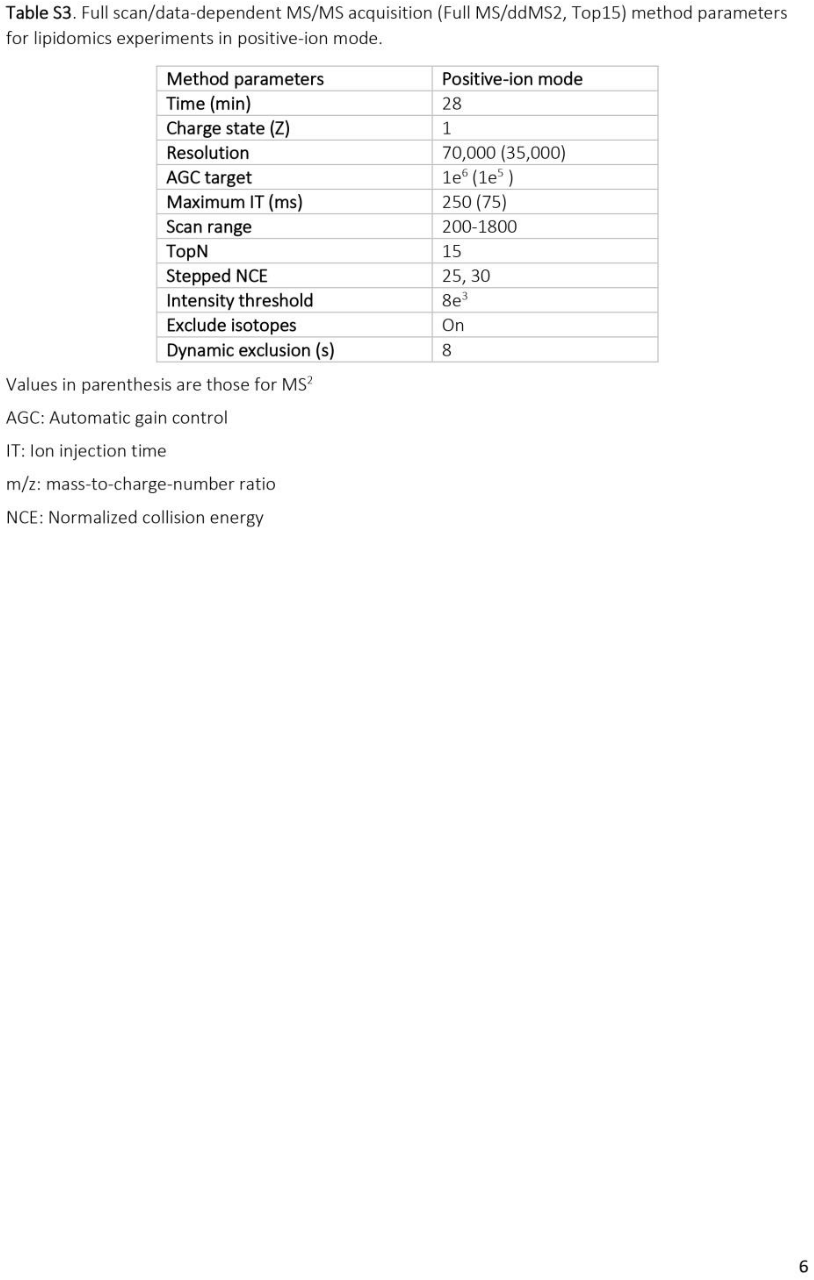

Table S3. Full scan/data-dependent MS/MS acquisition (Full MS/ddMS2, Top15) method parameters for lipidomics experiments in positive-ion mode.

Method parameters	Positive-ion mode
Time (min)	28
Charge state (Z)	1
Resolution	70,000 (35,000)
AGC target	$1e^6$ ($1e^5$)
Maximum IT (ms)	250 (75)
Scan range	200-1800
TopN	15
Stepped NCE	25, 30
Intensity threshold	$8e^3$
Exclude isotopes	On
Dynamic exclusion (s)	8

Values in parenthesis are those for MS^2

AGC: Automatic gain control

IT: Ion injection time

m/z: mass-to-charge-number ratio

NCE: Normalized collision energy

Table S4. Ion images of lipids and amino acids, which were semi-quantified in control and nickel-treated skin cross-sections (3 biological replicates) in Figure 4d-f. The blue color is the minimum intensity, and yellow is the maximum intensity.

m/z	ion	Annotated metabolites	Ion distribution in three control (left) and three 84µg/cm² nickel treated skin cross-sections (right)
734.5694	$[C_{40}H_{80}NO_8P+H]^+$	PC(16:0/16:0)	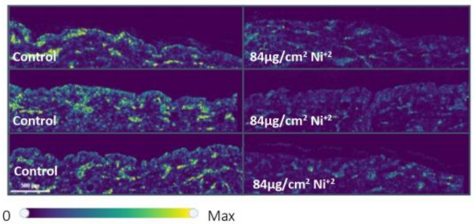
748.5851	$[C_{41}H_{82}NO_8P+H]^+$	PC(16:0/17:0)	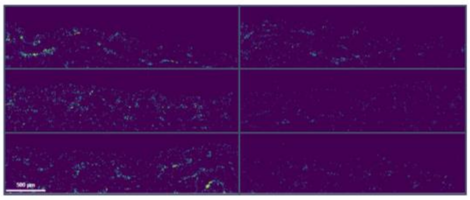
762.6007	$[C_{42}H_{84}NO_8P+H]^+$	PC(16:0/18:0)	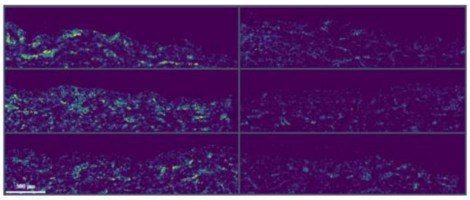
790.5593	$[C_{42}H_{80}NO_{10}P+H]^+$	PS(18:0/18:1)	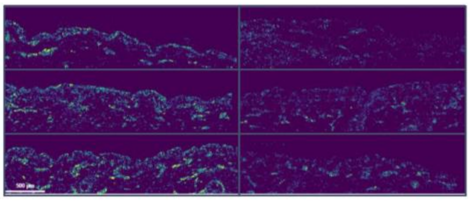

703.5749	$[C_{39}H_{79}N_2O_6P+H]^+$	SM (d18:1/16:0)	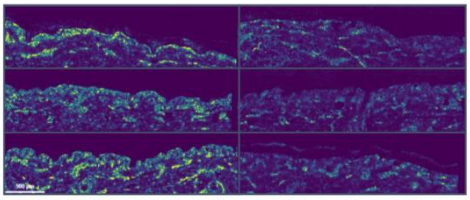
787.6687	$[C_{45}H_{91}N_2O_6P+H]^+$	SM (d18:1/22:0)	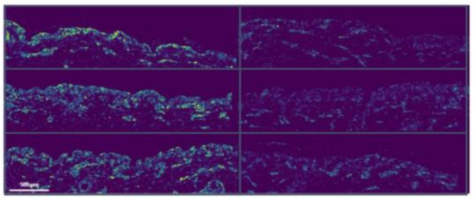
801.6844	$[C_{46}H_{93}N_2O_6P+H]^+$	SM (d18:1 /23:0)	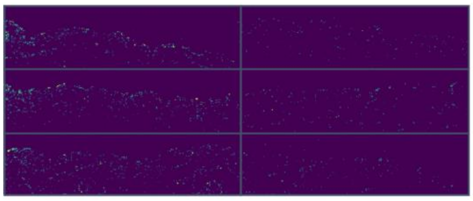
815.7001	$[C_{47}H_{94}N_2O_6P+H]^+$	SM (18:1 /24:0)	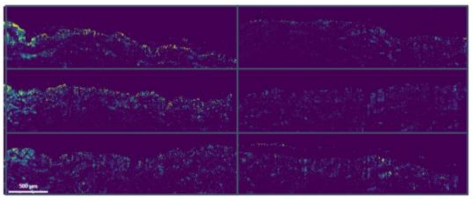
701.5592	$[C_{39}H_{77}N_2O_6P+H]^+$	SM (18:2/16:0)	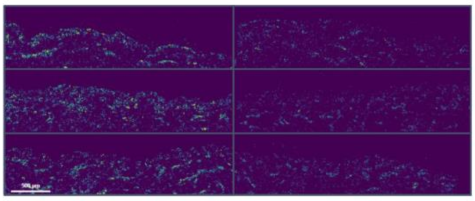

636.4235	$[C_{32}H_{62}NO_9P+H]^+$	oxLPC(24:1(KeOH)	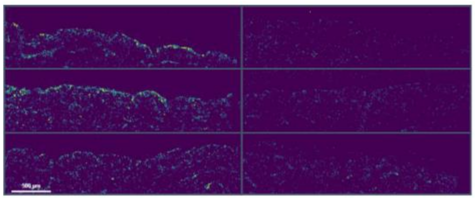
720.5538	$[C_{39}H_{78}NO_8P+H]^+$	PC (15:0/16:0)	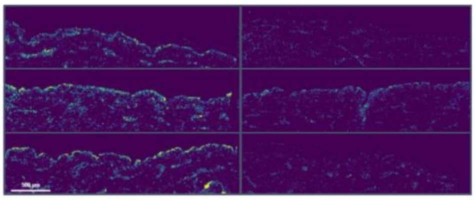
720.5902	$[C_{40}H_{82}NO_7P+H]^+$	PC (O-16:0/16:0)	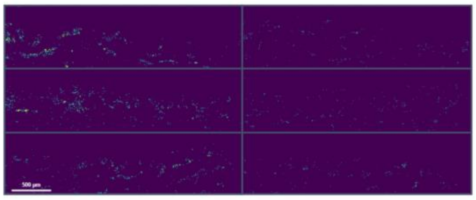
689.5592	$[C_{38}H_{77}N_2O_6P+H]^+$	SM(d17:1/16:0)	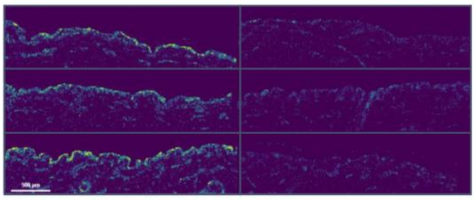
731.6062	$[C_{41}H_{83}N_2O_6P+H]^+$	SM(d17:1/19:0)	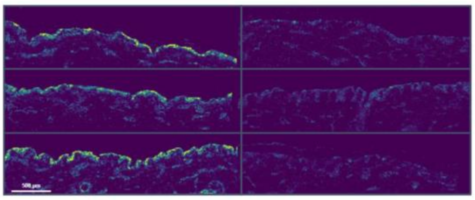

773.6531	$[C_{44}H_{89}N_2O_6P+H]^+$	SM (d17:1/22:0)	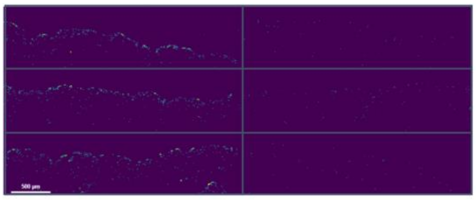
759.6375	$[C_{43}H_{87}N_2O_6P+H]^+$	SM(d18:1/20:0)	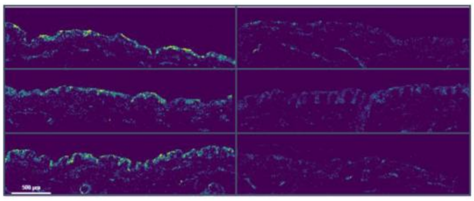
175.1190	$[C_6H_{14}N_4O_2+H]^+$	Arginine	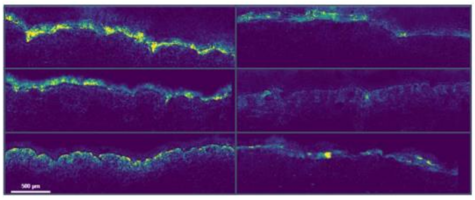
156.0767	$[C_6H_9N_3O_2+H]^+$	Histidine	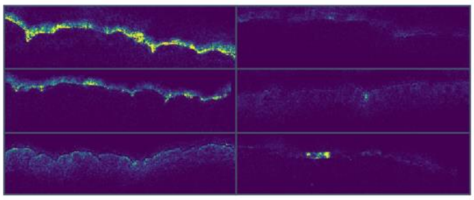
556.5299	$[C_{34}H_{69}NO_4+H]^+$	Cer ADS(d18:0/16:0)	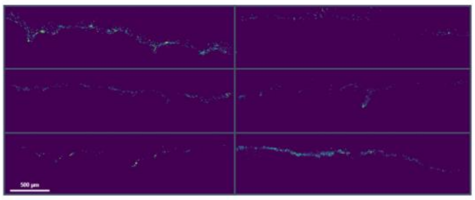

540.4986	$[C_{33}H_{65}NO_4+H]^+$	CerAS(d17:1/16:0)	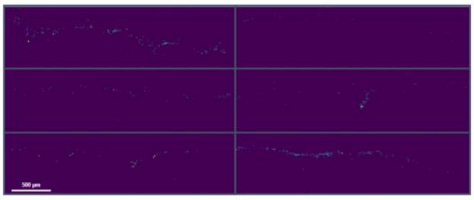
536.5037	$[C_{34}H_{65}NO_3+H]^+$	CerAS(d18:1/16:0)	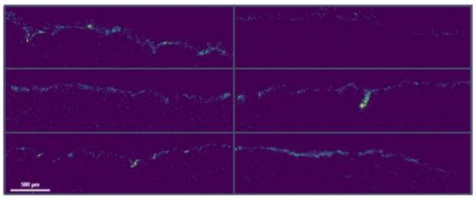
508.4724	$[C_{32}H_{61}NO_3+H]^+$	Cer-NS(d16:1/16:1)	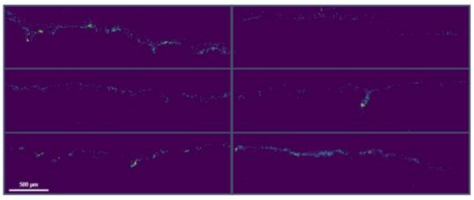
522.4881	$[C_{33}H_{63}NO_3+H]^+$	Cer-NS(d17:1/16:1)	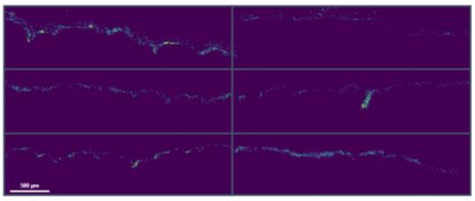

ACKNOWLEDGEMENT

I want to express my sincere gratitude to those who have contributed significantly to the successful completion of this research and my PhD journey.

I am deeply indebted to my supervisors, Professors Dr. Bernhard Spengler and Dr. Siegfried Schindler, for their unwavering support, guidance, and invaluable expertise throughout this endeavor. I would also like to extend my heartfelt thanks to Dr. Schulz for their continuous support and mentorship.

The collaborative environment fostered by the working group was instrumental to my success. Their willingness to share knowledge and offer support created a stimulating atmosphere conducive to research. I am particularly grateful to Prof. Cornelia M Keck and her team for providing essential samples for this study.

Financial support from a PhD scholarship from the DAAD Foundation is gratefully acknowledged. Also, my work in DRUID and the compulsory membership in the GGL are invaluable.

Finally, I express my sincere appreciation to my family and friends, Salar, Dr. Amin, Fezi, Aschkan, and Dr. Mahshid, for their unwavering belief in me and constant encouragement.